`

MODELLING OF COMBUSTION IN NATURAL DRAFT BURNERS FOR IMPROVED PERFORMANCE

BY

NWOYE FAVOUR CHUKWUNONSO

(B.Eng., M.Eng.)

Reg No; 20164992728

To

Department of Mechanical Engineering

School of Engineering and Engineering Technology

Federal University of Technology, Owerri

CERTIFICATION

This is to certify that this work: **"Modelling Of Combustion In Natural Draft Burners For Improved Performance"** was work carried out by **Nwoye Favour Chukwunonso** (Reg. No: 20164992728) in partial fulfilment of the award of Doctor of Philosophy (PhD) Degree in Mechanical Engineering (Energy and Power Engineering Option), Federal University of Technology, Owerri.

Engr. Prof. C.A. Okoronkwo
Principal Supervisor

26/02/2024
Date

Engr. Prof. E.E. Anyanwu
Principal Supervisor

26/02/2024
Date

Engr. Dr. G.N. Nwaji
Co-Supervisor 1

26/02/24.
Date

Engr. Dr. O.C. Nwufo
Co-Supervisor 2

26/02/2024
Date

Engr. Dr. G.O. Onuoha
Head of Department

26/02/2024
Date

Engr. Prof. Remy Uche
Dean, SEET

26/2/24
Date

Profesor B.O. Esonu
Dean, PGS

Date

Eng. Prof. F. Abam
External Examiner

06/02/2024
Date

`

DEDICATION

Dedicated to God. To my wife and children; Ebube, Ebere and Amara

`

Acknowledgment

To my principal supervisor, Engr Prof. Chukwunenye Okoronkwo, I want to say thank you for your calm and persistent leadership. You gave suggestions and advice in the course of this work and wrote the qualifying memos at every stage of the examination. Your report to my employers assured them that the work was on course.

Engr. Prof Emmanuel Anyanwu, your capacity to actively supervise works at your level and age is uncommon. Also intriguing is your deliberateness in training people who can stand in your stead. Your influence and interpersonal relationships gave me an edge. You are indeed a father, and I am grateful.

Engr. Dr. Godswill Nwaji took the time to read the manuscript. He made contributions and pointed out errors, the ambiance around him was friendly, and he spoke hope to me in my low moments.

To Engr. Dr. Olisaemeka Nwufor, I want to say thank you. You handled me on combustion, which was foundational to my research. You interfaced with PG school for exam dates and followed up on memos. Interacting with you was always a pleasure.

My short interaction with Engr. Dr. Nze Ebuka was helpful. I gained from his wealth of experience in CFD in ways he may never know.

This work progressed well under Engr. Dr. G.O Onuoha is the head of the Mechanical Engineering Department. His gentle nudge was a needed catalyst.

To every staff member of the Mechanical Engineering Department and colleagues who may have contributed to making this work a success, may the good Lord reward you.

To my beloved brother Humphrey Okoro, you were God's provision for me on this academic journey. With you, I didn't bother about accomodation and feeding. You made your car available for some of our travel. God bless you for always looking out for me.

This work received funding from TETFUND, and I am grateful.

I want to thank my Family. My wife Mrs Adaobi Nwoye, my children Ebube, Ebere, and Amara, my parents, and siblings, you were my pillar, a source of strength and comfort. You moved me on.

Above all, I want to thank God for his mercies throughout this academic journey. There were tales of woes and kidnapping on our route as we traveled to Owerri, but the Lord preserved us even when we journeyed into the night and made provision for us in unimaginable ways.

`

Table of Contents

`

`

`

Table of Figures

`

`

ABSTRACT

Combustion in natural draft burners involves the passive induction of atmospheric air into the burner mixer when a fuel jet flows through a venturi. The interaction of the fuel jet and air stream at different velocities causes shear and Kelvin Helmholtz instability that grows into turbulence and molecular mixing of both species. Modeling of flow and combustion process in natural draft burners for improved performance are presented. It involves the response of the flow to changes in the axial coordinate of the nozzle and passive alteration of the flow conditions upstream of the origin. The alteration was by varying the nozzle streamlines and installing a trip ring at the nozzle exit. The Reynolds Averaged Navier-Stokes (RANS) equation was used to model the flow physics; the turbulence modelling was done with the Reynolds Stress Model (RSM), while the standard wall function captured the near wall flow behaviour. The implementation was undertaken using ANSYS Fluent 18.1, and the model was validated with Binder and Kian experimental work. A low-fidelity model developed and implemented with a MATLAB script offered a cheap and quick alternative for the parametric investigation of jet flow and combustion processes. The flow parameters of interest are the velocity decay, pressure gradient, turbulence, ambient air entrainment, and its mixing with the fuel jet stream. The ratio of the axial distance between the nozzle exit and throat l_{TN} and the throat diameter d_T, $\frac{l_{TN}}{d_T}$ defined the position of the nozzle from the throat. At $\frac{l_{TN}}{d_{T=2.0}}$ and $\frac{l_{TN}}{d_T} = 0.5$ as reference, the increase in the velocity decay rate and the entrainment values were over 8% and 7%, respectively. These shows that when the nozzle was closer to the air inlet, velocity decay was faster, the entrainment was higher, and the mixing was better. The modification with the trip ring involved the installation of 0.5mm thick rings at the nozzle exit. The installed ring diameters were 4.9, 4.7, and 4.5mm, concentric with the nozzle trailing edge. The wake formed behind the trip ring interacted with the streamwise vortices and suppressed the near-stream turbulence. Flow modification with a 4.9mm ring increased the turbulence at the ejector outlet by over 26.6%. The final entrainment value was 16.7% higher, but the drop in the decay rate was 9.6%. The 4.9mm ring performed best because of the delayed flow separation and reduced pressure drag. Four different nozzle streamlines (PN1, PN2, PN3, and PN4) produced by straight lines and sine function combinations yielded different streamwise sectional area. With PN4 as the reference nozzle, the decay rate, entrainment and the maximum turbulence intensity increased by approximately $1.7, 8\ and\ 16\%$, respectively, in the PN3 nozzle, which has the smallest streamwise sectional area and the highest momentum difference between the streams. The relationship between the near stream decay rate and the streamwise sectional area was linear. Therefore, passive modification of the jet structure improved the burner performance substantially. Pressure drag formed behind the ring adversely affected performance. An optimized streamlined ring profile can delay flow separation and reduce pressure drag, thus recommended for further investigation.

Keywords: Natural draft burners; Combustion; modeling; Shear layer; Trip ring; Velocity decay; Pressure gradient; Entrainment, Turbulence

`

CHAPTER 1

1 INTRODUCTION

1.1 Background of study

Efficiency and the impact of combustion products on the environment have remained topical despite the record improvement in combustion systems in the recent past. Chemical energy in fuels is released as heat during combustion, with water and carbon dioxide as by-products when the combustion reaction is complete. The release of carbon dioxide into the atmosphere increases the concentration of greenhouse gases that cause global warming.

When the combustion is incomplete, carbon monoxide and even carbon particles are released, in addition to the carbon dioxide, thus complicating the problem further.

To abate these pollutants, designers of combustion units have adopted some pre\post combustion measures such as the burner unit redesign or flow process control to enhance the air/ fuel proportion and their mixing. Others are selective and non-selective catalytic reduction treatment of flue gases to reduce the number of toxic substances released into the atmosphere or their toxicity (Philip, 1997).

Furnaces, ovens, incinerators, domestic water heaters, and cooking ranges are some of the popular combustion equipment, of which the burner is a principal component. In burners, fuel, and oxidizer mix in a controlled manner to produce a flame. The extent of mixing and their proportion are functions of burner design, and they influence flame properties like stability, heat intensity, and emission constituents (Charles, 2003). Many burner designs exist depending on the choice of fuel/oxidizer, environmental regulation, heat transfer requirement, operating condition, and application. A good number of burners in use today make use of gaseous fuel. For complete combustion in a gas burner, the oxidizer, usually air, must be available in the right proportion and mixed with fuel at a molecular level. The processes leading to combustion in burners are fuel injection, the induction of primary air, and the mixing of the two. The manipulation or control of any of these processes can significantly affect performance.

Fuel admission into burners is in the form of jets. In jet flow, a high-velocity stream thrusts into still air or other surrounding fluid with consequent momentum transfer. The velocity differences between the two streams in contact cause shear that leads to Kelvin Helmholtz instability. The instability grows into turbulence a short distance from the origin and appears as a series of vortex rings (Liepmann & Gharib, 1992). The interfacial area where this occurs is known as the shear layer.

The nature of the turbulence will depend on the initial conditions and will determine the degree of mixing (Mohsen, 2011). A change in the initial conditions, say by exciting the jet and altering the geometry of the trailing edge of the nozzle or even by manipulating the structure of the boundary layer at the exit using trip rings or splitter plates, will vary the turbulence structure and mixing performance of the burner.

In free jets, air is readily available for entrainment purposes. In burners, however, the flow is confined and requires an external air supply. Supply of air into burners is either by a mechanical device such as a fan/blower or by a pressure gradient developed passively between the atmosphere and the burner inlet. The former is the forced draft burner, and the latter is the natural draft burner. In natural draft burners, the air supply is by pressure gradient developed between the venturi and the inlet because of the pressure drop associated with velocity increase in the venturi. Compared to free jets, entrainment in confined jets is lower due to momentum losses to the wall. Therefore, the design goal for most natural draft burners is to improve the entrainment performance (Demetris, Robert, & Wes, 2003).

The shape of the confining tube is in the form of an ejector (El-Zahaby, Hamed, Omara, & Eldesoukey, 2017). An ejector is a tube with a curved constriction at entry known as the throat and varying cross-sectional area downstream to ensure seamless and maximum entrainment of the surrounding fluid

(Figure 1.1). The throat cross-sectional area, the fuel nozzle coordinate, and the downstream profile of the tube (diffuser) can influence the entrainment performance (Peter, Robert, & Darren, 2016).

Other uses for ejectors include mixing exhaust gases with fresh air to reduce the temperature or suppress infrared signatures in aircraft (Asim, 2008) and to improve the performance and the structural integrity of equipment like gas turbines susceptible to failure at high temperatures (Keribo & Barinaadaa, 2018). Mixing flue gasses with fresh air before combustion using an ejector can reduce flame temperature and NOx formation (Philip, 1997). The chemical and biochemical industries engage ejectors to entrain or pump corrosive fluids, fumes, and dust-laden gases (El-Zahaby, Hamed, Omara, & Eldesoukey, 2017). They are also suitable for thrust augmentation in aircraft, noise reduction in the exhaust, and cycle optimization in refrigerating units.

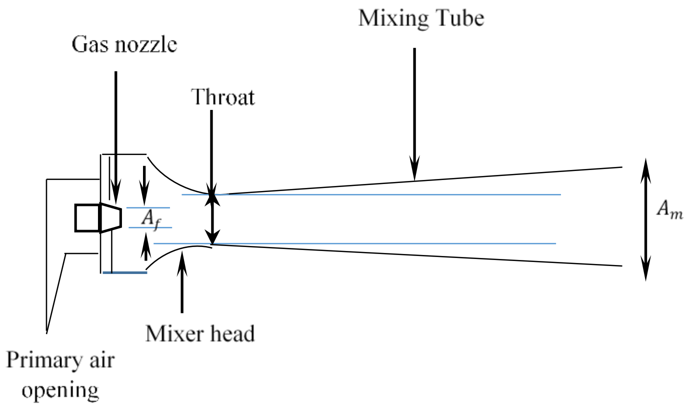

Figure 1.1 The schematic of a coaxial ejector

`

When the entrained air constitutes a fraction of the total air requirement for complete combustion, the flame produced is said to be partially premixed. However, when the air is sufficient, it is fully premixed. Complete combustion in partially premixed systems is achieved by secondary air diffusion to the hot combustion gases downstream of the flame front. Natural draft burners are good examples of partially premixed devices. The flame they produce is within a laminar regime (Lorenzo, 2008).

For stable operation, the flame must not extinguish, lift, or flashback to the tube over a wide range of service conditions, and the combustion must be complete within the stable range. The burner must also allow ready ignition, cross lighting, uniform distribution of heat over the heated area, and quiet operation (Kenya Bureau of Standards, 2013), (Lorenzo, 2008), (Bureau of Indian Standards, 2002) and (Department of Commerce Bureau of Standards, 1931).

Meeting these requirements for a range of service conditions can be challenging and may require trade-offs because conditions that support one may be detrimental to the other. For example, increasing the primary air volume, which aids complete combustion and improve efficiency due to reduced secondary air requirement that convects heat away from the system, can increase the tendency of flame to lift or flashback. In contrast, secondary air guarantees complete combustion in adverse service conditions. Hence, secondary air must be small enough to minimize convective heat losses from the system yet sufficient to ensure complete combustion under adverse service conditions. Conversely, the volume of primary air entrained must permit stable operation yet large enough to reduce the secondary air requirement to a permissible minimum. Passive manipulation of the jet flow and confining tube optimization is relatively easy and can lead to better entrainment, mixing, noiseless operation, and adaptation of the burner to other fuels.

1.2 Problem Statement

The energy costs have increased astronomically in the last few years, hence the need for more efficient conversion of chemical energy in fuels to heat energy. In addition, the operation flexibility of a good number of combustion devices is limited. For example, the conventional SI engines that use PMS will perform poorly or damage if the fuel or its composition changes. Even the combustion in domestic gas stoves will be incomplete and produce soothe or be unstable with changes in fuel composition. Natural draft burners have a cost and simplicity advantage over forced draft burners, but their flexibility is limited. The primary air volume and turbulence in forced draft burners are easier to regulate, hence the choice of the burner for industrial application. To scale up the capacity of a natural burner, the performance per air entrainment and mixing must improve to guarantee the right proportion and mix of fuel and air per time, ensure optimum energy release, and minimize pollutant discharge to the atmosphere from a given fuel mass.

1.3 Objectives

The main objective of this research work is to model combustion in natural draft burners for improved performance. The specific objectives include

I. To develop mathematical models that compute the entrained mass of air and velocity in the confining/mixing tube.

II. To employ RANS model for CFD simulation of the flow process using ANSYS FLUENT.

III. To validate and carry out a parametric study on the system using the developed models and how each variable will affect air entrainment, mixing of entrained air and fuel, velocity and pressure variation in the system.

`

IV. To find the optimum geometry for the mixing tube and explore the effectiveness of some passive control options in enhancing air entrainment and mixing.

1.4 Justification of the study

The energy industry is fast evolving, and government policies regarding the permissible emission level are becoming more stringent as the world is confronted daily with the dangers of greenhouse gas emissions to the environment and human health. More so, most energy resources are limited, the need for them is growing, and their cost is rising. Hence, the necessity to keep pace with the evolving industry by adapting combustion units to new and alternative energy resources and to design more efficient systems that meet government regulations.

The application of natural draft burners is versed, cutting across industries. They are for lighting and heating purposes. They find use in gas turbines, steam engines, industrial furnaces, boilers, and domestic gas stoves. The proposed modification is simple and cost-effective and can improve the air entrainment and the mixing efficiency, reduce complexity, and eliminate the need for and the attendant cost of extra units such as blowers to supply air.

The modification of Jet structure to alter the mixing and entrainment properties can be passive hence, more adaptable to changes in physical parameters of the air and use with other fuel sources. A well-designed ejector will ensure noiseless operation, guaranteeing that air flows through the throat without separation or recirculation.

`

1.5 Scope of Study

The focus of the research shall be limited to optimizing the primary air entrainment and mixing performance in natural draft burners. The methodology will be 3D modeling of the flow process with ANSYS FLUENT. The experiments will be limited to input parameter estimation.

The focus of the study will include variations in the initial conditions, the geometry of the confining tube and exit port area, and how they affect entrainment, mixing, velocity distribution, and pressure variation in the system.

`

CHAPTER 2

2 LITERATURE REVIEW

2.1 Background Information on Existing Systems

Burners have domestic and industrial applications and come in different forms and sizes. They are forced draft or natural draft, depending on whether the air induction into the system is by blowers or passive pressure gradient, respectively (Charles, 2003). Alternative forms of burner classification are non-premixed, premixed, and partially premixed (Lorenzo, 2008). In non-premixed burners, fuel and oxidizer blend is by diffusion at the flame front. Non-premixed burners produce diffused flames that are long and of low intensity. In premixed burners, the fuel and oxidizers mix upstream of the flame front in a proportion that guarantees complete combustion. In partially premixed burners, the mixing of fuel and air is upstream of the flame front, and their proportion is below the stoichiometric ratio and requires a secondary air supply to complete the combustion. Other modes of classification include air induction method, fuel type, emission, and flame shape (Erwin, Charles, & John, 2013). Burners come in different forms based on the application and operating condition and with additional units such as temperature controllers, temperature sensors, and damper blades. Whichever is the case, the principle of operation is the same- air is forced into the mixing tube using a blower or drawn naturally by the pressure gradient. The induced air is mixed with the fuel ahead of ignition and burns to produce heat in a controlled manner.

Natural draft burners consist of a venturi unit and a burner tip (Figure 2.1) and operate in partially premixed mode. The pressure gradient between the burner and the atmosphere responsible for primary air induction is relatively low and does not permit air up to the stoichiometric limit. Complete combustion requires additional or secondary air that blends with the premixed charge downstream of the flame front by diffusion.

`

The primary air supply in natural draft burners happens through the entrainment and the induction of atmospheric air to replace the entrained air. Minimizing momentum losses to the confining wall during air induction is a critical performance concern, resolved by proper tube geometry design (Demetris, Robert, & Wes, 2003).

Mixing air and fuel is, by turbulence, a function of the initial or flow condition at the nozzle exit (Sadeghi & Pollard, 2012).

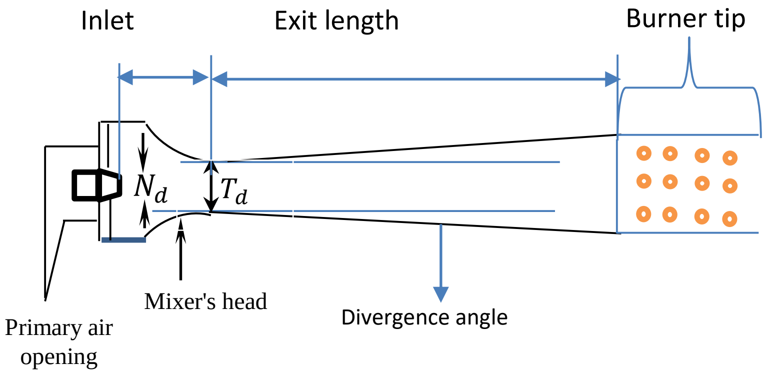

Figure 2.1 The natural draft burner

2.2 Ejectors/Venturi Jet Mixers

Ejectors are cheap and easy to maintain, and their operation depends on the venturi effect. In venturi, the pressure energy of motive fluids transforms into kinetic energy. The resultant pressure gradient

`

causes suction and entrainment of the surrounding fluid. This effect has found application in ejectors used in heat pumps for compressor work recovery and in refrigerators for cycle performance improvement. In subsea applications, they help lower pressure in the well, reduce condensate loading, boost production, and maximize recovery (David, 2013).

Mathematical models, experiments, and computer simulations are the tools for ejector performance analysis. The CFD studies include the optimization of the mixing chamber for two throat nozzle ejector (Fatong, Dazhang, & Jing, 2021), the influence of operating conditions on optimum nozzle exit position (Ali & Mohammed, 2020), parametric analysis of inlet pressure and primary nozzle position on performance (William, José, Iván, Johan, & John, 2020) and optimization of nozzle structure for maximum gas induction (Enle, Xiaofeng, & Long, 2020). Others are parametric investigation by Scott, Aidoun, Bellache, & Ouzzane (2008) to identify key features that impact ejector performance and the study of the performance of steam ejectors for use in a refrigeration/heat pump system by Mustafa & Cuneyt (2019). 1D models were developed by Lawn (2002), Hafiz et al. (2020), and Matrio et al. (2021) to investigate the performance of ejectors. Hadi (2017), Schmidt & Hupfer (2021), and Nakagawa, Berana, & Harada (2008) used experiments and CFD simulation (2017). The works by Subramanian et al. (2018) and Voropayev, Sanchez, Nath, Webb, and Fernando (2011) were strictly experimental.

Systems that use ejectors prioritize the secondary fluid entrainment and its mixing with the primary stream. Other performance indicators include pressure profile, mass flux, volume fraction, entrainment ratio, pumping coefficient, the mean velocity at the outlet, axial velocity distribution, and turbulent kinetic energy (Zihzhen, Tianyang, Fangxiang, Lin, & Rui, 2020), (Ali & Mohammed, 2020), (Krzysztof & Robert, 2017) & (Manisha & Bhim, 2017). The factors that influence performance include the pressure difference between the inlet and outlet section (Yanqi & Wenquan, 2012) & (Zhang, 2017), the design of the nozzle (Enle, Xiaofeng, & Long, 2020) & (Fatong, Dazhang, & Jing, 2021), the working fluid (Ali & Mohammed,

`

2020) and structural parameters of the mixer such as area of throat to nozzle ratio, suction chamber area ratio and nozzle exit position or projection ratio (Agrawal, 2013). Other parameters include the throat contraction ratio, contraction angle, expansion angle, and throat aspect ratio (Yanqi & Wenquan, 2012) & (Zhang, 2017).

Mass flux correlated positively with the contraction ratio and inlet/outlet pressure differential, but the reverse was the case with diffusion angle (Zhang, 2017). The investigation by Vashahi, Ra, Choi, and Lee (2017) showed that contraction ratio affects entrainment the most compared to air inlet diameter and diffuser angle. This position agrees with the investigation by Yanqi and Wenquan (2012) on the effect of structural parameters on hydraulic performance. The performance criteria included the minimum pressure achieved in the unit and the mean velocity at the outlet. Juan, Carmen, Benito, Guilherme, and Denise (2016) also investigated the influence of throat morphology on velocity distribution in ejectors.

Energy transition to future group (ETF) designed a multi-fuel, low-emission burner numerically (Saponaro, et al., 2020). A parametric investigation to help identify features that impact ejector performance by Scott, Aidoun, Bellache, & Ouzzane (2008) was by CFD. The performance criteria of a steam ejector investigation by Mustafa and Cuneyt (2019) using ANSYS FLUENT were static pressure distribution, temperature variation along the centerline, and velocity profile. Using experiments and CFD simulation, Hadi (2017) investigated the performance of a radial flow ejector for use in refrigerators with entrainment ratio and critical exit pressure as the performance criteria. Still for application in refrigerators and using CFD, Kemal, Sen, and Iskender (2013) investigated the performance of a gas ejector. The performance criteria again were entrainment ratio, while the nozzle position relative to the ejector inlet and temperature were the varied parameters.

Matrio et al. (2021) developed a 1D model based on energy and momentum conservation and an isentropic equation to investigate the performance of gas burner ejectors. The 1D result obtained agreed

`

well with the 2D CFD simulation and experiment. A similar model was developed by Lawn (2002) with a 1D flow momentum conservation equation, and the result also agreed well with the experimental result. Hafiz et al. (2020) derived a 1D model using multivariate polynomial regression to predict the flow field inside an ejector with entrainment and compression pressure ratio as major performance-influencing parameters.

Primary aeration in natural draft burners with venturi configuration was between 40-80%, depending on the working fluid and other conditions (Brandon, 2019). The axial coordinate of the nozzle, the mixer head finishing, the diffuser length, the diffuser angle, and the area of the primary air opening affect performance. The optimal value for the inlet length recommended in the literature ranges between 2-2.5 throat diameters, while the range for the diffuser length was between 6-8.5 throat diameter (Brandon, 2019) and (Peter, Robert, & Darren, 2016). The industry standard for the diffuser divergence angle is 2-3.5 degrees (Demetris, Robert, & Wes, 2003). At higher values, entrainment performance reduces due to the formation of recirculation zones.

2.3 The Dynamics of Flow in Gas Burners

Flow in natural draft burners involves the induction of atmospheric air and the formation of the reactive mixture.

When two fluids flowing at different velocities in the same direction come in contact, there is a momentum transfer from the high-velocity fluid to the low-velocity fluid. The result is shear force formation at the contact surface, which causes instability that eventually grows into turbulence. This is the nature of flow in natural draft burners when high-velocity gas from the nozzle comes in contact with quiescent air at the mixer head. The shear at the nozzle exit causes the formation of trains of coherent vortex rings or eddies. The vortices grow in scale downstream of the origin by paring and form a part of the turbulent interfacial area known as the mixing or shear layer (Figure 2.2) and (Figure 2.3).

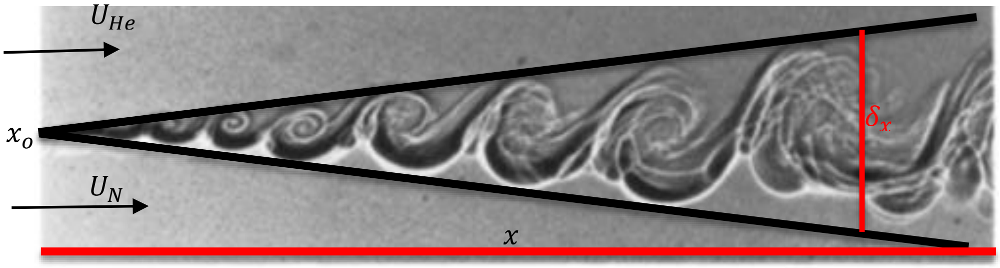

Figure 2.2 Plane mixing layer between Helium (upper) and Nitrogen (lower) at $Re \approx 5000$ *(Brown & Roshko, 1974)*

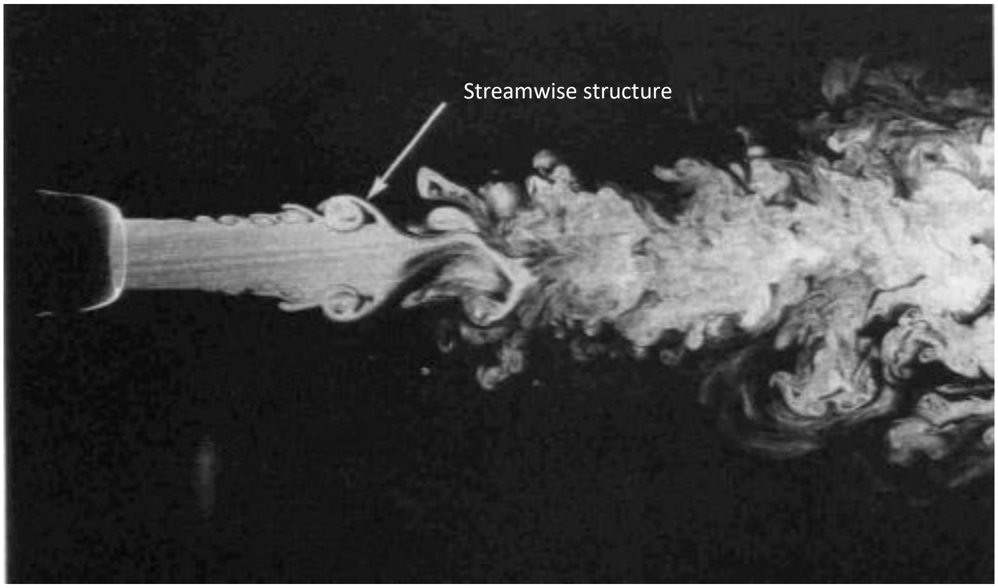

Figure 2.3 LIF side view of Jet at $Re \approx 5500$ *(Liepmann & Gharib, 1992)*

A breakdown of the vortices into small-scale eddies happens a short distance from the origin, leading to turbulence and molecular mixing of the fluids in jet flow (Figure 2.3). The induction of the low-velocity fluid into the turbulent interfacial area is called entrainment.

`

2.4 Mixing/shear layer

From the seminal experiments of Brown & Roshko (1974), Bernal & Roshko (1986), and Liepmann & Gharib (1992), the following are the characteristics of shear layers;

- Shear layers form when fluids at different velocities come in contact, as in plane mixing layers and jet flows.
- Shear/mixing layers are turbulent and characterized by large two-dimensional structures referred to as the primary structure and a secondary or streamwise structure, which is three-dimensional.
- The two structures vary in space and time and grow with increasing distance from the origin.
- The growth of the primary structure is linear on average, and the spread is affected by conditions upstream of the origin, the Reynolds number of the flow, density, and the velocity ratios of the streams.
- The streamwise vortices are responsible for entrainment and
- a distinctive feature of the plane mixing layer is the persistence of streamwise vortices. In the jet flow, the centreline velocity decay starts at $X/d \approx 5$. The velocity difference between the streams decreases in the streamwise direction due to momentum transfer. This decrease weakens the shear that sustains the structure. In the plane mixing layer, the decay witnessed in jet flow does not occur due to imposed shear by keeping the velocity difference constant.

`

2.5 Plane Mixing Layer

The plane mixing layer described in by Brown and Roshko (1974) also approximates the near-field mixing region of an axisymmetric jet. The motivation of the experiment was the need to sustain the distinct properties of individual flow and to allow for flexibility in the choice of parameters (density and velocity)

Tangents drawn to the edges of the vortex (Figure 2.2) form a wedge with a vertex at a virtual origin x_o. The ratio of the thickness of the shear layer δ_x to the axial distance x measured from the virtual origin measures the spread angle or the rate at which the shear layer grows and sets the boundary for the maximum amount of reactive mixture formation. The fluid species involved in the mixing layer do not all form a combustible mixture. The proportion of the species in the layer involved in the combustion reaction is those mixed or combined at the molecular level. Correct mixture formation is primarily a function of shear layer growth and molecular mixing of species in the shear layer.

A critical parameter in shear layer development is the Reynolds number (Re) given by

$$Re = \frac{\delta_x \Delta u}{\nu} \tag{2.1}$$

δ_x the thickness of the shear layer increases in the axial direction. The value is local and depends on the axial distance from the virtual origin.

$The\ parameter\ \Delta u$ is the difference between the free stream velocities $(U_N - U_{He})$, while ν is the appropriate measure of kinematic viscosity.

`

2.6 Shear Layer Growth

Shear layer growth depends on velocity and density ratios $u_r\ and\ \rho_r$, respectively. Other parameters that affect shear layer growth are the Mach numbers $M_{c1}\ and\ M_{c2}$ of the two streams and streamwise pressure gradient $\frac{dp}{dx}$ (Dimotakis, 1991).

Brown and Roshko (1974) were the first to document the study of the dependence of shear layer growth rate on density and velocity ratio. Subsequently, Brown (1974) suggested a model for the combined effect of velocity and density ratio on entrainment rate (Eqn. (2.2)).

$$\frac{\delta}{x} = C_\delta \frac{(1-u_r)(1+{\rho_r}^{0.5})}{(1+{\rho_r}^{0.5}u_r)} \tag{2.2}$$

Further investigations by Dimotakis (1991) revealed that entrainment of the free streams is asymmetric and modified the brown model to account for it (Eqn. (2.3)).

$$\frac{\delta}{x} = C_\delta \frac{(1-u_r)(1+{\rho_r}^{0.5})}{2(1+{\rho_r}^{0.5}u_r)} \left\{1 - \frac{(1-{\rho_r}^{0.5})/(1+{\rho_r}^{0.5})}{1+2.9\,(1+u_r)/(1-u_r)}\right\} \tag{2.3}$$

The factors outside the braces are the same as Brown's model in Eqn. (2.2) and describes the temporal growth of the layer. The expression in the braces is for spatial growth. The study of the dependence of the shear layer growth rate on ρ_r using both models showed that $\frac{\delta}{x}$ increased with density ratio. The differences in values of $\frac{\delta}{x}$ predicted by both models are relatively small, and at $\rho_r = 1$, the terms in the bracket equated to unity.

`

Dimotakis (1991) compared the dependence of $\frac{\delta}{\mathrm{x}}$ on ρ_r at velocity ratios $0.2 \text{ and } 0.4$, respectively. An increase in u_r suppressed the shear layer growth significantly. In Comparison to u_r, the change in $\frac{\delta}{\mathrm{x}}$ with respect to ρ_r was negligible. Hence, the shear layer growth depends more on u_r.

2.7 Jet Flow

Jet flow is slightly different from plane mixing layers. In the plane mixing layer, the shear layer sustains because of the persistence of the velocities of both streams. In jets, the high-velocity streams discharge into a surrounding fluid. The resulting instability and subsequent vortex roll-up lead to a series of vortex rings that grow outward into the surrounding air and inward toward the jet center. Due to progressive merging and pairing at every $x/d \approx 2$ (Liepmann & Gharib, 1992), the vortex ring grows inward enough that the diameter spans the radius of the jet. What follows is the breakdown of the potential core and the vortex ring into smaller structures (Figure 2.3and Figure 2.4). This breakdown into small eddies marks the beginning of the mixing transition.

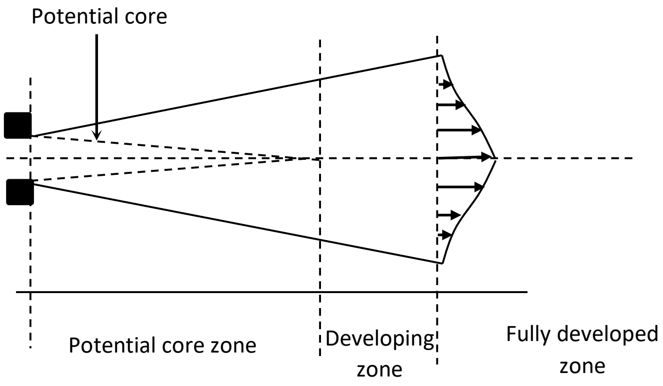

Figure 2.4 Jet Flow Development

2.8 The Mixing Process

Turbulent shear layers are characterized by 2D vortical structures and 3D counter rotating streamwise vortices (Figure 2.5). By the reason of conservation law associated with 2D structures, energy cannot be transferred to smaller scales i.e. they can only be rearranged in space but not reduced or increased (Ecke, 2017). Under this condition, entrained fluid participate in large scale motion but remain relatively unmixed because the area of fluids in contact relative to volume is small (Figure 2.6).

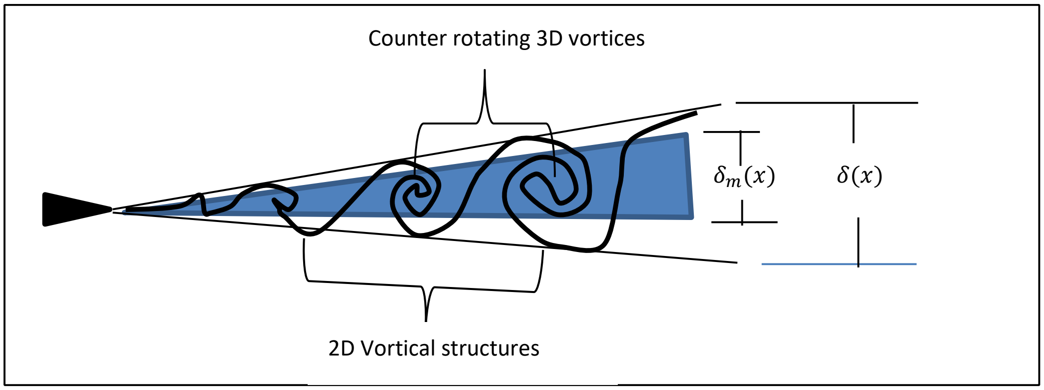

Figure 2.5 Evolution of 2 and 3D vertical structures in the mixing layer *(Dimotakis, 1991)*

Figure 2.6 Large scale motion of entrained fluid with little or no mixing *(Dimotakis, 2005)*

`

Of interest in combustion process is mixing at molecular scale because chemical reaction cannot take place outside of this scale. This requires the species to interact and diffuse into one another on a molecular level and the resultant small interfacial area due to 2D turbulence limits the rate at which this diffusion can occur (Lorenzo, 2008).

In contrast with 2D, 3D turbulence has a broad spectrum of eddying scales (Dimotakis, 2005). Therefore energy is transferred to smaller scale in a sequence of forward cascade due to continuous stretching and folding with energy dissipated at the smallest scale by viscous forces (Ecke, 2017). For improved mixing, 3D *counter rotating streamwise vortices* must be developed and sustained in the layer and condition for this to happen is a critical Re of approximately 2.3×10^4 (Dimotakis, 1991). This vortical structure transitions to fully developed 3D turbulence which breaks down the large structure into molecules by sequence of forward cascade increasing the interfacial area between the fluid species (Figure 2.7) and enhancing molecular mixing. It is important to note that Re here is based on local shear layer thickness and velocity difference as defined in Eqn. (2.1)

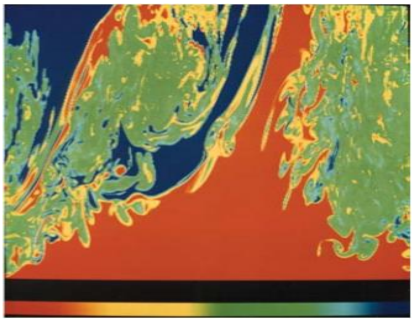

Figure 2.7 Enhanced mixing due to increase in interfacial area between fluid species *(Dimotakis, Turbulent Mixing, 2005)*

If the initial condition is perturbed so that this critical Re is attained early, the molecular mixing of fluids can take place at location very close to the origin- almost as soon as they are drawn into the shear layer

`

(Dimotakis, 1991). Therefore, the location of the mixing transition can be adjusted by varying the level of perturbation in initial conditions of the layer-an understanding which can be applied in the design of more compact mixing or combustion system.

Since molecular mixing depends on diffusion following viscous dissipation at the smallest scale, then it can be argued that the mixed fluid fraction depends on the fluid Schmidt number(Sc).

$$Sc = \frac{\nu}{D} \tag{2.4}$$

Where ν is the kinematic viscosity and D the diffusivity of the mixing species

2.9 Development and Interaction of Vortices

The LIF photograph of jet flow in Figure *2.3* shows a series of vortex rings that grew in size due to pairing and disintegrated downstream of the nozzle. The structure in Figure *2.8* attached to the potential core that looks like a finger roll around the vortex ring in the braid region is the secondary vortex (Liepmann & Gharib, 1992). The secondary vortex has an irregular core Figure 2.8(middle). The protuberances are the streamwise vortices at a formative stage. The core of the primary vortex or ring cross-section -Figure 2.8 (left) is regular, with a dark ring, which is the entrained surrounding fluid in between. The core is symmetric due to streamwise vortex attenuation in the braid region (Liepmann & Gharib, 1992).

The images of the braid area at $X/D = 3.5$ (Figure 2.9) Figure *2.9*showed a more developed structure. The ring cross section showed protuberances and azimuthal instabilities which are in phase with the streamwise vortex pairs of the (1992)braid region. Spatial and structural mapping of the streamwise vortices with the protrusion showed a close match, hence the conclusion that the observed protuberances in the ring section were the streamwise vortices that developed in the braid region (Liepmann & Gharib, 1992).

`

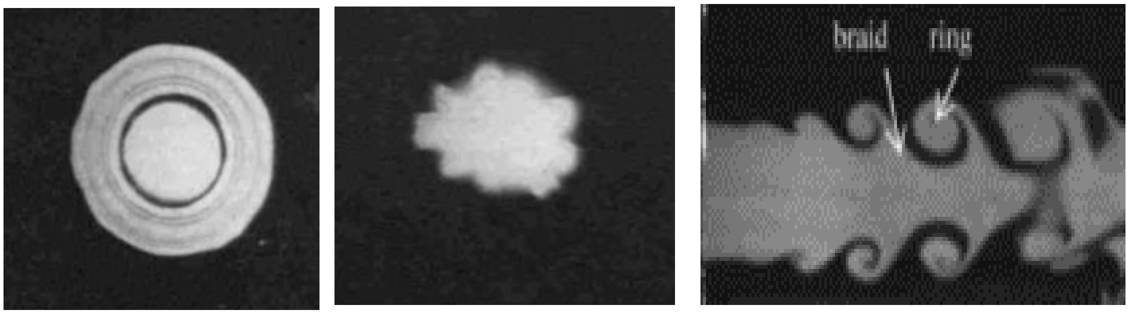

Figure 2.8 LIF visualization of jet flow- (left) Transverse plane image of the ring cross-section at $X/D = 2.25$ - (middle) Transverse plane image of the braid region at $X/D = 2.25$ *(Liepmann & Gharib, 1992)* and (right) side view *(Nastase, Meslem, & Gervals, 2008)*

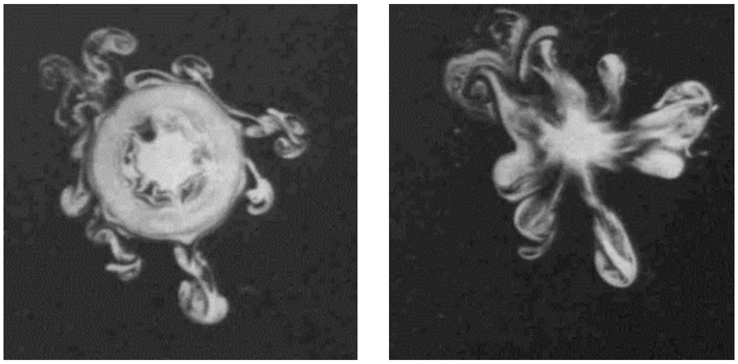

Figure 2.9 Transverse image of the ring (left) and the braid (right) cross sections at $X/D = 3.5$

2.10 Control

Shear or mixing layers and their defining turbulent structures develop from the initial instability at the contact surface due to differences in the velocity of the fluids. If the initial flow condition is perturbed or excited, say by changing the geometry of the trailing edge of the nozzle or splitter plate, the resulting flow will behave differently. The shear layers do not have a unique growth rate but rather an amplifier of

`

externally imposed disturbances, which can be manipulated or controlled. The in-flow conditions are a function of the level and the nature of fluctuations associated with the boundary layer upstream (Slessor, Bond, & Dimotakis, 1998). Boundary layer parameters include momentum thickness (θ), boundary layer thickness (δ), boundary layer displacement (δ^*), Skin friction (C_f), shape factor (H), and friction velocity (u_f) (Rengasamy & Alakesh, 2017).

Shear layers are modified using methods described in literature as active techniques (Reynolds, Parekh, Juvet, & Lee, 2003) & (Mohsen, 2011) and passive techniques (Zaman, Reeder, & Samimy, 1994), (Behrouzi & McGuirk, 2006), (Chen, Hayes, & Fletcher, 1999), (Rajagopalan & Antonia, 2007) and (Sadeghi & Pollard, 2012). In an active method, external energies are superimposed periodically on the mean flow. Turbulence is enhanced or reduced depending on the phase, amplitude, and frequency of the disturbance imposed. The actuators include acoustic speakers, vibrating springs, piezoceramic elements, and pulsed and steady fluid tabs. Devices for Passive control are trip rings, tabs, and slender bluff bodies at the nozzle exit. Others include the chevron nozzle or tabs in combination with the chevron nozzle.

Strouhal number ($St = fD/U$), quantifies the near field instability/disturbance (f is the excitation frequency, D is the nozzle diameter, and U is the center line or the average jet exit velocity). St is also computed based on Kelvin-Helmholtz instability frequency f_0 and boundary layer momentum thickness θ. $St_\theta = f_0\theta/U$ (Rajagopalan & Antonia, 2007). The values of St or St_θ indicate the magnitude of turbulence amplification or suppress (Sadeghi & Pollard, 2012)ion. At the jet's preferred mode i.e. St or St_θ values ranging from 0.3-0.56 the shear layer growth rate, turbulence intensity, and mixing (Reynolds, Parekh, Juvet, & Lee, 2003), (Rajagopalan & Antonia, 2007)and (Sadeghi & Pollard, 2012). There is stable pairing at St_θ ranging from 0.01 to 0.018, where the vortical structure is weak because the wake introduced a canceling effect or suppressed the large vortices in the shear layer. The consequence is the

`

reduction in the shear layer width, early breakdown of the shear layer vortex core, and quick transition to full-scale turbulence.

.

2.10.1 **Active control**

Reynolds, Parekh, Juvet, and Lee (2003) obtained a bifurcating and blooming jet by axial and helical excitation. The excited jet had a higher mixing capacity, and the modification was for jet engine exhaust control (Figure 2.10). The axial excitation by acoustic forcing or axisymmetric mechanical agitation upstream of the nozzle altered the vortex ring spacing. The helical excitation obtained by wobbling the nozzle, on the other hand, offsets the successive rings from the average position.

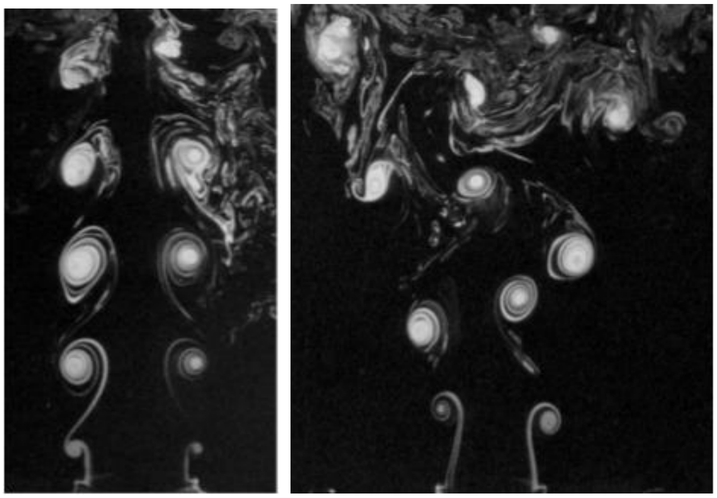

Figure 2.10 Ring vortex structures formed due to different types of perturbation by an air jet at Re=10000 (left) Axial forcing and (Right) combined axial and helical forcing (Reynolds, Parekh, Juvet, & Lee, 2003)

The vortical structures on the left and right of Figure 2.10 were obtained by axial forcing and combined axial and helical forcing, respectively, at $St_a = f_{axial}D/U = 0.55$ (where f_{axial} is the axial forcing frequency). The far-field profile was a product of the two excitation techniques and a function of the axial

`

and helical forcing frequency ratio ($r_f = f_{axial}/f_{helical}$). The jet will bifurcate at $r_f = 2$ (Figure 2.11), at values slightly different from 2 bifurcations occurred in addition to slow precession of the bifurcation plane around the nozzle axis, at $r_f = 3\ or\ 4$, the jet divided into three or four vortex streams, and bloomed when r_f is an irrational multiple of circumferential or orbital frequency (Figure 2.12).

Figure 2.11 Bifurcating water Jet at Re=4300 (Reynolds, Parekh, Juvet, & Lee, 2003)

Figure 2.12 Blooming water Jet at $Re \approx 20000$ (Reynolds, Parekh, Juvet, & Lee, 2003)

Faivre & Poisnot (2020) increased the spread angle of a jet by radial injection of fluid. The idea was to induce swirl or streamwise vortices in the flow to enhance mixing. The discovery by Faivre and Poisnot (2020) was that the intensity of the vortices impacted and consequent spread/ mixing is proportional to the momentum flux ratio of radial to main jet i.e., the momentum flux and swirl intensity due to radial fluid injection into the main jet will be higher for lighter gases if the mass flow rate is constant.

Also affecting the spread are the exit diameters (d) of the radial injectors, their orientation relative to the main jet (α), and the distance (h) between the radial injector and the main jet exit (Figure 2.13). A radial fluid injected at 90° introduced azimuthal velocity only and produced the maximum swirl in contrast to axial and azimuthal velocity components at other orientations. In addition, small h values because of the vanishing effect of wall confinement and friction gave a better spread.

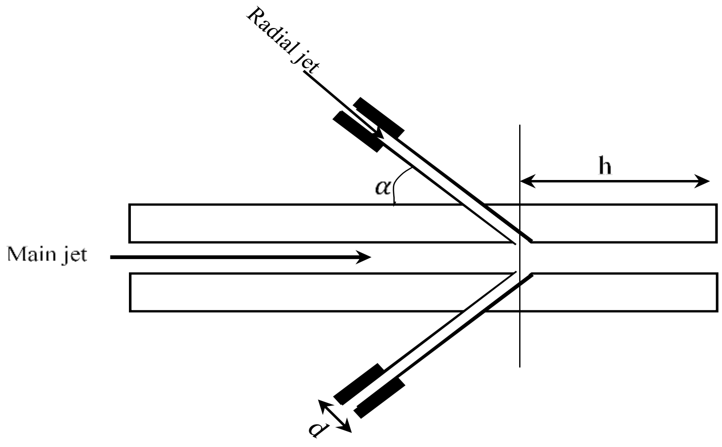

Figure 2.13 Radial/main jet configuration

`

2.10.2 Passive Control

Passive devices like trip rings, tabs, lobs, and slender bluff bodies installed at the nozzle trailing edge can alter the interaction of the vortices.

Use of Tabs, lobs, and chevron nozzle

Nastase, Meslem, and Gervais (2008) investigated the evolution of primary and secondary vortices in round and cross-shaped lobed jet (2008)s. The result showed a strong correlation between the periodic fluctuation in the entrainment rate and the passage of the ring structures (Figure 2.16). The minimum entrainment rate coincided with the passing of the ring Figure 2.14because of the attenuation of streamwise vortices (Liepmann & Gharib, 1992).

The cross-shaped lobed jet Figure *2.15* has an edge over the round nozzle in terms of entrainment. The PIV images of the lobed nozzle (Figure 2.17) showed a core indentation, a periodic ring dearth, and persistent streamwise vortices that guaranteed continuous entrainment.

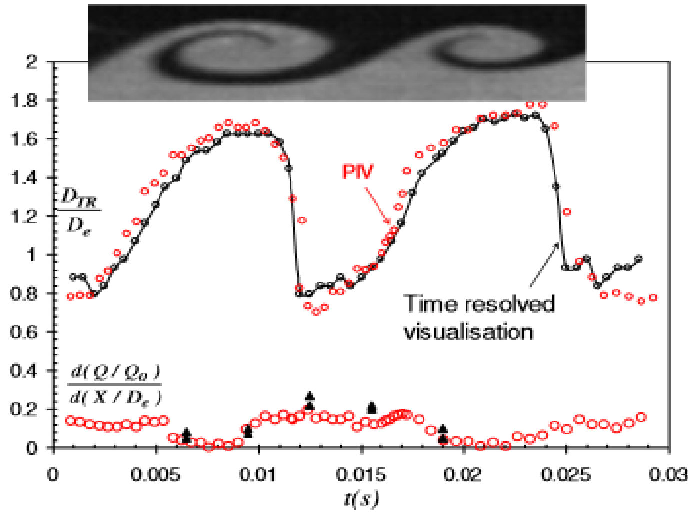

Figure 2.14 reconstructed vortex ring passing in a round jet and its correlation with instantaneous entrainment rate (Nastase, Meslem, & Gervals, 2008).

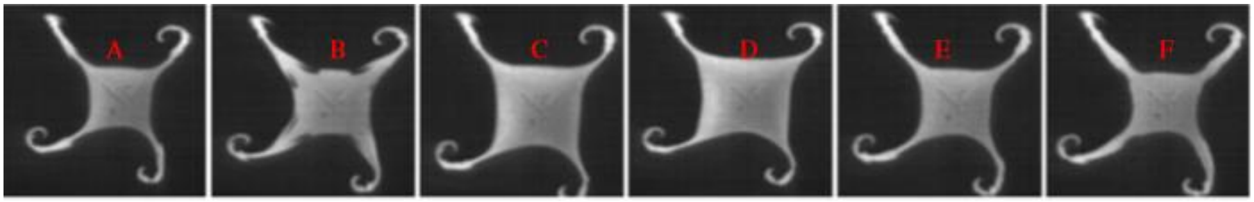

Figure 2.15 Series of PIV Images of cross-shaped lobed jet cross section at $X/D = 3$ *(Nastase, Meslem, & Gervals, 2008)*

Serrated (chevron) and tabbed round nozzle have similar indentation as lobes (Subramanian, et al., 2018); (Behrouzi & McGuirk, 2006), (Reeder & Samimy, 1996), and (Zaman, Reeder, & Samimy, 1994). The lobes caused a stretching of the mixing layer (Zaman K. B., 2001). Serration or tabs in round nozzles generated a counter-rotating pair of streamwise vortices and distorted jet core (Callender, Gutmark, & Martens, 2008) (Zaman, Reeder, & Samimy, 1994).

For a given blockage ratio, a delta tab installed at the trailing edge of the nozzle (Figure 2.16) is the most effective in distorting or causing indentation to the jet core with a corresponding increase in mixing and centerline velocity decay rate (Zaman, Reeder, & Samimy, 1994). The number of delta tabs around the nozzle and their protrusion into the boundary layer is critical for performance.

Four tabs spaced equally around the nozzle lip produced the most distortion, spread, entrainment, and mixing. Anything more or less was less effective. The flow instability heightened at tab numbers exceeding four (Zaman, Reeder, & Samimy, 1994). The results were similar for the chevron nozzle with more than four serrations (Figure 2.17). The magnitude of the core indentation reduced progressively with the number of serrations (Nandita, Sruthi, Suriyaprabha, Sundaram, & Arun, 2018). Figure *2.17* Subramanian et al. (2018) showed that the indentations endured farther downstream (2018)with tabs at the tip of the serration (Figure 2.19- right).

The optimum position for the tabs was at the lip. A small gap between the lip and the delta tab made it less effective. Tab height higher than the boundary layer thickness helps for deeper core indentation, especially in turbulent boundary layer (Zaman, Reeder, & Samimy, 1994).

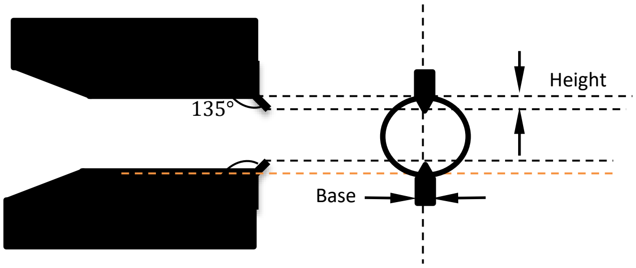

Figure 2.16 Delta tabs

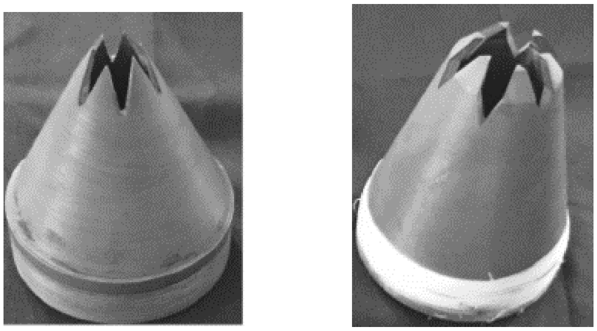

Figure 2.17 Six-tooth Chevron nozzle configuration: (left) - conventional chevron nozzle, (right)- Tabbed chevron nozzle (Subramanian, et al., 2018)

Passive Rings\Trips

Sadeghi and Pollard (2012) investigated the coherent structure modification with passive rings. The rings in the shear layer ($0.466 \leq r/D \leq 0.486$) and the potential core $0.407 \leq r/D \leq 0.427$) affected the flow differently. Spectra measurement in the shear layer ($r/D = 0.476$) of a free jet at various positions downstream showed stable vortex pairing activity. This appears as peaks at near submultiples of the roll-up frequency. With the rings in the shear layer, the flow transited early to full-scale turbulence. The initial roll-up was at the same frequency but lower amplitude as the free jet, which signals a suppression of the coherent structure by the ring. There was also a surppression of the vortices with the passive ring in the potential core but at a lower scale (Rajagopalan & Antonia, 2007).

2.11 Effect of Confinement

Flow through ejectors and caverns are confined in a low aspect ratio duct. The boundary conditions of the confinement can cause significant changes in the flow behavior, some of which include the rate of decay of the center line velocity and the formation of a recirculation zone between the jet and the walls of the confining duct (Voropayev, Sanchez, Nath, Webb, & Fernando, 2011). If both or one end of the confinement is closed, the jet will break up totally a short distance from the origin due to an adverse pressure gradient and oscillate with uniform frequency (Liberzon & Fernando, 2014). The breakup point depends on factors like jet spread and the ratio of the confining tube to nozzle diameter (D/d). A low spread angle extends the break up point but a low D/d reduces it (Subramanian, et al., 2018)

Craya-Curtet number C measures the (Liberzon & Fernando, 2014)possibility of recirculation occurrence in a confined flow (Khodadadi & Vlachos, 1988) and (Revuelta, Martinez-Bazan, Sanchez, & Amable, 2004)

$$C = \frac{U_m}{\left[\left({u_j}^2 - {u_s}^2\right)a^2 + 0.5\left({u_s}^2 - {U_m}^2\right)\right]^{1/2}} \qquad (2.5)$$

Where U_m is the mean velocity in the mixing tube given as $U_m = \left(u_j - u_s\right)a^2 + u_s,$ a is the ratio of the nozzle to confining tube diameter, while u_j and $u_s$we are the mean velocities of the jet and secondary stream, respectively.

`

Craya-Curtet number relates to the ratio of momentum flux of secondary fluid to that of the primary jet as (Revuelta, Martinez-Bazan, Sanchez, & Amable, 2004)

$$C = \left(J_s/J_j\right)^{1/2} \tag{2.6}$$

Where J_s and J_j, respectively, are the momentum flux of the secondary stream and the jet.

The critical Craya-Curtet number (C_c) for uniform and parabolic flows are 0.65 and 0.77, respectively. For $\mathrm{C} > C_c$, the flow will remain aligned with the axis, indicating the absence of adverse pressure gradient and the associated toroidal recirculation.

2.12 Combustion Theories

Designers of combustion equipment focus mainly on the safe conversion of chemical energy in fuels to heat and work and minimal release of toxic combustion products to the environment. To effectively achieve this, an understanding of combustion theories is necessary.

Combustion involves the molecular mixing of fuel and oxygen in an oxidation process to produce flame, light and heat. The immediate consequence of this reaction is the rise in temperature. Temperature and combustion product composition are functions of the oxygen/fuel ratio and their mixedness and are critical in combustion system (Irvin & Richard, 2008). Combustion system classifications based on molecular mixing are premixed and non-premixed. In premixed systems, the reactants are well mixed before the initiation of the combustion while, in non-premixed or diffusion combustion systems, the reactants combination is by diffusion and bulk convective motion at the (Chung, 2006). Other forms of classification include laminar and turbulent depending on the nature of the flow, subsonic and supersonic

`

subject to the velocity of flow, and homogenous and heterogenous based on whether or not the reacting species are in the same phase- say gas-gas, gas-solid, liquid-liquid, liquid-solid e.t.c.

If the heat released during combustion serves only to increase the temperature of the combustion product, then the temperature known as adiabatic flame temperature (T_{ad}) is estimated based on fundamental principles. T_{ad} indicates the rate at which the combustion reaction progresses and the potential of the reactive species to deliver heat and power (Chung, 2006).

The combustion equation is critical in the combustion products and T_{ad} analysis. The combustion equation gives a general overview of the reacting species interaction and the rearrangement of their molecules to form elements with different chemical properties. Though the chemical properties of the reactants differ from the products, there is a conservation of the mass of reacting species as the number of atoms for the reactant and the product is the same.

Chemical equations convey two basic information- the composition of the reactants and products and their amount. The fuels are basically hydrocarbons comprising mainly hydrogen, carbon, oxygen, and other nonreactive elements. The oxygen supplied from the atmosphere is the oxidizer. The air composition by volume is approximately 21% oxygen and 79% nitrogen or 23.3% oxygen or 76.7% nitrogen by mass.

Air is available in nature and attractive for use in most combustion systems. The temperature and flame intensity in systems using air lower than those using only oxygen because the inert nitrogen

absorbs some of the heat of combustion. The chemical equation for the oxygen/hydrogen reaction is

$$H_2 + \frac{1}{2}O_2 \rightarrow H_2O \qquad (2.7)$$

`

1 mole of H_2 reacts with 0.5 mole of O_2 to form 1 mole of H_2O. The state (vapor or liquid) of the H_2O formed is a function of the imposed temperature.

Similarly, O_2 reacts with carbon to form either CO_2 or CO. The equations for both scenarios respectively are;

$$C + O_2 \rightarrow CO_2 \tag{2.8}$$

$$C + \frac{1}{2}O_2 \rightarrow 2CO \tag{2.9}$$

Similarly, any combustion reaction involving hydrocarbon fuels will produce $H_2O\ and\ CO_2$ if the supply is of stoichiometric value or CO if less. When the oxygen is above the stoichiometric value, the excess oxygen passes with the combustion product. The O_2 available in fuel, takes part in combustion and reduces the oxygen requirement from the air.

CFD is a computer-based simulation tool for fluid flow, heat transfer, and combustion reaction analysis (Versteeg & Malalasekera, 2007). In order to improve efficiency, there is a need to interrogate the burner variables. Achieving this through experiments will require the construction of multiple physical prototypes, which is expensive. CFD can create a virtual prototype and solve numerically the governing equations for fluid flow, heat, and mass transfer at a short lead time.

CFD provides comprehensive flow information over the entire flow domain, at variance to experiments limited to the points installed with the measuring device (Abdulnaser, 2009). In addition, simulation with CFD is at the correct scale and the actual operating condition, eliminating the need for unnecessary extrapolations.

`

Table 2.1 shows some CFD Table 2.1capabilities. There are no universal models that handle all the problems. In order to select the appropriate model for a particular flow problem, a deep understanding of the physics and theories of fluid dynamics models and their limitations is essential. An arbitrary approach to model selection will cast a shadow on the reliability of the CFD result.

Table 2.1 List of possible simulations in CFD (Bengt, et al., 2012)

Flow	**Mass Transfer**	**Heat Transfer**
Laminar	Convection	Conduction
Turbulent	Diffusion	Convection
Single-phase	Reaction	Radiation
Multi-phase	Phase transfer	

The governing equations are the conservation of mass momentum and energy laws. These are partial differential equations (PDE). The numerical solution procedure starts with domain discretization, followed by conversion of the PDEs to sets of algebraic equations at discrete points and solving them with digital computers.

The discretization techniques are finite volume, finite element, and finite difference methods. Others are spectral methods, boundary element, vorticity-based methods, lattice gas/lattice Boltzmann, etc. The finite volume method is the most popular and is used in 80% of commercial CDF codes, followed by finite elements (15%) and the rest (Andre, 2006).

`

2.13 Computational Fluid Dynamics (CFD)

The popular CFD codes are Fluent, CFX, Star-CD, Flow-3D, phenolics, and Open Foam. Open foam is a high-performance open-source program with a poorly developed user interface and documentation (Bengt, et al., 2012).

All commercial CFD codes have the pre-processor, the solver, and the post-processor to aid data input and result analysis.

The pre-processor includes the drawing and meshing modules. The domain is created in the drawing module and transferred to the meshing module for discretization into subdomains or cells. The governing flow equations are converted into algebraic equations in the cells and solved iteratively.

The accuracy of the solution largely depends on how well the meshes are applied. Finer cells often yield better results, albeit costly per time and computer hardware. For optimal performance, cells are usually finer in areas with a likelihood of significant variations and coarse in regions prone to little changes.

The choice of the flow model, the definition of the thermo-physical properties of the fluid, the specification of the boundary conditions and the iteration happen in the solver.

At the end of the iteration process, the result appears in the post-processor as lines, contours, vectors, 2D surface plots, and streamlines. The alteration of the display coordinate and the result export to other programs for further manipulation are some of the features of the post-processor.

2.14 Summary of the Findings from the Literature Review

This review surveyed the nozzle venturi arrangements for primary air induction in natural draft burners. Also reviewed were the entrainment mechanism and the jet structure control/modification procedures. Here also are existing works on combustion, flame stability, and the flow dynamics in natural draft burners

`

. The interest was venturi geometry and gas nozzle position to optimize primary air entrainment and mixing. The research methodologies were CFD analysis, 1D modeling, and experiments. CFD produced robust results that compared well with experiments. It has the capacity to provide a visual outlook of the flow behavior in the entire domain compared to localized data from probes placed at specific points.

There was a documentation of theories of jet structure modification using passive and active options (Reynolds, Parekh, Juvet, & Lee, 2003) (Subramanian, et al., 2018). None of the reviewed works paid attention to jet structure modifications and optimum air entrainment and mixing in ejectors, hence the need to carry out a parametric study of the unit. The experimental approach at this stage would be expensive, making analytical and CFD options very attractive. A good number of the documented studies paid attention to axial flow only. However, the radial velocity profile along the jet can also provide information about the extent of mixing in the system.

`

CHAPTER 3

3 METHODOLOGY

3.1 The Structure of a Natural Draft Burner Unit

The schematic of the configuration of a natural draft burner unit is in Figure 3.1. The burner consists primarily of the fuel inlet, the air inlet, the throat, the mixing zone, and the burner head. All natural draft burners have similar structures and operating principles and are described clearly in Figure 3.1.

The operating pressure range is 1.724 to 2.0 kPa for natural gas and 2.5 to 2.75 kPa for LPGs (Robert, 2010). As the gas flows through the throat, which serves as a convergent/divergent nozzle, the velocity of the gas increases while the pressure drops below that of the ambient. The negative pressure at the throat draws atmospheric air into the system. The air entrainment and the mixing with the fuel continue in the diffuser/mixing zone. The diffuser design, therefore, must guarantee a homogenous supply of air /fuel mixture to the burner head before ignition.

`

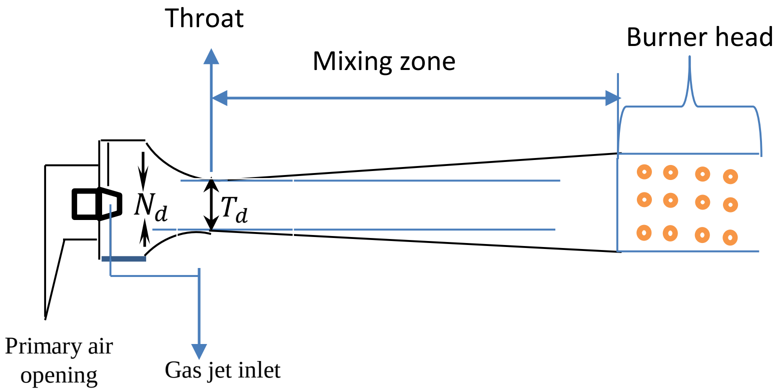

Figure 3.1 The configuration of a natural draft burner unit

3.2 Model Development

Here is an attempt to develop some mathematical models for the analysis of flow dynamics both in free and confined jet systems using the momentum conservation principles. This will include models to compute the radial velocity profile at different axial locations, the axial volumetric flux, and entrainment velocity.

3.2.1 Simplifying Assumptions

- The first assumption is the momentum conservation between the motive fluid and the surrounding air. The aim was to simplify the computation process by negleting frictional losses and drag.

`

- The second was the assumption that the flow was incompressible and does not separate or recirculate. This is because of the mild streamline curvature, a relatively low primary stream velocity and also the computed Mach number M was $\ll 1$
- The jet spread takes the form of a wedge, and the nozzle exit diameter which is the actual flow origin is greater than zero hence assumption that the flow origin is at a virtual location O inside the nozzle
- The radial velocity has a normal profile and can be modelled using a Gaussian equation.

3.2.2 Free /Unconfined jet

I. Model for Velocity Profile at Different Axial Locations

A schematic representation of the velocity profile in unconfined jet flow is in Figure 3.2. It follows from the figure that the thickness or radius of the jet r is a function of downstream distance x and the angle $\emptyset$

$$r = x\, tan\, \emptyset \qquad (3.1)$$

r is the radial distance from the jet centreline to the point known as velocity half width where $u = 0.5u_{max}$ (Ghahremanian & Moshfegh, 2011). Considering that the initial radius of the jet is higher than zero, the measurement of the axial distance x starts from a virtual origin x_0 inside the nozzle.

The mean velocity of the jet at different axial coordinates from the nozzle exit showed that at locations very close to the nozzle, the velocity profile is more like a top hat (Liepmann & Gharib, 1992). Further downstream, the shape evolves to Gaussian because of air entrainment (Pope, 2000), (Reeder & Samimy, 1996) (Labus & Symons, 1972).

`

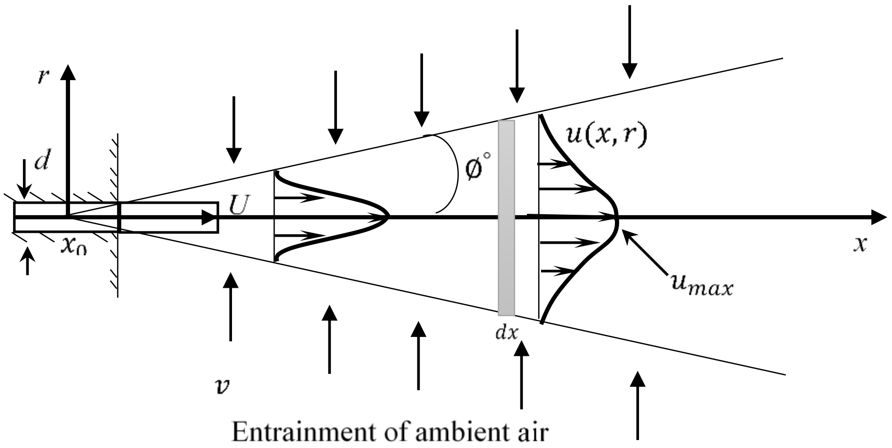

Figure 3.2 Schematic description of the radial velocity profile of axisymmetric jet at different axial positions

The radial velocity profile of a jet in a fully developed or self-similar region is bell-shaped (Figure 3.3), and the model approximates a Gaussian function of the form.

$$y(x) = ae^{-\left(\frac{(x-b)^2}{c}\right)} \tag{3.2}$$

Where the maximum value of $y(x)$ occurs at $x = b$, $c = 2\sigma^2$ where σ is the standard deviation and controls the curve width or spread across the centreline

`

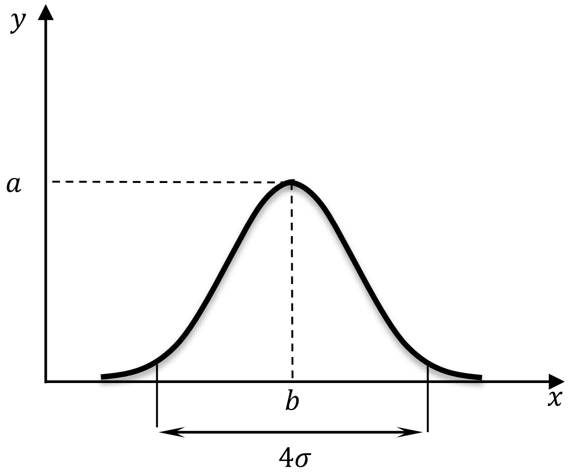

Figure 3.3 Bell curve

The line of Figure 3.2symmetry is at $b = r = 0$ for a Gaussian function (Figure 3.2), the model for velocity profile is

$$u(x,r) = u_{max}e^{-\left(\frac{(r)^2}{2\sigma^2}\right)} \qquad (3.3)$$

From statistics, 95% of the area of the curve has a width length of approximately 4σ hence

$2r \approx 4\sigma$, therefore, half the width of the profile is $2\sigma = r$

It follows from Eqn. (3.1) that

$\sigma = 0.5x\, tan\, \emptyset$ which can be substituted into Eqn.(3.3) to give

$$u(x,r) = u_{max}e^{-\left(\frac{(r)^2}{0.5x^2 tan^2 \emptyset}\right)} \qquad (3.4)$$

The momentum flux equation is

$$\dot{m}u = \rho A u^2 \qquad (3.5)$$

`

Where ρ, A, and u, respectively, are the density, cross-sectional area, and average velocity of the fuel/air mixture.

Integration of $\rho A u^2$ over the jet cross-section $2\pi r$ will state the conservation of momentum as

$$\int_{\mathbf{0}}^{r} \rho u^2 2\pi r dr \; = \rho_f {u_f}^2 \pi R^2 \tag{3.6}$$

Where R, ρ_f, *and* u_f, respectively, are the radius of the fuel nozzle, the fuel density, and the mean velocity of the fuel at the nozzle exit.

Calculating the integral and simplifying gives

$$\rho u^2 \pi r^2 = \; \rho_f {u_f}^2 \pi R^2 \tag{3.7}$$

$$u = u_f \frac{R}{r} \left(\frac{\rho_f}{\rho}\right)^{1/2} \tag{3.8}$$

From Eqn. (3.1), $\mathrm{r} = \mathrm{x} \tan \emptyset$.

Therefore Eqn. (3.8) can be written as.

$$u = u_f \frac{R}{(x \, tan \, \emptyset)} \left(\frac{\rho_f}{\rho}\right)^{1/2} \tag{3.9}$$

Substituting Eqn. (3.8) into Eqn. (3.4)

$$u(x, r) = u_f \frac{R}{(x \, tan \, \emptyset)} \left(\frac{\rho_f}{\rho}\right)^{1/2} e^{-\left(\frac{(r)^2}{0.5 x^2 tan^2 \emptyset}\right)} \tag{3.10}$$

$$u_{max} = u_f \frac{R}{(x \, tan \, \emptyset)} \left(\frac{\rho_f}{\rho}\right)^{1/2} \tag{3.11}$$

`

The inverse of centreline velocity standardized by the average velocity at nozzle exit is;

$$\frac{u_f}{u_{max}} = \frac{x}{R}\left(\frac{\rho}{\rho_f}\right)^{1/2} tan\,\emptyset \tag{3.12}$$

II. Model for axial volumetric flux

The volumetric flux Q of the jet increases downstream due to continuous air entrainment.

$$Q = u\pi r^2 \tag{3.13}$$

or

$$Q = \pi u_f R\left(\frac{\rho_f}{\rho}\right)^{1/2}(x\,tan\,\emptyset) \tag{3.14}$$

Similarly, the volumetric flux of fuel q is

$$q = u_f A_f \tag{3.15}$$

The volume and mass flux of air, respectively, are

$$\dot{v}_a = Q - q \tag{3.16}$$

$$\dot{m}_a = Q\rho - q\rho_f \tag{3.17}$$

From Eqn. (3.16) and Eqn. (3.17) the density of air ρ_a can be written as

$$\rho_a = \frac{Q\rho - q\rho_f}{Q - q} \tag{3.18}$$

ρ is unknown and can be replaced as

`

$$\rho = \rho_a + \frac{q}{Q}\left(\rho_f - \rho_a\right) \tag{3.19}$$

Substituting the value of ρ in Eqn. (3.19) into Eqn. (3.14)

$$Q = \pi u_f R \left(\frac{\rho_f}{\rho_a + \frac{q}{Q}\left(\rho_f - \rho_a\right)}\right)^{1/2} (x \tan \emptyset) \tag{3.20}$$

The expansion of Eqn. (3.20) gives

$$Q^2 \rho_a - Qq\left(\rho_a - \rho_f\right) - \pi^2 {u_f}^2 R^2 x^2 \tan^2 \emptyset = 0 \tag{3.21}$$

If

$a = \rho_a$

$b = -q(\rho_a - \rho_f)$

$c = -\left(\pi^2 {u_f}^2 R^2 \rho_f x^2 \tan^2 \emptyset\right)$

It becomes clear that Eqn. (3.21) is a quadratic equation of the form

$$aQ^2 - bQ - c = 0 \tag{3.22}$$

The solution of Eqn. (3.21) will give

$$Q = \frac{q\left(\rho_a - \rho_f\right) + \sqrt{q^2\left(\rho_a - \rho_f\right)^2 + 4R^2 {u_f}^2 \rho_a \rho_f \pi^2 x^2 \tan^2 \emptyset}}{2\rho_a} \tag{3.23}$$

The entrainment rate E is the rate at which the volumetric flux grows with distance downstream of the flow.

$$E = \frac{dQ}{dx} = \pi u_f R \left(\frac{\rho_f}{\rho}\right)^{1/2} \tan \emptyset \tag{3.24}$$

`

III. Entrainment Velocity Model

The conservation of Q over an area dA along x is

$$dQ = udA \tag{3.25}$$

Where $dA = 2\pi rdx$ it follows that

$$dQ = u2\pi rdx \tag{3.26}$$

and

$$\frac{dQ}{dx} = u2\pi r \tag{3.27}$$

Where

$$u = \frac{u_f R}{2x\, tan\, \emptyset}\left(\frac{\rho_f}{\rho}\right)^{1/2} \tag{3.28}$$

3.2.3 **Confined Jet/Ejector Models**

An ejector consists of a confining tube with varying cross-sectional areas. The primary features of an ejector are the inlet, the throat, and the diffuser. At the throat, the velocity of the primary or motive fluid must increase because of mass conservation with a consequent pressure drop. The negative pressure at the throat causes suction and the velocity difference between the streams will cause the entrainment of atmospheric air into the jet stream. Both streams mix in the diffuser as the flow progresses. In the diffuser, the velocity of the mixed stream will again drop and its pressure rise.

`

In the ejector, there is a conservation of momentum, and the fuel injection into the system relates to the mixture flow rate using the geometric parameters of the venturi (Glassman & Yetter, 2008). The assumption here is that the jet takes the form of the ejector.

$$\dot{m}u = \dot{m}_f u_f \tag{3.29}$$

Where

$\dot{m}$ is the mass flow rate of the air/fuel mixture

$\dot{m}_f$, the mass flow rate of fuel

u, velocity of the mixture

u_f, fuel velocity.

$\dot{m} = \rho u A^*$; $\dot{m}_f = \rho_f u_f A_f$

A^* is the port area or area at the end of the mixing tube. A_f, is the cross-sectional area of the fuel nozzle at the exit.

For conservation of momentum, Eqn. (3.29) holds

$$\rho A^* u^2 = \rho_f A_f {u_f}^2 \tag{3.30}$$

From Eqn. (3.30)

$$\frac{u^2}{{u_f}^2} = \frac{\rho_f A_f}{\rho A^*} \tag{3.31}$$

and

$$\frac{u}{u_f} = \left(\frac{\rho_f}{\rho}\right)^{1/2} * \left(\frac{A_f}{A^*}\right)^{1/2} \tag{3.32}$$

`

The ratio of the volume of air to fuel in the mixture is

$$\frac{Q-q}{q} = \frac{uA^* - u_f A_f}{u_f A_f} = \frac{uA^*}{u_f A_f} - 1 \tag{3.33}$$

where *Q*, and *q*, respectively, are the mixture(fuel/air) and fuel volume.

From Eqn. (3.32)

$$\frac{u\mathrm{A}^*}{u_f A_f} = \left(\frac{\rho_f}{\mathrm{\rho}}\right)^{1/2} \left(\frac{A_f}{\mathrm{A}^*} * \frac{{\mathrm{A}^*}^2}{{A_f}^2}\right)^{1/2}$$

$$\frac{uA^*}{u_f A_f} = \frac{Q}{q} = \left(\frac{\rho_f}{\rho}\right)^{1/2} \left(\frac{A^*}{A_f}\right)^{1/2} \tag{3.34}$$

Therefore, the volumetric air/ fuel ratio will be

$$\frac{A}{F} = \frac{Q-q}{q} = \left(\frac{\rho_f}{\rho}\right)^{1/2} \left(\frac{A^*}{A_f}\right)^{1/2} - 1 \tag{3.35}$$

From Eqn. (3.18) and Eqn. (3.19), the density of air and the mixture ρ is

$$\rho_a = \frac{Q\rho - q\rho_f}{Q-q}$$

and

$$\rho = \rho_a + \frac{q}{Q}\left(\rho_f - \rho_a\right)$$

Substituting ρ into Eqn. (3.35) and solving for Q will give

`

$$Q = \left[\frac{q(\rho_a - \rho_f) + \sqrt{q^2(\rho_a - \rho_f)^2 + \frac{4A^*\rho_a\rho_f q^2}{A_f}}}{2\rho_a} \right] \tag{3.36}$$

If there are no adverse pressure gradients in the mixing tube and the resistance to flow is only due to wall friction, the.equation for the free jet can also describe the flow through ejectors (Voropayev, Sanchez, Nath, Webb, & Fernando, 2011) and (Lee, 2015). Hence, the system analysis using Eqn. (3.23)- the free jet flow and Eqn. (3.36) will yield a similar result.

In carrying out the above analysis, some of the.assumptions made were that the transfer of momentum of gas fuel to the surrounding air occurred without losses due to friction and drag. The second was that the molecular mixing of air and fuel is complete so that all the air entrained takes part in combustion.

It follows that the initial flow conditions and the ejector geometry are critical. For example, the mixing tube length should be as short as possible to reduce losses due to friction and allow for a compact design yet long enough to allow time for complete mixing. Similarly, turbulence enhances mixing, but at the inlet, turbulence will reduce the entraining capacity of the system due to the dissipation of kinetic energy that otherwise would have been used for entrainment. The flow will separate and recirculate if the throat curvature is steep, but the seamless flow may entail longer curvatures with the chances of frictional loss in the system. The initial flow conditions, the diffuser length, curvatures, and the relative dimensions of the mixing tube are critical to the system performance hence the need for correction factor.

A detailed empirical investigation is expensive in addition to the fact that the optimal geometry of an ejector may vary with application. This requires a fresh experiment per time, which is not feasible. CFD therefore is a cheaper investigative approach.

`

3.2.4 **Performance Criterial**

Reynolds number (Re), Mach number (Ma), and vorticity(w) are some of the variables that define the flow through the ejector.

Reynolds number (Re)

$Re = \frac{\rho UD}{\mu}$ affect entrainment and mixing, where ρ, U, and μ, respectively, are the density, velocity, and dynamic viscosity of the motive fluid, and D is the diameter of the nozzle. Ideally, high Re number, should translate to. better the entrainment and mixing. However, turbulence is associated with a high Re number, which reduces entrainment when present at the origin due to kinetic energy dissipation.

Mach number (Ma)

Mach number is given by;

$$Ma = \frac{U}{C} = \frac{U}{\sqrt{\gamma RT}} \tag{3.37}$$

U is the flow velocity, C is the speed of sound in the fluid, and k, R, and T are the specific heat ratio, gas constant, and temperature in absolute scale, respectively. For values of $\mathrm{Ma} \leq 0.3$, the incompressibility assumption in the flow analysis is valid.

Vortices

According to the works of Liepmann & Gharib (1992), the presence of streamwise vortices in jet flow improves entrainment and mixing. Similarly, from Reeder & Samimy (1996) and Zaman, Reeder, & Samimy (1994), installing tabs at the nozzle trailing edge can generate streamwise vortices. The influence of a tab

`

generated vortices on entrainment and mixing depends on the orientation, the position, and the number of tabs. Four tabs spaced equally around the lip of the nozzle gave the best result.

Geometry Parameters

This includes the ejector length and the tube ratio to nozzle diameter $\left(\frac{D_m}{D_n}\right)$.

Mixing Length of Ejectors

The mixing length measurement starts from a virtual origin upstream of the nozzle. Below the optimum length, the mixing of the fuel and air is incomplete, and above it, efficiency drops due to frictional losses. Also affecting the system is the axial distance between the nozzle and the throat, known as standoff. A high standoff value will increase the mixing period.

The Ratio of Tube to Nozzle Diameter $\left(\frac{D_m}{D_n}\right)$

Whereas $\boldsymbol{D_n}$ is constant, the value of $\boldsymbol{D_m}$ can be at any point along the length of the ejector. The area of the ejector is not uniform hence $\boldsymbol{D_m}$ is arbitrary but is usually the equivalent of the port diameter.

Performance Parameter

Several indicators measure the performance of an ejector. They include entrainment ratio, ejector efficiency, and momentum mixing (Asim, 2008). The diffuser characteristics such as pressure loss coefficient, relative total pressure drop, pressure rise coefficient, and diffuser efficiency (Sobieski, 2003).

Entrainment ratio

`

Perhaps the most important parameter used in describing the performance of any ejector is the ratio of the mass of entrained fluid to the mass of the primary fluid $\left(\frac{m_s}{m_p}\right)$, which in this case is the ratio of the entrained mass of air to gas fuel

$$\frac{m_s}{m_p} = \frac{\rho_a(Q - q)}{\rho_f(q)} \tag{3.38}$$

Where q can be determined empirically and Q computed using Eqn. (2.29) or Eqn. (2.42)

Pressure parameters

The pressure in the ejector is the static and dynamic pressures. The static pressure Ps is due to the random motion of the flluid at rest.

$$PV = mRT \tag{3.39}$$

$$P_s = \rho RT \tag{3.40}$$

$\mathrm{P_s}, \rho, and\ T$ are the static pressure, density, and temperature of the gas/air mixture in the ejector, respectively.

R is a specific gas constant.

$$R = \frac{R_u}{M_m} \tag{3.41}$$

$M_m\ and\ R_u$ are the molar mass of the gas/air mixture and universal gas constant, respectively

$$M_m = m_{fa} * M_a + m_{ff} * M_f \tag{3.42}$$

`

m_{fa} and m_{ff} are the mass fraction of air and fuel, respectively, while M_a and M_f are the molar mass of air and fuel

$$m_{fa} = \frac{m_a}{m_T} \tag{3.43}$$

$$m_{ff} = \frac{m_f}{m_T} \tag{3.44}$$

Where $m_T = m_a + m_f$

Considering that entrainment is progressive through the length of the ejector, there will be an axial variation of the air/fuel ratio and the molar mass of the mixture.

The dynamic pressure is due to the motion of the gas through the ejector.

$$P_d = \frac{1}{2}\rho u^2 \tag{3.45}$$

ρ is the density of the air/fuel mixture, and u is the average velocity at the crosssection under consideration.

Total pressure (P_T) in the system is the sum of static and dynamic pressures

$$P_T = P_s + P_d \tag{3.46}$$

Pressure losses between two points, say entry and exit, are quantified using pressure loss coefficient δ_p

$$\delta_p = \frac{P_{T2}}{P_{T1}} \tag{3.47}$$

3.3 Combustion Equations

A combustion reaction with the exact oxygen requirement to completely burn the fuel is stoichiometric.

`

The generic

chemical equation that describes the stoichiometric combustion of a hydrocarbon $C_mH_n\mathrm{O_i}$ with oxygen stock from atmospheric air is;

$$k_fC_mH_nO_i + k_aAir \rightarrow aCO_2 + bH_2O + cN_2 \qquad (3.48)$$

$$k_fC_mH_nO_i + k_a\left(O_2 + \frac{79}{21}N_2\right) \rightarrow aCO_2 + bH_2O + cN_2 \qquad (3.49)$$

$k_f, k_a, a, b, and\ c$ are the coefficients. The mass of the reacting species remains the same after the reaction, and the computation of the coefficients is as follows;

$$a = k_fm;\ \ b = k_f\frac{n}{2};\ \ k_a = k_fm + k_f\frac{n}{4} - \frac{k_fi}{2};\ \ c = k_a\left(\frac{79}{21}\right) = \left(k_fm + k_f\frac{n}{4} - \frac{k_fi}{2}\right)\left(\frac{79}{21}\right)$$

For one mole of fuel, k_f is 1, therefore

$$a = m;\ \ b = \frac{n}{2};\ \ k_a = m + \frac{n}{4} - \frac{i}{2};\ \ c = k_a\left(\frac{79}{21}\right) = \left(m + \frac{n}{4} - \frac{i}{2}\right)\left(\frac{79}{21}\right)$$

$$\frac{k_a + k_a\left(\frac{79}{21}\right)}{k_f} \qquad (3.50)$$

The ratio k is the stoichiometric air/fuel ratio, which measures the relative concentration of air and fuel.

The stoichiometric condition is hardly the case in most combustion systems because of the differences in operating conditions. The air supply is often in excess or short of the stoichiometric value. In excess, the mixture is weak or lean but rich when in short supply

The equivalence ratio (∅) is used to indicate the deviation of the mixture concentration from the stoichiometric value and is given by

`

$$\emptyset = \frac{Actual\ F/A}{Stoichiometric\ F/A} \tag{3.51}$$

Or

$$\emptyset = \frac{1}{(A_e + 1)} \tag{3.52}$$

Where A_e is the percentage of excess air

Combustion products will differ depending on the $\emptyset$ value, which indicates the amount of oxygen available to convert carbon from CO to CO_2. In lean mixtures $\emptyset < 1$, the oxygen supply is sufficient to complete the conversion of the carbon to CO_2, and the excess oxygen escapes with other combustion products. The chemical equation for this type of reaction will be of the form

$$k_f C_m H_n O_i + \frac{k_a}{\emptyset}\left(O_2 + \frac{79}{21}N_2\right) \rightarrow aCO_2 + bH_2O + cN_2 + dO_2 \tag{3.53}$$

$k_f, k_a, a, b, and\ c$ are the same as the stoichiometric coefficients $d = \frac{k_a}{\emptyset} - k_a$

$\emptyset$>1 in fuel-rich mixtures, and they form soot. The approximate oxidation sequence is the conversion of the carbon in the hydrocarbon fuel to CO, then the oxidation of hydrogen to H_2O, and CO to CO_2 (Chung L. K., 2006). CO passes off as a by-product in rich mixtures because of insufficient oxygen.

$$k_f C_m H_n O_i + \frac{k_a}{\emptyset}\left(O_2 + \frac{79}{21}N_2\right) \rightarrow aCO_2 + bH_2O + cN_2 + dCO \tag{3.54}$$

where

$k_a = m + \frac{n}{4} - \frac{i}{2}$; $a = \left(\frac{2ka}{\emptyset} + k_f i\right) - \left(\frac{k_f n}{2} + k_f m\right)$; $b = \frac{k_f n}{2}$, $c = \frac{k_a}{\emptyset}\left(\frac{79}{21}\right)$;

$d = \left(2k_f m + \frac{k_f n}{2}\right) - \left(\frac{2ka}{\emptyset} + k_f i\right)$

`

3.3.1 **Dissociation**

Combustion reactions discussed in the previous section are known as the global reaction. It gives a general overview of species transformation during combustion but not in detail. At very high temperatures, combustion products $\mathrm{CO_2}$ and $\mathrm{H_2O}$ break up into components as

$$2CO + O_2 \rightleftharpoons 2CO_2 \tag{3.55}$$

$$2H_2 + O_2 \rightleftharpoons 2H_2O \tag{3.56}$$

This phenomenon is known as dissociation. The reverse reaction i.e., the breakup, is endothermic and absorbs heat from the system. The adiabatic flame temperature computed based on global reaction, which is entirely exothermic, is usually higher than the actual value. The implication is that in combustion systems involving hydrocarbons and air, the combustion product would at least, in addition to CO_2, H_2O,and N_2, contain the dissociated species such as CO, H_2, and O2. Eqn(3.57) is a more elaborate combustion reaction

$$k_f C_m H_n O_i + \frac{k_a}{\emptyset}\left(O_2 + \frac{79}{21}N_2\right) \to aCO_2 + bH_2O + cN_2 + dCO + eH_2 + f\,O_2 \tag{3.57}$$

$a = k_f m - d$

$b = 0.5(\mathrm{k_f}n - 2e)$

$\frac{\mathrm{k_a}}{\emptyset} = 0.5(2a + b + d + 2f - \mathrm{k_f}i)$

$c = \left(\frac{\mathrm{k_a}}{\emptyset}\frac{79}{21}\right)$

$a, b, d, e, and\ f$ are unknowns, with just three equations available. Therefore, two more equations are needed to determine them.

`

Other possible product includes HO, C, $\mathrm{O}, \mathrm{H}, \mathrm{N}, \mathrm{NO}$, NO+, etc. These are the minor species (Chung L. K., 2006) & (Glassman & Yetter, 2008). O_2 is a minor species in rich mixtures, while in lean mixtures (Chung L. K., 2006). Considering all the possible species makes product composition very complex, but narrowing only to the major ones will significantly reduce the complexity and give a reasonably accurate and physically illuminating result.

Each species exerts some pressure in the system and from gas law $(PV = nRT)$. P is proportional to $n -$ the number of moles of the gas species. Therefore, the partial pressure P_i of a species i as a function of the total pressure P and its molar proportion is

$$P_i = \left(\frac{n_i}{\sum_i n_i}\right) P \tag{3.58}$$

$n_i / \sum_i n_i$ is the mole fraction of species i in the mixture.

The proportions of the constituents vary with temperature and pressure and depend on the value of equilibrium constant k whose knowledge is needed to derive the fourth equation that completes the set of simultaneous equations necessary for the computation of the product compositions.

For a hypothetical reaction,

$\mathrm{aA} + \mathrm{bB} \rightleftharpoons \mathrm{cC}$

The equation for a standard thermodynamic equilibrium constant K° is

$$ln\, K^{\circ} = ln\left(\frac{P_c}{P^{\circ}}\right)^{c} - ln\left(\frac{P_b}{P^{\circ}}\right)^{b} - ln\left(\frac{P_a}{P^{\circ}}\right)^{a} \tag{3.59}$$

$K^{\circ}$is dimensionless and standardized by normalizing with P°, which is I bar.

$\mathrm{P_a}, Pb, and\ \mathrm{P_c}$ are the partial pressures of species A,

B, and C, respectively.

`

Comparing this with Eqn. (3.55) and Eqn. (3.56) respectively, the dimensionless standard thermodynamic equilibrium constant K° for both equations can be written as

$$K^{\circ} = \frac{p_{CO_2}(p^{\circ})^{1/2}}{p_{CO}\left(p_{O_2}\right)^{1/2}} \tag{3.60}$$

and

$$K^{\circ} = \frac{p_{H_2O}(p^{\circ})^{1/2}}{p_{H_2}\left(p_{O_2}\right)^{1/2}} \tag{3.61}$$

From the above equations, K° is the ratio of product to reactant. Therefore, when it is high, the proportion of the product is high, and the level of dissociation is low.

The dissociation of $\mathrm{CO_2}$ and $\mathrm{H_2O}$ in the combustion of hydrocarbons is simultaneous, and the division of Eqn. (3.61) by Eqn. (3.60) gives a third equilibrium constant as

$$K^{\circ} = \frac{p_{H_2O}p_{CO}}{p_{H_2}p_{CO_2}} \tag{3.62}$$

Thermodynamic tables such as JANAF tabulate K°values against temperature.

Substituting $\sum_{\mathrm{i}} \mathrm{n_i}$ with n_T it follows from Eqn. (3.58) and Eqn. (3.59) that

$$\mathrm{p_{CO_2}} = \frac{a}{n_T}P, \qquad \mathrm{p_{CO}} = \frac{d}{n_T}P, \qquad \mathrm{p_{O_2}} = \frac{f}{n_T}P$$

Where P is the sum of the partial pressures of the constituents

Substituting these into Eqn. (3.60) gives

$$K^{\circ} = \frac{a}{d}\sqrt{\frac{n_T}{fP}} \tag{3.63}$$

`

Similarly,

$$\mathrm{p_{H_2O}} = \frac{b}{n_T}P \; and \;\; \mathrm{p_{H_2}} = \frac{e}{n_T}P$$

and Eqn. (3.61) and Eqn. (3.62) respectively as

$$K^\circ = \frac{b}{e}\sqrt{\frac{n_T}{fP}} \tag{3.64}$$

$$K^\circ = \frac{bd}{ea} \tag{3.65}$$

P in Eqn. (3.63) is the sum of $\mathrm{p_{CO_2}}, \mathrm{p_{CO}}$ and $\mathrm{p_{O_2}}$ while for Eqn. (3.64) It is the sum of $\mathrm{p_{H_2O}}, \mathrm{p_{H_2}}, and$ $\mathrm{p_{O_2}}$

Any two of the equations (3.63), (3.64), and (3.65) are sufficient to determine the product composition, while the K° value reading is from the thermodynamic tables.

3.3.2 Adiabatic Flame Temperature

The heat release(Q) (Irvin & Richard, 2008) or change in internal energy (ΔU) during a combustion reaction is independent of the process but a function of the product composition, temperature, pressure, and state (Irvin & Richard, 2008).

For a constant volume or non-flow process, the expression for ΔU is

$$\Delta U = Q_v = U_P - U_R \tag{3.66}$$

The heat release at a constant pressure or steady flow process is equivalent to a change in enthalpy ΔH between the reactant and product

$$\Delta H = Q_P = H_P - H_R \tag{3.67}$$

`

The heat released when reactants at a state (1) transform to products at another state (2) during combustion will depend only on the conditions at states 1 and 2 and is independent of the process through which the transformation occurred. This heat release takes place in three stages.

First, the change from reactant at state 1 to reactant at a reference temperature $T_\circ$, followed by the change from reactant at $T_\circ$ to the product at $T_\circ$ and finally from product at $T_\circ$ to product at state 2.

For a constant volume system, the process analysis is

$$U_{P2} - U_{R1} = \left(U_{R\circ} - U_{R1}\right) + \left(U_{P\circ} - U_{R\circ}\right) + \left(U_{P2} - U_{P\circ}\right) \tag{3.68}$$

U_{R1} is the internal energy of the reactant at state 1, U_{P2} is the internal energy of the product at state 2, while $\mathrm{U_{R\circ}}$ and $\mathrm{U_{P\circ}}$, respectively, are the internal energies of the reactants and products at a reference temperature $T_\circ$

$$U_{P\circ} - U_{R\circ} = (\Delta U_\circ)$$

is the internal energy of reaction at reference temperature $T_\circ$

$$U_{R\circ} - U_{R1} = \sum_{R} n_i(\breve{u}_{i\circ} - \breve{u}_{i1})$$

$$U_{P2} - U_{P\circ} = \sum_{P} n_i(\breve{u}_{i2} - \breve{u}_{i\circ})$$

Where the value of u_i is at the average of the temperature range (T) i.e., for the temperature range $T_\circ$ to T_1

$$T = \frac{(T_\circ + T_1)}{2}$$

in terms of specific heats, this is

`

$$U_{R_\circ} - U_{R1} = (T_\circ - T_1) \sum_R m_i c_{vi}$$

$$U_{P2} - U_{P_\circ} = (T_2 - T_\circ) \sum_R m_i c_{vi}$$

Extending the same analysis to constant pressure systems

$$H_{P2} - H_{R1} = \left(H_{R_\circ} - H_{R1}\right) + \left(H_{P_\circ} - H_{R_\circ}\right) + \left(H_{P2} - H_{P_\circ}\right) \tag{3.69}$$

Where

H_{R1} is the enthalpy of a reactant at state 1, H_{P2} is the enthalpy of the product at state 2, while $\mathrm{H}_{\mathrm{R}_\circ}$ and $\mathrm{H}_{\mathrm{P}_\circ}$, respectively, are the enthalpies of the reactants and products at a reference temperature $T_\circ$

$$H_{P_\circ} - H_{R_\circ} = (\Delta H_\circ)$$

is the enthalpy of the reaction at $T_\circ$

$$H_{R_\circ} - H_{R1} = \sum_R n_i\left(\check{h}_{i^\circ} - \check{h}_{i1}\right)$$

$$H_{P2} - H_{P_\circ} = \sum_P n_i\left(\check{h}_{i2} - \check{h}_{i^\circ}\right)$$

or in terms of specific heat

$$H_{R^\circ} - H_{R1} = (T_\circ - T_1) \sum_P m_i c_{pi}$$

$$H_{P2} - H_{P_\circ} = (T_2 - T_\circ) \sum_P m_i c_{pi}$$

$\sum_R and \sum_P respectively$ represents the summation of all constituents of reactants and products.

Also $m_i c_{vi} = n_i \tilde{c}_{vi} \; and \; m_i c_{pi} = n_i \tilde{c}_{pi}$

`

Where n_i the amount of substance of species i, m_i is the mass of species i, $\tilde{c}_{vi}$ is the molar specific heat of species i at constant volume, and $\tilde{c}_{pi}$ is the molar specific heat of species i at constant pressure.

The enthalpy of reaction $\Delta H_\circ$ can be computed from the enthalpy of formation Δh_{f° using Eqn. (3.71).

$$\Delta H_\circ = \sum_P n_i \Delta h_{fi^\circ} - \sum_R n_i \Delta h_{fi^\circ} \qquad (3.70)$$

Δh_{f° is the increase in enthalpy or the amount of heat released or absorbed from the formation of one mole of a substance from its constituent elements in their standard state, with the initial and final temperature $T_\circ$ being the same. The thermodynamic tables contain Δh_{f° values for different substances. At standard state, $T_\circ$ is 25°C, and the pressure is 1 bar. Δh_{f° is zero for elements in their standard form at standard state. It is positive if the process is endothermic and negative for exothermic processes.

Regarding Eqn. (3.67) and Eqn. (3.68), if all the heat raises only the temperature of the product gases, $\Delta U \; or \; Q_v$, as well as $\Delta H \; or \; Q_P$, is zero. The product temperature is the adiabatic flame temperature (Irvin & Richard, 2008). The implication of this is that

$\mathrm{U_{P2}}-\mathrm{U_{R1}} = 0$ as well as $\mathrm{H_{P2}}-\mathrm{H_{R1}}$ and Eqn. (3.69) and Eqn. (3.70) respectively can be rewritten as

$$\left(U_{R_\circ} - U_{R1}\right) + \Delta U_\circ + \left(U_{P2} - U_{P_\circ}\right) = 0 \qquad (3.71)$$

$$\left(H_{R_\circ} - H_{R1}\right) + \Delta H_\circ + \left(H_{P2} - H_{P_\circ}\right) = 0 \qquad (3.72)$$

$\mathrm{U_{R_\circ}}$ is the sum of the values of internal energies of the reactants at $T_\circ = 25$°C or 298k

$\mathrm{U_{p_\circ}}$ is the sum of the product's internal energy at $T_\circ = 25$°C or 298k

$\mathrm{U_{R1}}$ is the internal energy of the reactant at an initial temperature T_1. $\mathrm{U_{P2}}$ is the unknown, and a similar analogy applies to $\mathrm{H_{P2}}$.

`

$T_{P2}-$ the temperature at which the sum of the internal energies or enthalpies of the products corresponds to U_{P2} and H_{P2}, respectively, is the adiabatic flame temperature and is determined iteratively. The adiabatic flame temperature is the maximum temperature attained when the product mixture is at equilibrium. It influences the reactivity of the various chemical species and plays a critical role in pollutant formation.

3.3.3 Reaction Rate

A chemical reaction occurs when reactive molecules or atoms collide with energy exceeding a minimum threshold. This minimum collision energy is known as the activation energy, and the collision frequency is proportional to the concentration of the reactants. At the beginning of any chemical reaction process, the initial concentration of the reacting species is relatively high, and thus, the rate of collision and product formation. As the reaction progresses, the consumption of the reacting species and product formation will proceed more slowly. The reaction rate is a change in the concentration of the reactants with time.

The collision of atoms and molecules is responsible for chemical reactions. The multiple reactant collision will cause several intermediate species to form before the final product formation.

This intermediate reaction is the elementary reaction. An example of this type of reaction is

$$aA + bB \rightarrow cC + dD \qquad (3.73)$$

$a, b, c, and\ d$ are stoichiometric coefficients, the reaction rate R_r, expressed as the change in concentration with time of either of the reactants $(A\ or\ B)$ or products $(C\ or\ D)$, is proportional to the product of the reacting species concentration raised to a power equal to their reaction order. For an

`

elementary reaction, the order equals the stoichiometric coefficient (Irvin & Richard, 2008) and (Ragland & Bryden, 2011) i.e.,

$$R_{rf} = -\frac{d[A]}{dt} = -\frac{d[B]}{dt} = \frac{d[C]}{dt} = \frac{d[D]}{dt} = k_f[A]^a[B]^b \tag{3.74}$$

$[A], [B], [C], and\ [D]$, respectively, are the concentrations of species A, B, C, and D so that

$$[A] = \frac{a}{n}\frac{P}{\hat{R}T}$$

and

$$[B] = \frac{b}{n}\frac{P}{\hat{R}T}$$

Where n is the total number of moles of reactive species in the mixture for the forward reaction of Eqn. (3.74) It is the sum of a and b; P is the system's total pressure, $\hat{R}$ is the universal gas constant, and T is temperature.

k_f is the reaction rate constant, which is an exponential function of the temperature of the Arrhenius form

$$k_f = k_0 e^{-E/\hat{R}T} \tag{3.75}$$

where

k_0 is the pre-exponential or frequency factor, and E is the activation energy. The empirical data for k0 and E are available for most elementary reactions that occur during combustion.

Elementary reactions are reversible reactions. The reverse form of Eqn. (3.74) is

$$cC + dD \rightarrow aA + bB \tag{3.76}$$

`

$$R_{rb} = -\frac{d[C]}{dt} = -\frac{d[D]}{dt} = \frac{d[A]}{dt} = \frac{d[B]}{dt} = k_b[C]^c[D]^d \tag{3.77}$$

At equilibrium,

$$-\frac{d[C]}{dt} = -\frac{d[D]}{dt} = \frac{d[A]}{dt} = \frac{d[B]}{dt} = 0$$

The net reaction rate will be

$$k_f[A]^a[B]^b - k_\mathrm{b}[C]^c[D]^d = 0$$

$$\frac{k_f}{k_b} = \frac{[C]^c[D]^d}{[A]^a[B]^b} \tag{3.78}$$

$\frac{[C]^c[D]^d}{[A]^a[B]^b}$ is thermodynamic equilibrium constant K°.

A simple combustion process comprises at least 20 elementary reactions, and reaction rate analysis on this basis is complex (Irvin & Richard, 2008). Westbrook and Dryer (1981) proposed a one and two-step global mechanism as a simple alternative to this. They varied the reaction rate parameters so that the flame speed computed using the resulting rate expression agreed with the experimental data.

The rate equation for the single-step global reaction of the form

$$fuel + \alpha(O_2 + 3.76N_2) \rightarrow \beta CO_2 + \delta H_2O \ + \alpha 3.76N_2 \tag{3.79}$$

is

$$r_f = -\frac{d[fuel]}{dt} = -AT^zP^me^{-E/\hat{R}T}[fuel]^{n1}[oxidizer]^{n2} \tag{3.80}$$

For many cases, $z = m = 0$ and

$$r_f = \frac{d[fuel]}{dt} = Ae^{-E/\hat{R}T}[fuel]^{n_1}[oxidizer]^{n_2} \tag{3.81}$$

`

$$[fuel] = x_f n$$

Where $n = \frac{p}{RT_{adiabatic}}$ and x_f is the mole of a fraction of fuel in the stoichiometric fuel/air mixture

i.e.

$$x_f = \frac{1}{1 + \alpha * 4.76}$$

Similarly,

$$[\text{oxidizer}] = (\alpha * 4.76)[fuel]$$

In Westbrook and Dryer's approach, The pre-exponential was varied while keeping the rest of the parameters (n_1,n_2, E) constant until the flame speed at the atmospheric pressure and the stoichiometric air-fuel ratio coincided with the empirical value. The resulting model predicted the flame speed as a function of equivalent ratios and pressures. The exponents n_1 and n_2 are the reaction order of the reactants and indicate the extent to which the reaction rate will change when the concentration of the reactants is varied. The evaluation of the overall reaction order is by experiment. For elementary reactions, however, the reaction order and stoichiometric coefficient have the same value (Chung L. K., 2006).

3.3.4 **Flame**

Flames are combustion waves that advance through a flammable fuel oxidizer mixture when ignited. The flame propagation velocity is classified as subsonic when it is lower than the sound velocity in the burnt gases or supersonic when it is higher.

At subsonic velocity, the mixture deflagrates in layers because heat and radicals at the flame front are simultaneously transferred to the layer of the unburnt mixture ahead, causing an increase in the temperature of the layer downstream and subsequent ignition.

`

Detonation happens at supersonic velocity. It is a function of the system's shock wave, which raises the temperature and pressure of the entire mixture substantially to cause an explosive reaction.

In most domestic appliances, fuel and oxidizer mix are in steady laminar flow, and the deflagration or laminar flame velocity ranges between $20 - 40\,cm/s$, depending on the reaction rate (Irvin & Richard, 2008).

Flame structure

The ignition of a charge in steady laminar flow will cause the flame to propagate towards the unburnt mixture. The flame front will stabilize where the flow velocity perpendicular it and the burning velocity are at equilibrium. The flame is static at equilibrium. The lean premixed flame consists of the burning or reaction zone and the preheat zone (Figure 3.4).

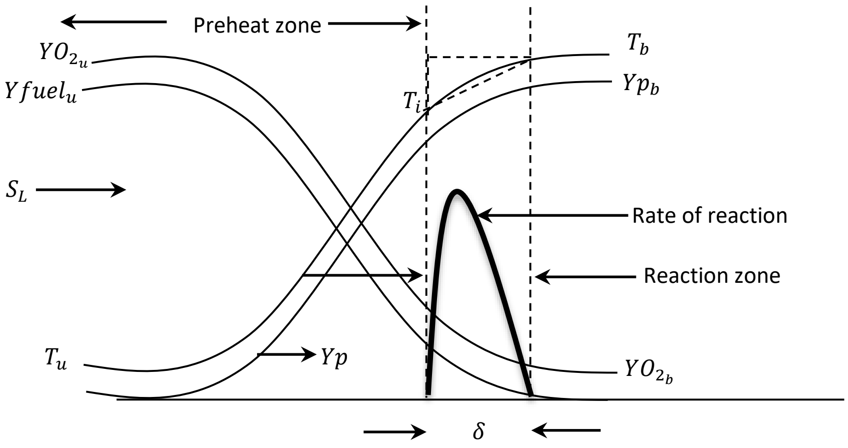

Figure 3.4 Lean premixed flame structure

`

The premixed fuel $\left(Y_{fuel_u}\right)$ and oxidizer $\left(Y_{O_{2u}}\right)$ convected continuously from an upstream location with the velocity S_L known as the burning velocity diffuse into the reaction zone. This zone has a characteristic thickness δ and starts from the point of the fuel ignition to the place of complete fuel consumption. Within this space, the reaction rate (i.e., the rate of product formation or the depletion of the reactants) is rapid, with a corresponding rise in temperature due to heat release. At the end of the reaction zone, the excess oxygen $\left(Y_{O_{2b}}\right)$ and most of the products formed during the reaction (Yp_b) are convected away while the rest diffuse and combine with the unburnt mixture due to concentration gradient. Because of the temperature gradient, heat conduction from the reaction zone to adjacent layers of the unburnt mixture occurs. This simultaneous heat conduction and diffusion of combustion product increase the temperature of the adjacent unburnt mixture. Hence, the region next to the reaction zone is the preheat region.

3.3.5 **Burning Velocity**

The fuel oxidizer mix ignites when the heat transfer from the reacting zone raises the temperature of the unburnt mixture above the ignition temperature T_i.

If the temperature profile in the reacting zone is approximately linear (Figure 3.4), then the slope will be

$$\frac{dT}{dx} = \frac{T_b - T_i}{\delta} \tag{3.82}$$

T_b is the flame temperature, T_i is the ignition temperature, and δ is the thickness of the reacting zone.

The chemical heat (Q_{chem}) released in the reaction zone are

$$Q_{chem} = KA\frac{dT}{dx} \tag{3.83}$$

It then follows from Eqn. (3.82) that

`

$$Q_{chem} = KA\frac{T_b - T_i}{\delta}$$

If the system is adiabatic, the chemical heat liberated only heats the unburnt mixture, and the heat gained by the unburnt mixture will equal the chemical heat release.

$$\dot{m}C_p(T_b - T_u) = KA\frac{T_b - T_i}{\delta} \qquad (3.84)$$

$$\dot{m} = \rho A u$$

Where $u = S_L = burning\ velocity$

$$S_L = \frac{K}{\rho C_p}\left(\frac{T_b - T_i}{T_b - T_u}\right)\frac{1}{\delta} \qquad (3.85)$$

$\frac{K}{\rho C_p} = \lambda =$ thermal diffusivity hence

$$S_L = \frac{\lambda}{\delta}\left(\frac{T_b - T_i}{T_b - T_u}\right) \qquad (3.86)$$

From Eqn. (3.86), δ and T_i are not known.

Since δ is the thickness of the reaction zone, the rate at which the unburnt mixture flows into the reaction zone must be the same as the rate of consumption

$$\rho A S_L = r_f A \delta \qquad (3.87)$$

$$\delta = \frac{\rho S_L}{r_f} \qquad (3.88)$$

Where $\mathrm{r_f}$ is the reaction rate in $gcm^{-3}s^{-1}$

Substituting Eqn. (3.88) into Eqn. (3.86)

`

$$S_L = \left(\frac{\lambda r_f}{\rho}\left(\frac{T_b - T_i}{T_b - T_u}\right)\right)^{0.5} \tag{3.89}$$

It also follows from Eqn. (3.89) that the approximate mass of the fuel and oxidizer mixture consumed by the laminar flame is

$$\rho S_L \sim \left(\frac{k r_f}{C_p}\left(\frac{T_b - T_i}{T_b - T_u}\right)\right)^{0.5} \tag{3.90}$$

To eliminate the unknown T_i from the temperature term $\left(\frac{\mathrm{T_b - T_i}}{\mathrm{T_b - T_u}}\right)$, a procedure known as narrow reaction zone asymptotics that assumes that the reaction rate decreases rapidly with a decrease in temperature was applied (Irvin & Richard, 2008). The result of this was the replacement of the temperature term with

$$\frac{R{T_b}^2}{E(T_b - T_u)}$$

The term $\frac{R{T_b}^2}{E(T_b - T_u)}$ is the Zeldovich number, represented with the symbol β. It specifies the ratio of the preheat to reaction zone thickness.

$$S_L = \left(\frac{\lambda r_f}{\rho\beta}\right)^{0.5} \tag{3.91}$$

From the above analysis, S_L is a function of the thermochemical properties of the fuel oxidizer mix so that a given mixture propagates with a unique S_L.

3.3.6 **Stability Limits**

Laminar flame stability is a function of the heat and flow properties of the mixture. Heat properties (heat loss and release rate) depend on the mixture ratio. Both in the rich and lean concentration spectrum, there are mixture ratios beyond which the heat loss to the surroundings is higher than the heat from the

`

combustion process. In this circumstance, the flame propagation after removing the ignition source is impossible. These are the rich and lean flammability limits (Irvin & Richard, 2008). The latter is responsible for flashback, blow-off, and flame lift.

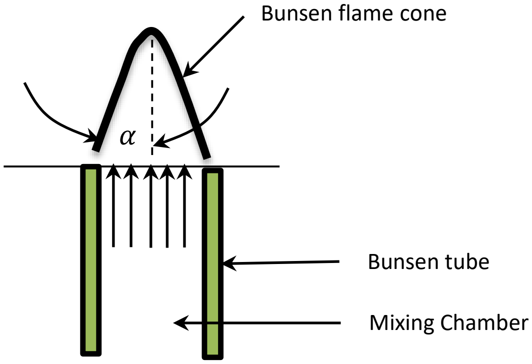

Figure 3.5 Bunsen flame

The flame resulting from the ignition of an unburnt mixture flowing through a tube at a velocity S_L will be stationary inside the tube. Above S_L, the equilibrium point will be outside, often at the tube exit. The flame profile will take the form in Figure 3.5 for a vertical tube, as in Bunsen flame, and can remain at the rim for a considerable range of flow velocity and mixture concentration. Flame stability over a wide range of service conditions is necessary for the continuous operation of any practical combustion system. This process is known as flame stabilization. The terms such as flame holding, flame anchoring, or flame attachment also describe the process in some literature (Chung L. K., 2006). Flame stability allows for balance in the flame structure, location, orientation, and configuration in response to adjustments in mixture concentration and flow velocity (Irvin & Richard, 2008) (Chung L. K., 2006).

`

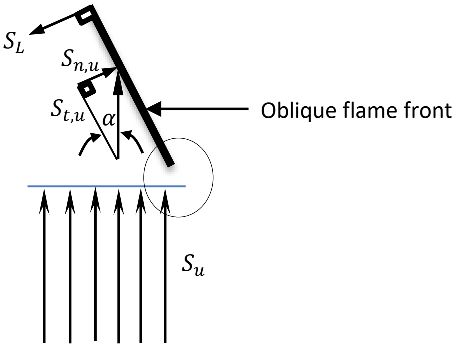

Figure 3.6 Kinematic balance of a steady oblique flame

Figure 3.6. Shows the kinematic flame balance at the tube exit. The flow velocity of the unburnt mixture S_u has a normal and a tangential component $S_{n,u}$, and $S_{t,u}$, respectively. For the flame front to be stationary, S_L must be equal to $S_{n,u}$.

$$S_L = S_{n,u}$$

From Figure 3.6, $S_{n,u} = S_u \sin \alpha$ and

$$S_L = S_u \, sin \, \alpha \tag{3.92}$$

α is the cone angle of the Bunsen flame. Given that S_L is unique for a mixture concentration and the flame front is stable at the rim, if the laminar flow velocity S_u approaching the flame front increases, the flame cone angle must reduce to meet the condition $S_L = S_{n,u}$.

`

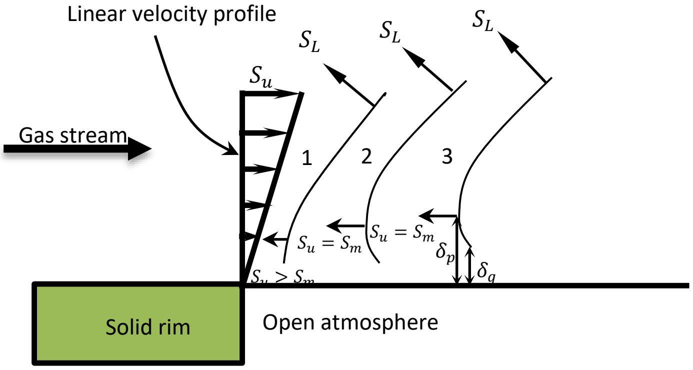

Figure 3.7 Stabilization mechanism of Bunsen flame

The velocity profile of a flow that has developed fully is parabolar. The velocity is significantly lower at the rims than at the center due to the no-slip condition. The velocity change close to the boundary is approximately linear Figure 3.7and unequal to S_L- the characteristic burning velocity of the mixture. Factors affecting the near-wall velocity change include heat loss from the flame to the rim, radical quenching, and dilution of the unburnt mixture concentration due to diffusion and entrainment of the ambient air (Figure 3.7). Very close to the wall, the reaction is unsustainable because of the high rate of heat loss to the wall and quenching. The perpendicular distance from the wall to where the quenching occurs is the quenching distance δ_qFigure 3.7). Considering the variation in flow velocity and modification of S_u at the boundary layer close to the rim, the flame will anchor at the point δ_p known as penetration distance, where the local flow velocity and the modified laminar flame speed S_m are in equilibrium.

In the flame stabilization for a Bunsen flame of Figure 3.7, the effect of the flame-flow interaction was negligible. Heat loss to the rim causes cooling and a reduction in reactivity. The consequence is a drop in the burning velocity of the flame close to the boundary below S_L. For configuration 1, if S_L is higher than S_u, the flame front will propagate towards the tube inlet, the loss of heat at the rim will cause S_L to drop S_m, which is less than S_u, and the flame will be pushed back and steadied at the edge or region

`

downstream of the rim. Further reduction in S_u for a given mixture ratio and flow velocity or an increase in reactivity by adjusting the mixture concentration towards stoichiometry will cause the flame to propagate toward the tube. Beyond the flashback limit, the burning velocity will be greater than the flow velocity of the gas, and the flame front will propagate into the mixing tube.

If the flow velocity S_u increases, the flame pushes away from the rim as in configuration 2, the heat loss to the edges reduces, S_m increases, and the flame front settles back to a new equilibrium position. In configuration 3, there was an increase in the flow velocity and the advancement of flame away from the rim. This reduces the heat loss to the edges and increases the secondary air diffusion into the unburnt mixture, diluting it. The dilution brings the air-fuel mixture in the rich spectrum closer to stoichiometry, causing a more intense reaction. For a lean charge, the mixture dilution neutralizes the reduction in heat loss.

When the S_u is below the blow-off limit, the flame moves forward and settles at a new equilibrium position, usually in space above the rim, a phenomenon known as flame lift. Beyond the blow-off limit, the reduction in reactivity due to dilution overbalances the increase due to low heat loss. The burning velocity along every streamline is lower than the gas flow velocity, and the flame blows off.

3.3.7 **Flashback**

To further explain the concept of flashback, the velocity profile at different flow conditions and the variation in burning velocity relative to the wall of the burner is compared in Figure 3.8. The burning velocity is zero from the wall up to the quenching distance δ_q from where it begins to increase gradually to a constant value corresponding to S_L the characteristic burning velocity of the flame. The distance from the wall where the flow velocity equates the burning velocity is the penetration distance δ_p. At condition 2 the flow velocity is tangent to S_L and a stable point is reached. Below this point (condition 1) the flow

`

velocity is lower than the burning velocity and the flame will propagate into the tube representing the condition for flashback. The opposite is the case at condition 3 where the flow velocity inside the tube is greater than the flame velocity at any point. The consequence is that any flame inside the tube will be blown out

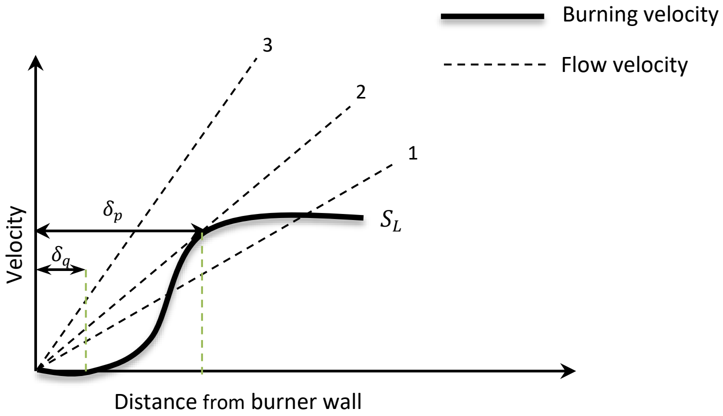

Figure 3.8 Flame flashback condition

From Figure 3.8, the critical velocity gradient for flashback g_c is given as

$$g_c = \frac{u_{/y=\delta_p}}{\delta_p} \tag{3.93}$$

At critical condition,

$u_{/y=\delta_p} \approx S_L$

Therefore

`

$$g_c = \frac{S_L}{\delta_p} \tag{3.94}$$

Where by one dimensional steady analytical development, δ_p can be approximated to flame thickness δ (Kalantari, 2018) and (Irvin & Richard, 2008)

Flame thickness was estimated using the expression (Baumgartner, 2014)

$$\delta = k\frac{\lambda}{S_L} \tag{3.95}$$

Where k is an arbitrary constant which can be taken as unity and therefore follows that

$$\delta = \delta_p \approx \frac{\lambda}{S_L} \tag{3.96}$$

Blowoff

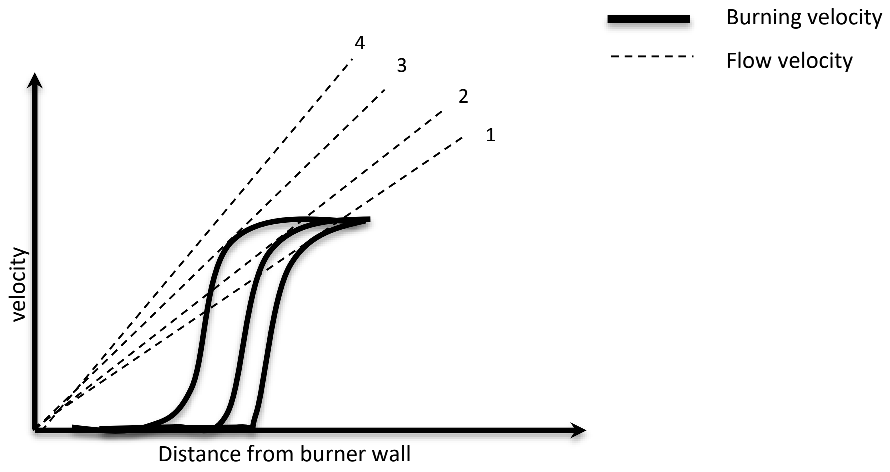

Figure 3.9 Blowoff condition

Figure 3.9 illustrates the blowoff condition for a lean mixture situation. When the flow velocity is sufficiently high the flame is stabilized in space above the rim. Additional increase in flow velocity lifts the flame higher. As the flame moves higher above the rim heat loss is reduced and the burning velocity at the base of the flame increases so that new equilibrium points are reached as illustrated in conditions 1-3. Also the higher the flame is above the rim the more the atmospheric air is entrained diluting the mixture thus setting a limit to the flame speed. Increasing the flow velocity above this limit as represented by condition 4 causes a dynamic imbalance between the flow and burning velocity and the flame will be blown off.

`

3.4 Development of Governing Equations for CFD Computations

Computational fluid dynamics involves the solution to the governing equations of fluid flow which are the continuity, momentum, and energy equations. The equations are the mathematical statements of the three fundamental physical principles- the conservation of mass, momentum and energy. Their development is as follows.

3.4.1 Continuity Equation

The continuity equation is a statement of mass conservation, which states that for an infinitesimally small fluid volume (Figure 3.10), the mass of fluid accumulated equals the difference between the mass flowing in and out of the element.

$$\dot{m}_{in} - \dot{m}_{out} = \frac{dm}{dt} \tag{3.97}$$

$\frac{d\dot{m}}{dt}$ is the rate of change in the accumulated fluid mass with time.

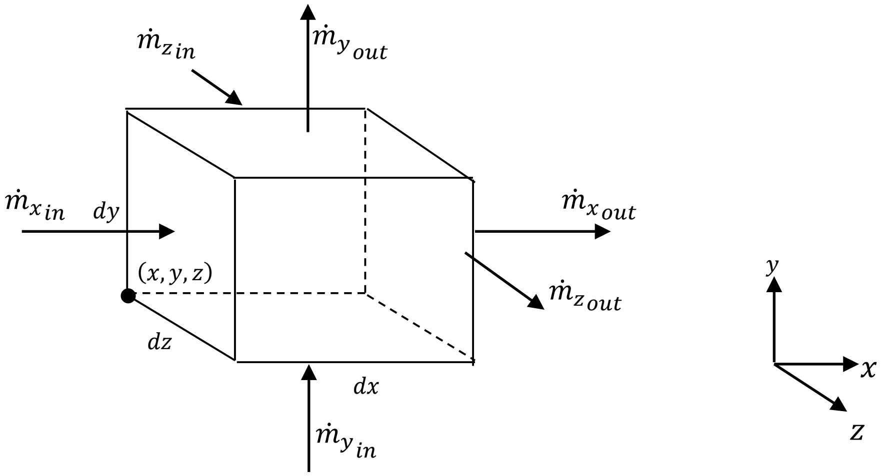

Figure 3.10 mass flux through an infinitesimally small fluid element

`

Concerning Figure 3.10, it follows that

$$\dot{m}_{x_{in}} = \rho_x u_x dydz \tag{3.98}$$

$$\dot{m}_{y_{in}} = \rho_y u_y dxdz \tag{3.99}$$

$$\dot{m}_{z_{in}} = \rho_z u_z dydx \tag{3.100}$$

$$\dot{m}_{x_{out}} = \rho_{x+dx} u_{x+dx} dydz \tag{3.101}$$

$$\dot{m}_{y_{out}} = \rho_{y+dy} u_{y+dy} dxdz \tag{3.102}$$

$$\dot{m}_{z_{out}} = \rho_{z+dz} u_{z+dz} dydx \tag{3.103}$$

Substituting these into the left-hand side of Eqn. (3.97) and dividing through by $dxdydz$ gives;

$$\frac{\rho_x u_x dydz - \rho_{x+dx} u_{x+dx} dydz + \rho_y u_y dxdz - \rho_{y+dy} u_{y+dy} dxdz + \rho_z u_z dydx - \rho_{z+dz} u_{z+dz} dydx}{dxdydz}$$

$m = \rho d\mathrm{v}$

$$\frac{dm}{dt} = \frac{d\rho}{dt} dxdydz \tag{3.104}$$

Substituting **Eqn. (3.104)** and dividing by $dxdydz$, the right-hand side of the equation becomes;

$$\frac{d\rho}{dt} \frac{dxdydz}{dxdydz}$$

Therefore Eqn. (3.97) is now

$$\frac{\rho_x u_x - \rho_{x+dx} u_{x+dx}}{dx} + \frac{\rho_y u_y - \rho_{y+dy} u_{y+dy}}{dy} + \frac{\rho_z u_z - \rho_{z+dz} u_{z+dz}}{dz} = \frac{d\rho}{dt} \tag{3.105}$$

If $\mathrm{u_x} = u$, $\mathrm{u_y} = v, and$ $\mathrm{u_z} = w$, the limits of Eqn. (3.105) as $dx, dy, and\ dz$ approach zero gives

`

$$-\frac{\partial \rho u}{\partial x}-\frac{\partial \rho v}{\partial y}-\frac{\partial \rho w}{\partial z}=\frac{\partial \rho}{\partial t} \tag{3.106}$$

Eqn. (3.106), can be written as

$$\frac{\partial \rho}{\partial t}+div(\rho V)=0 \tag{3.107}$$

The first term of Eqn. (3.107) is a local time derivative and represents the rate of density change with time. The second term is the convective term and represent the net flow of mass across its boundaries

If the flow is steady so that ρ does not change with time, $\frac{\partial \rho}{\partial t}=0$, and

$$div(\rho V)=0 \tag{3.108}$$

For an incompressible flow, ρ is constant at every point in the system, i.e., ρ is independent of $x, y, or\ z$ and Eqn. (3.108) becomes;

$$\frac{\partial u}{\partial x}+\frac{\partial v}{\partial y}+\frac{\partial w}{\partial z}=0 \tag{3.109}$$

For two-dimensional flow

$$\frac{\partial u}{\partial x}+\frac{\partial v}{\partial y}=0 \tag{3.110}$$

3.4.2 **Momentum Equation**

The momentum equation for a viscous flow is a complicated vectorial expression known as the Navier-Stokes equation. The concept of the material derivative is fundamental in momentum equation development.

Material Derivative

A Fluid flowing through a channel (Figure 3.11) consists of several elements or particles. The velocity of one of such particles at points $a, b, and\ c$ will vary due to differences in the cross-sectional area of the channel. Also, the velocity at any point will vary slightly with time around a mean value.

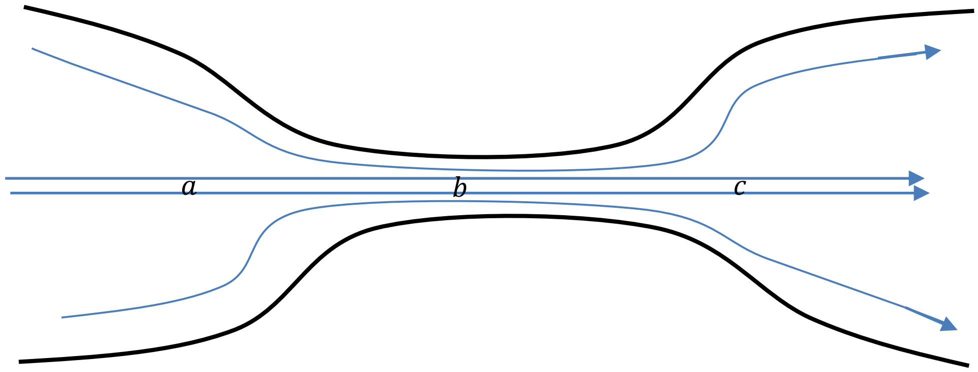

Figure 3.11 Flow through a constricted channel

It then follows that change in the velocity of the fluid element depends both on time and the location and a function of the location (x, y, z) and time(t).

$$u = f(t, x, y, z) \tag{3.111}$$

By applying the chain rule, the change in velocity of the element is

$$du = \frac{\partial u}{\partial t}\partial t + \frac{\partial u}{\partial x}\partial x + \frac{\partial u}{\partial y}\partial y + \frac{\partial u}{\partial z}\partial z \tag{3.112}$$

$$\frac{du}{dt} = \frac{\partial u}{\partial t}\frac{\partial t}{\partial t} + \frac{\partial u}{\partial x}\frac{\partial x}{\partial t} + \frac{\partial u}{\partial y}\frac{\partial y}{\partial t} + \frac{\partial u}{\partial z}\frac{\partial z}{\partial t} \tag{3.113}$$

If $\frac{\partial x}{\partial t} = u; \frac{\partial y}{\partial t} = v\ and\ \frac{\partial z}{\partial t} = w$

Eqn. (3.113) can be written as

`

$$\frac{du}{dt}=\frac{\partial u}{\partial t}+\frac{\partial u}{\partial x}u+\frac{\partial u}{\partial y}v+\frac{\partial u}{\partial z}w \tag{3.114}$$

$$\frac{Du}{Dt}=\frac{\partial u}{\partial t}+u\frac{\partial u}{\partial x}+v\frac{\partial u}{\partial y}+w\frac{\partial u}{\partial z} \tag{3.115}$$

or

$$\frac{Du}{Dt}=\frac{\partial u}{\partial t}+V.gradu \tag{3.116}$$

Eqn. (3.116) is known as material derivative and corresponds to the derivative of the velocity as measured by an observer in the velocity field, and a more general representation is

$$\frac{D}{Dt}=\frac{\partial}{\partial t}+u\frac{\partial}{\partial x}+v\frac{\partial}{\partial y}+w\frac{\partial}{\partial z} \tag{3.117}$$

This result can extend to an arbitrary property $\emptyset$ of the fluid element like temperature, density, and energy

$$\frac{D\emptyset}{Dt}=\frac{\partial\emptyset}{\partial t}+u\frac{\partial\emptyset}{\partial x}+v\frac{\partial\emptyset}{\partial y}+w\frac{\partial\emptyset}{\partial z} \tag{3.118}$$

The expansion of Eqn. (3.107) will give

$$\frac{\partial\rho}{\partial t}+\frac{\partial\rho u}{\partial x}+\frac{\partial\rho v}{\partial y}+\frac{\partial\rho w}{\partial z}=\left\{\frac{\partial\rho}{\partial t}+u\frac{\partial\rho}{\partial x}+v\frac{\partial\rho}{\partial y}+w\frac{\partial\rho}{\partial z}\right\}+\left\{\rho\frac{\partial u}{\partial x}+\rho\frac{\partial v}{\partial y}+\rho\frac{\partial w}{\partial z}\right\}=0 \tag{3.119}$$

The first expression on the right side of Eqn. (3.119) is the material derivative of density. The continuity equation is

$$\frac{D\rho}{Dt}+div(\rho V)=0 \tag{3.120}$$

Momentum equation

The momentum equation is a statement of Newton's second law

$$f = ma \tag{3.121}$$

Which states that the rate of change of momentum equals the sum of the forces acting on the fluid particles. These forces are the body forces (such as centrifugal force and electromagnetic force) and surface forces (such as shear stresses(τ), pressure forces(p), and gravity force).

On a per-unit volume basis,

$$f = \rho \frac{Du}{Dt} \tag{3.122}$$

Where Du/Dt is the material acceleration of the fluid element.

It follows from Eqn. (3.118) that

$$\frac{Du}{Dt} = \frac{\partial u}{\partial t} + \mathrm{u}\frac{\partial \mathrm{u}}{\partial \mathrm{x}} + \mathrm{v}\frac{\partial \mathrm{u}}{\partial \mathrm{y}} + \mathrm{w}\frac{\partial \mathrm{u}}{\partial \mathrm{z}}$$

Therefore,

$$\rho \frac{Du}{Dt} = \frac{\partial \rho u}{\partial t} + \frac{\partial \rho uu}{\partial x} + \frac{\partial \rho vu}{\partial y} + \frac{\partial \rho wu}{\partial z} \tag{3.123}$$

$$\rho \frac{Du}{Dt} = \quad \frac{\partial (\rho u)}{\partial t} + div(\rho V u) \tag{3.124}$$

For a viscous fluid, the surface forces f acting on an infinitesimal fluid particle in the x direction comprise the shear stress and pressure forces as in Figure 3.12

`

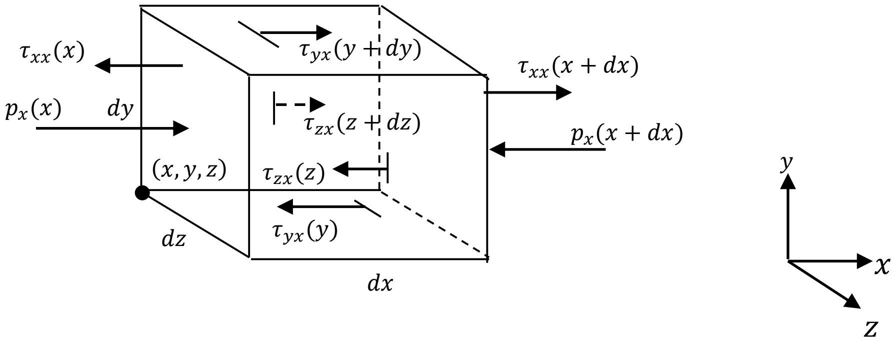

Figure 3.12 Surface forces acting on a fluid particle in the x direction

If the sign convention is such that forces that align with the x-axis are positive and those opposite negative, the net surface and the body forces in the x-direction can summed as

$$\begin{aligned}&(p_x(x) - p_x(x+dx))dydz + (\tau_{xx}(x+dx) - \tau_{xx}(x))dydz + \left(\tau_{yx}(y+dy) - \tau_{yx}(y)\right)dzdx \\ &\quad + \left(\tau_{zx}(x+dx) - \tau_{zx}(x)\right)dydx \\ &\quad + \rho g_x dxdydz \qquad (3.125)\end{aligned}$$

Dividing $Eqn.(3.125)$ by $dxdydz$ gives

$$\begin{aligned}f &= \frac{(p_x(x) - p_x(x+dx))}{dx} + \frac{(\tau_{xx}(x+dx) - \tau_{xx}(x))}{dx} + \frac{\left(\tau_{yx}(y+dy) - \tau_{yx}(y)\right)}{dy} \\ &\quad + \frac{\left(\tau_{zx}(x+dx) - \tau_{zx}(x)\right)}{dz} \\ &\quad + \rho g_x \qquad (3.126)\end{aligned}$$

Taking the limits as $dx, dy\ and\ dz$ approaches zero

$$f = -\frac{\partial p}{\partial x} + \frac{\partial \tau_{xx}}{\partial x} + \frac{\partial \tau_{yx}}{\partial y} + \frac{\partial \tau_{zx}}{\partial z} + \rho g_x \qquad (3.127)$$

`

$Eqn. (2.127)$

Can now be equated to

$$-\frac{\partial p}{\partial x}+\frac{\partial \tau_{xx}}{\partial x}+\frac{\partial \tau_{yx}}{\partial y}+\frac{\partial \tau_{zx}}{\partial z}+\rho g_x = \rho \frac{Du}{Dt} \tag{3.128}$$

$$-\frac{\partial p}{\partial x}+\frac{\partial \tau_{xx}}{\partial x}+\frac{\partial \tau_{yx}}{\partial y}+\frac{\partial \tau_{zx}}{\partial z}+\rho g_x = \frac{\partial (\rho u)}{\partial t}+div(\rho V u) \tag{3.129}$$

The forces acting in the y and z direction, respectively, are

$$-\frac{\partial p}{\partial y}+\frac{\partial \tau_{yy}}{\partial y}+\frac{\partial \tau_{xy}}{\partial x}+\frac{\partial \tau_{zy}}{\partial z}+\rho g_y = \frac{\partial (\rho v)}{\partial t}+div(\rho V v) \tag{3.130}$$

$$-\frac{\partial p}{\partial z}+\frac{\partial \tau_{zz}}{\partial z}+\frac{\partial \tau_{yz}}{\partial y}+\frac{\partial \tau_{xz}}{\partial x}+\rho g_z = \frac{\partial (\rho w)}{\partial t}+div(\rho V w) \tag{3.131}$$

For an incompressible Newtonian fluid, the viscous stresses are proportional to the deformation rate, and nine components of the viscous stress tensors are (Cengel & Cimbal, 2006).

$$\tau_{xx} = \lambda \nabla . V + 2\mu \frac{\partial u}{\partial x} \tag{3.132}$$

$$\tau_{yy} = \lambda \nabla . V + 2\mu \frac{\partial v}{\partial y} \tag{3.133}$$

$$\tau_{zz} = \lambda \nabla . V + 2\mu \frac{\partial w}{\partial z} \tag{3.134}$$

$$\tau_{xy} = \tau_{yx} = \mu \left(\frac{\partial v}{\partial x}+\frac{\partial u}{\partial y}\right) \tag{3.135}$$

$$\tau_{xz} = \tau_{zx} = \mu \left(\frac{\partial w}{\partial x}+\frac{\partial u}{\partial z}\right) \tag{3.136}$$

`

$$\tau_{zy} = \tau_{yz} = \mu\left(\frac{\partial w}{\partial y} + \frac{\partial v}{\partial z}\right) \tag{3.137}$$

The constant of proportionality μ is the dynamic viscosity and relates the stresses to linear deformation. λ relates stresses to volumetric deformation. In practice, the effect of λ is negligible. $\lambda = -\frac{2}{3}\mu$ for gasses (Bengt, et al., 2012).

Eqn. (3.132)-Eqn. (3.137) can be substituted into Eqn. (3.129)

$$f = -\frac{\partial p}{\partial x} + \frac{\partial}{\partial x}\left[\lambda\nabla . V + 2\mu\frac{\partial u}{\partial x}\right] + \frac{\partial}{\partial y}\left[\mu\left(\frac{\partial v}{\partial x} + \frac{\partial u}{\partial y}\right)\right] + \frac{\partial}{\partial z}\left[\mu\left(\frac{\partial w}{\partial x} + \frac{\partial u}{\partial z}\right)\right] + \rho g_x \tag{3.138}$$

The right-hand side of Eqn. (3.139) can be rearranged as

$$-\frac{\partial p}{\partial x} + \mu\left[\frac{\partial}{\partial x}\left(\frac{\partial u}{\partial x} + \frac{\partial v}{\partial y} + \frac{\partial w}{\partial z}\right) + \frac{\partial^2 u}{\partial x^2} + \frac{\partial^2 u}{\partial y^2} + \frac{\partial^2 u}{\partial z^2}\right] + \frac{\partial}{\partial x}(\lambda\nabla . V) + \rho g_x \tag{3.139}$$

The terms $\left(\frac{\partial \mathrm{u}}{\partial \mathrm{x}} + \frac{\partial \mathrm{v}}{\partial \mathrm{y}} + \frac{\partial \mathrm{w}}{\partial \mathrm{z}}\right)$ in the bracket are zero, going by the continuity equation for incompressible flow, and if the term $\lambda\nabla . V$ is negligible

$$-\frac{\partial p}{\partial x} + \mu\left(\frac{\partial^2 u}{\partial x^2} + \frac{\partial^2 u}{\partial y^2} + \frac{\partial^2 u}{\partial z^2}\right) + \rho g_x \tag{3.140}$$

Or

$$-\frac{\partial p}{\partial x} + div(\mu grad u) + \rho g_x$$

The x component of the momentum equation becomes

$$-\frac{\partial p}{\partial x} + \mu\left(\frac{\partial^2 u}{\partial x^2} + \frac{\partial^2 u}{\partial y^2} + \frac{\partial^2 u}{\partial z^2}\right) + \rho g_x = \frac{\partial(\rho u)}{\partial t} + div(\rho V u) \tag{3.141}$$

y and z components, respectively, are

$$\frac{\partial p}{\partial y}+\mu\left(\frac{\partial^2 v}{\partial x^2}+\frac{\partial^2 v}{\partial y^2}+\frac{\partial^2 v}{\partial z^2}\right)+\rho g_y = \frac{\partial(\rho v)}{\partial t}+div(\rho V v) \qquad (3.142)$$

$$-\frac{\partial p}{\partial z}+\mu\left(\frac{\partial^2 w}{\partial x^2}+\frac{\partial^2 w}{\partial y^2}+\frac{\partial^2 w}{\partial z^2}\right)+\rho g_z = \frac{\partial(\rho w)}{\partial t}+div(\rho V w) \qquad (3.143)$$

Eqn. (3.141) to Eqn. (3.143) are the unsteady, nonlinear, second-order partial differential equation known, respectively, as x, y, and z components of incompressible Navier Stokes equation. Navier Stokes equation have three equations with four unknowns- the pressure and three velocity components. The pressure and velocity field computation is by coupling the incompressible continuity equation to the Navier-Stokes equation when the geometry and boundary conditions are defined.

For inviscid or non-viscous fluid, the shear stresses are negligible. Only pressure and gravity forces act on the system, and the momentum equation per unit volume of flow becomes

$$-\frac{\partial p}{\partial x}+\rho g_x = \frac{\partial(\rho u)}{\partial t}+div(\rho V u) \qquad (3.144)$$

$$-\frac{\partial p}{\partial y}+\rho g_y = \frac{\partial(\rho v)}{\partial t}+div(\rho V v) \qquad (3.145)$$

$$-\frac{\partial p}{\partial z}+\rho g_z = \frac{\partial(\rho w)}{\partial t}+div(\rho V w) \qquad (3.146)$$

3.4.3 Energy Equation

The derivation of the energy equation is on the premise that the rate of change of the energy in a fluid particle is equal to the sum of the net heat flux to the particle and the net work done on the particle by surface and body forces. This is a statement of the first law of thermodynamics. Heat and work input defines the energy of the elements.

`

Work done

Work is done on the fluid particle as body and surface forces act on it. The work done by body force on a particle moving with a velocity V equals the product of force and the velocity component in the force direction.

$\rho g.Vdxdydz$

The net surface forces acting on the particle in the x direction $-\frac{\partial \mathrm{p}}{\partial \mathrm{x}}+\frac{\partial \tau_{\mathrm{xx}}}{\partial \mathrm{x}}+\frac{\partial \tau_{\mathrm{yx}}}{\partial \mathrm{y}}+\frac{\partial \tau_{\mathrm{zx}}}{\partial \mathrm{z}}$ in $Eqn.$ (3.128). Therefore, the work done by the force acting in the x direction going by the above definition will be

$$-\frac{\partial up}{\partial x}+\frac{\partial u\tau_{xx}}{\partial x}+\frac{\partial u\tau_{yx}}{\partial y}+\frac{\partial u\tau_{zx}}{\partial z} \qquad (3.147)$$

Similarly, for surface forces acting in the y and z directions, respectively, the work done will be

$$-\frac{\partial vp}{\partial y}+\frac{\partial v\tau_{yy}}{\partial y}+\frac{\partial v\tau_{xy}}{\partial x}+\frac{\partial v\tau_{zy}}{\partial z} \qquad (3.148)$$

$$-\frac{\partial wp}{\partial z}+\frac{\partial w\tau_{zz}}{\partial z}+\frac{\partial w\tau_{yz}}{\partial y}+\frac{\partial w\tau_{xz}}{\partial x} \qquad (3.149)$$

The net rate of work done on the element will be the summation of the surface work in the $x, y, and\ z$ directions and the body force.

$$-\left(\frac{\partial up}{\partial x}+\frac{\partial vp}{\partial y}+\frac{\partial wp}{\partial z}\right) + \left(\frac{\partial u\tau_{xx}}{\partial x}+\frac{\partial u\tau_{yx}}{\partial y}+\frac{\partial u\tau_{zx}}{\partial z}+\frac{\partial v\tau_{xy}}{\partial x}+\frac{\partial v\tau_{yy}}{\partial y}+\frac{\partial v\tau_{zy}}{\partial z}+\frac{\partial w\tau_{xz}}{\partial x}+\frac{\partial w\tau_{yz}}{\partial y} + \frac{\partial w\tau_{zz}}{\partial z}\right)dxdydz + \rho g.Vdxdydz \qquad (3.150)$$

`

Heat input

The net heat flux into the system is due to volumetric heating and heat transfer across the boundary due to temperature gradient.

$$Volumetric\ heating\ of\ the\ particle = \rho\dot{q}dxdydz \tag{3.151}$$

While heat transfer to the particle due to temperature gradient is

$$-\frac{\partial q_x}{\partial x} - \frac{\partial q_y}{\partial y} - \frac{\partial q_z}{\partial z} \tag{3.152}$$

$q_x = -k\frac{\partial T}{\partial x},\ q_y = -k\frac{\partial T}{\partial y}\ , q_z = -k\frac{\partial T}{\partial z}$

Substituting for $q_x,\ q_y, and\ q_z$ in Eqn. (3.153) gives;

$$\frac{\partial}{\partial x}\left(k\frac{\partial T}{\partial x}\right) + \frac{\partial}{\partial y}\left(k\frac{\partial T}{\partial y}\right) + \frac{\partial}{\partial z}\left(k\frac{\partial T}{\partial z}\right) \tag{3.153}$$

The net heat flux into the particle will be the sum of Eqn. (3.151) and Eqn. (3.153)

$$Net\ flux\ \ of\ heat = \left[\rho\dot{q} + \frac{\partial}{\partial x}\left(k\frac{\partial T}{\partial x}\right) + \frac{\partial}{\partial y}\left(k\frac{\partial T}{\partial y}\right) + \frac{\partial}{\partial z}\left(k\frac{\partial T}{\partial z}\right)\right]dxdydz \tag{3.154}$$

The Energy of the Fluid Particle

The total energy of the fluid particle is the sum of internal energy i and kinetic energy, $\frac{1}{2}(u^2 + v^2 + w^2)$.

Therefore, the time rate of change of total energy per unit mass is

`

$$\rho \frac{D}{Dt}\left(i + \frac{1}{2}(u^2 + v^2 + w^2)\right) dxdydz \qquad (3.155)$$

i.e.

$$\rho \frac{D}{Dt}\left(i + \frac{1}{2}(u^2 + v^2 + w^2)\right) dxdydz = \ Net\ rate\ of\ work\ input +\ Net\ heat\ flux \quad (3.156)$$

$$\begin{aligned}
\rho \frac{D}{Dt}\left(i + \frac{1}{2}(u^2 + v^2 + w^2)\right) \\
&= -\left(\frac{\partial up}{\partial x} + \frac{\partial vp}{\partial y} + \frac{\partial wp}{\partial z}\right) \\
&+ \left(\frac{\partial u\tau_{xx}}{\partial x} + \frac{\partial u\tau_{yx}}{\partial y} + \frac{\partial u\tau_{zx}}{\partial z} + \frac{\partial v\tau_{xy}}{\partial x} + \frac{\partial v\tau_{yy}}{\partial y} + \frac{\partial v\tau_{zy}}{\partial z} + \frac{\partial w\tau_{xz}}{\partial x} + \frac{\partial w\tau_{yz}}{\partial y}\right. \\
&\left. + \frac{\partial w\tau_{zz}}{\partial z}\right) dxdydz + \ \ \rho g.V \\
&+ \left[\rho\dot{q} + \frac{\partial}{\partial x}\left(k\frac{\partial T}{\partial x}\right) + \frac{\partial}{\partial y}\left(k\frac{\partial T}{\partial y}\right) + \frac{\partial}{\partial z}\left(k\frac{\partial T}{\partial z}\right)\right] \qquad (3.157)
\end{aligned}$$

The terms in the first and second parenthesis on the right side of Eqn. (3.157) can be further broken down as

$$,\frac{\partial up}{\partial x} = p\frac{\partial u}{\partial x} + u\frac{\partial p}{\partial x}$$

$$\frac{\partial u\tau_{xx}}{\partial x} = u\frac{\partial \tau_{xx}}{\partial x} + \tau_{xx}\frac{\partial u}{\partial x}$$

In terms of internal energy, the energy equation is;

`

$$\rho\frac{D(i)}{Dt} = -\rho\frac{D\left(\frac{1}{2}(u^2+v^2+w^2)\right)}{Dt} \tag{3.158}$$

From Eqn. (3.128)

$\rho\frac{Du}{Dt} = -\frac{\partial p}{\partial x} + \frac{\partial \tau_{xx}}{\partial x} + \frac{\partial \tau_{yx}}{\partial y} + \frac{\partial \tau_{zx}}{\partial z} + \rho g_x$

It therefore follows that

$$\rho\frac{D}{Dt}(u^2/2) = -u\frac{\partial p}{\partial x} + u\frac{\partial \tau_{xx}}{\partial x} + u\frac{\partial \tau_{yx}}{\partial y} + u\frac{\partial \tau_{zx}}{\partial z} + \rho g_x u \tag{3.159}$$

$$\rho\frac{D}{Dt}(v^2/2) = -v\frac{\partial p}{\partial x} + v\frac{\partial \tau_{xx}}{\partial x} + v\frac{\partial \tau_{yx}}{\partial y} + v\frac{\partial \tau_{zx}}{\partial z} + \rho g_y v \tag{3.160}$$

$$\rho\frac{D}{Dt}(w^2/2) = -w\frac{\partial p}{\partial x} + w\frac{\partial \tau_{xx}}{\partial x} + w\frac{\partial \tau_{yx}}{\partial y} + w\frac{\partial \tau_{zx}}{\partial z} + \rho g_z w \tag{3.161}$$

Summing Eqn. (3.159-3.161) gives

$$\begin{aligned}\rho\frac{D\frac{1}{2}(u^2+v^2+w^2)}{Dt} \\ &= -\left(u\frac{\partial p}{\partial x} + v\frac{\partial p}{\partial y} + w\frac{\partial p}{\partial z}\right) + u\left(\frac{\partial \tau_{xx}}{\partial x} + \frac{\partial \tau_{yx}}{\partial y} + \frac{\partial \tau_{zx}}{\partial z}\right) \\ &+ v\left(\frac{\partial \tau_{yy}}{\partial y} + \frac{\partial \tau_{xy}}{\partial x} + \frac{\partial \tau_{zy}}{\partial z}\right) + w\left(\frac{\partial \tau_{zz}}{\partial z} + \frac{\partial \tau_{yz}}{\partial y} + \frac{\partial \tau_{xz}}{\partial x}\right) \\ &+ \quad \rho\big(g_x u + g_y v \\ &+ g_z w\big)\end{aligned} \tag{3.162}$$

`

$\rho(g_x u + g_y v + g_z w) = \rho g.V$

Substituting Eqn. (3.162) into Eqn. (3.156)

$$\rho\frac{D(i)}{Dt} = -\left(p\frac{\partial u}{\partial x} + p\frac{\partial v}{\partial y} + p\frac{\partial w}{\partial z}\right) + \left(\tau_{xx}\frac{\partial u}{\partial x} + \tau_{yx}\frac{\partial u}{\partial y} + \tau_{zx}\frac{\partial u}{\partial z}\right)$$

$$+ \left(\tau_{yy}\frac{\partial v}{\partial y} + \tau_{xy}\frac{\partial v}{\partial x} + \tau_{zy}\frac{\partial v}{\partial z}\right) + \left(\tau_{zz}\frac{\partial w}{\partial z} + \tau_{yz}\frac{\partial w}{\partial y} + \tau_{xz}\frac{\partial w}{\partial x}\right)$$

$$+ \left[\rho\dot{q} + \frac{\partial}{\partial x}\left(k\frac{\partial T}{\partial x}\right) + \frac{\partial}{\partial y}\left(k\frac{\partial T}{\partial y}\right)\right.$$

$$\left. + \frac{\partial}{\partial z}\left(k\frac{\partial T}{\partial z}\right)\right] \qquad (3.163)$$

From $Eqn.$ (3.134) -$Eqn.$ (3.136),$\tau_{yx} = \tau_{xy}$ $\tau_{zx} = \tau_{xz}$ and $\tau_{zy} = \tau_{yz}$

Therefore

The rearrangement of Eqn. (3.163) will give;

$$\rho\frac{D(i)}{Dt} = -\left(p\frac{\partial u}{\partial x} + p\frac{\partial v}{\partial y} + p\frac{\partial w}{\partial z}\right) + \tau_{xx}\frac{\partial u}{\partial x} + \tau_{yy}\frac{\partial v}{\partial y} + \tau_{zz}\frac{\partial w}{\partial x} + \tau_{yx}\left(\frac{\partial u}{\partial y} + \frac{\partial v}{\partial x}\right)$$

$$+ \tau_{zx}\left(\frac{\partial u}{\partial z} + \frac{\partial w}{\partial x}\right) + \tau_{zy}\left(\frac{\partial v}{\partial z} + \frac{\partial w}{\partial y}\right)$$

$$+ \left[\rho\dot{q} + \frac{\partial}{\partial x}\left(k\frac{\partial T}{\partial x}\right) + \frac{\partial}{\partial y}\left(k\frac{\partial T}{\partial y}\right)\right.$$

$$\left. + \frac{\partial}{\partial z}\left(k\frac{\partial T}{\partial z}\right)\right] \qquad (3.164)$$

Substituting the values of $\tau_{xx}, \tau_{yy,} \tau_{zz}$ $\tau_{yx},$ τ_{zx} and τ_{zy} from $Eqn.$ (3.132) -$Eqn.$ (3.138) into Eqn. (3.164) gives

`

$$\rho \frac{D(i)}{Dt} = -\left(p\frac{\partial u}{\partial x} + p\frac{\partial v}{\partial y} + p\frac{\partial w}{\partial z}\right) + \lambda \nabla . V\left(\frac{\partial u}{\partial x} + \frac{\partial v}{\partial y} + \frac{\partial w}{\partial x}\right)$$

$$+ \mu\left[2\left(\frac{\partial u}{\partial x}\right)^2 + 2\left(\frac{\partial v}{\partial y}\right)^2 + 2\left(\frac{\partial w}{\partial z}\right)^2 + \left(\frac{\partial u}{\partial y} + \frac{\partial v}{\partial x}\right)^2 + \left(\frac{\partial u}{\partial z} + \frac{\partial w}{\partial x}\right)^2\right.$$

$$\left. + \left(\frac{\partial v}{\partial z} + \frac{\partial w}{\partial y}\right)^2\right]$$

$$+ \left[\rho\dot{q} + \frac{\partial}{\partial x}\left(k\frac{\partial T}{\partial x}\right) + \frac{\partial}{\partial y}\left(k\frac{\partial T}{\partial y}\right)\right.$$

$$\left. + \frac{\partial}{\partial z}\left(k\frac{\partial T}{\partial z}\right)\right] \qquad (3.165)$$

$$\rho \frac{D(i)}{Dt} = -\left(p\frac{\partial u}{\partial x} + p\frac{\partial v}{\partial y} + p\frac{\partial w}{\partial z}\right) + \lambda\left(\frac{\partial u}{\partial x} + \frac{\partial v}{\partial y} + \frac{\partial w}{\partial x}\right)^2$$

$$+ \mu\left[2\left(\frac{\partial u}{\partial x}\right)^2 + 2\left(\frac{\partial v}{\partial y}\right)^2 + 2\left(\frac{\partial w}{\partial z}\right)^2 + \left(\frac{\partial u}{\partial y} + \frac{\partial v}{\partial x}\right)^2 + \left(\frac{\partial u}{\partial z} + \frac{\partial w}{\partial x}\right)^2\right.$$

$$\left. + \left(\frac{\partial v}{\partial z} + \frac{\partial w}{\partial y}\right)^2\right]$$

$$+ \left[\rho\dot{q} + \frac{\partial}{\partial x}\left(k\frac{\partial T}{\partial x}\right) + \frac{\partial}{\partial y}\left(k\frac{\partial T}{\partial y}\right)\right.$$

$$\left. + \frac{\partial}{\partial z}\left(k\frac{\partial T}{\partial z}\right)\right] \qquad (3.166)$$

$$\rho \frac{D(i)}{Dt} = \frac{\partial \rho i}{\partial t} + \frac{\partial \rho u i}{\partial x} + \frac{\partial \rho v i}{\partial y} + \frac{\partial \rho w i}{\partial z}$$

Or

`

$$\rho \frac{D(i)}{Dt} = \frac{\partial \rho i}{\partial t} + \nabla . (\rho V i)$$

Or

$$\rho \frac{D(i)}{Dt} = \frac{\partial(\mathrm{\rho i})}{\partial \mathrm{t}} + \mathrm{div}(\mathrm{\rho Vi})$$

$$\begin{aligned}
\frac{\partial(\rho i)}{\partial t} + div(\rho V i) \\
= \quad & -\left(p\frac{\partial u}{\partial x} + p\frac{\partial v}{\partial y} + p\frac{\partial w}{\partial z}\right) + \lambda\left(\frac{\partial u}{\partial x} + \frac{\partial v}{\partial y} + \frac{\partial w}{\partial x}\right)^2 \\
& + \mu\left[2\left(\frac{\partial u}{\partial x}\right)^2 + 2\left(\frac{\partial v}{\partial y}\right)^2 + 2\left(\frac{\partial w}{\partial z}\right)^2 + \left(\frac{\partial u}{\partial y} + \frac{\partial v}{\partial x}\right)^2 + \left(\frac{\partial u}{\partial z} + \frac{\partial w}{\partial x}\right)^2 \right. \\
& \left. + \left(\frac{\partial v}{\partial z} + \frac{\partial w}{\partial y}\right)^2\right] \\
& + \left[\rho\dot{q} + \frac{\partial}{\partial x}\left(k\frac{\partial T}{\partial x}\right) + \frac{\partial}{\partial y}\left(k\frac{\partial T}{\partial y}\right)\right. \\
& \left. + \frac{\partial}{\partial z}\left(k\frac{\partial T}{\partial z}\right)\right] \qquad (3.167)
\end{aligned}$$

Eqn. (3.166) is the energy equation as a function of internal energy in conservation form.

Following the same argument as above, the total energy equation in Eqn. (3.156) can be written in conservation form as;

$$\frac{\partial}{\partial t}\left[\rho\left(i+\frac{V^2}{2}\right)\right]+div\left[\rho V\left(i+\frac{V^2}{2}\right)\right]$$

$$=-\left(\frac{\partial up}{\partial x}+\frac{\partial vp}{\partial y}+\frac{\partial wp}{\partial z}\right)$$

$$+\left(\frac{\partial u\tau_{xx}}{\partial x}+\frac{\partial u\tau_{yx}}{\partial y}+\frac{\partial u\tau_{zx}}{\partial z}+\frac{\partial v\tau_{xy}}{\partial x}+\frac{\partial v\tau_{yy}}{\partial y}+\frac{\partial v\tau_{zy}}{\partial z}+\frac{\partial w\tau_{xz}}{\partial x}+\frac{\partial w\tau_{yz}}{\partial y}\right.$$

$$\left.+\frac{\partial w\tau_{zz}}{\partial z}\right)dxdydz+\ \rho g.V$$

$$+\left[\rho\dot{q}+\frac{\partial}{\partial x}\left(k\frac{\partial T}{\partial x}\right)+\frac{\partial}{\partial y}\left(k\frac{\partial T}{\partial y}\right)+\frac{\partial}{\partial z}\left(k\frac{\partial T}{\partial z}\right)\right] \qquad (3.168)$$

The governing equations so far derived appear similar in some ways. The Suppression of the dissimilarities will give the conservative flow equation for an arbitrary variable Ø as

$$\frac{\partial(\rho\emptyset)}{\partial t}+div(\rho V\emptyset)=div(\Gamma\ grad\ \emptyset)+S_{\emptyset} \qquad (3.169)$$

The interpretation is

The rate of increase of fluid element Ø + The net rate of flow of Ø out of the = Rate of increase Ø due to diffusion + The source points Ø rise.

Eqn (3.168) is the **transport equation** for the property Ø and forms the basis for numerical computation procedures.

`

3.4.4 Discretization

Finite difference and finite volume methods are the major algebraic approaches to solving differential equations governing the fluid flow. A computer solves a large number of algebraic expressions from this process. The finite element method is also popular but traditionally for physical mechanics.

The numerical concept is simple, but the calculations are lengthy and approximate due to round-off errors. High-speed digital computers reduce the computation time and errors associated with numerical approximations.

3.4.5 Finite Difference Method

Regarding Figure 3.13, $\frac{\mathrm{dt}}{\mathrm{dx}}$ is the true tangent to the curve. The tangent estimate is also possible by backward differencing, forward differencing, and central differencing and is in Eqn. (3.170), (3.171) and (3.172), respectively.

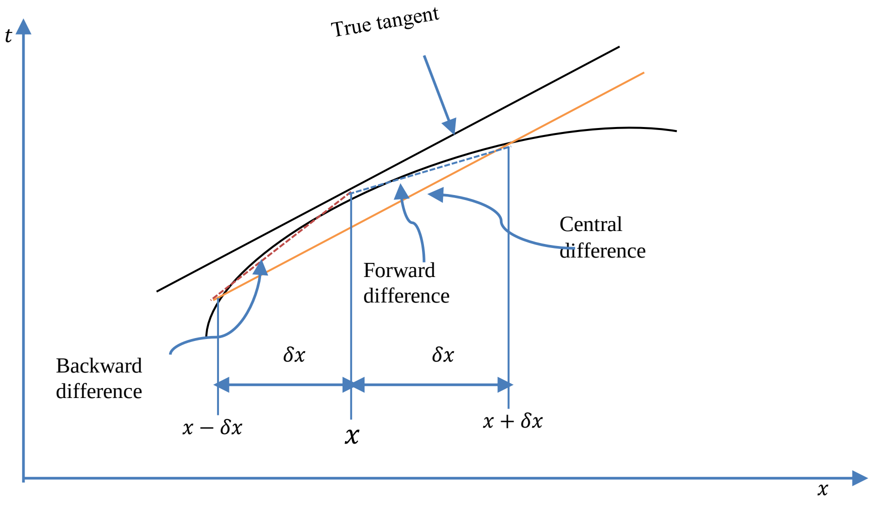

Figure 3.13 Backward, forward, and central difference approximations

Backward differencing

`

$$\frac{dt}{dx} \approx \frac{t_x - t_{x-\delta x}}{\delta_x}$$

Forward differencing

$$\frac{dt}{dx} \approx \frac{t_{x+\delta x} - t_x}{\delta_x} \qquad (3.170)$$

Central differencing

$$\frac{dt}{dx} \approx \frac{t_{x+\delta x} - t_{x-\delta x}}{2\delta_x} \qquad (3.171)$$

A more elaborate derivation of the Eqn. (3.170) to Eqn. (3.172) can be achieved using Taylor series expansion. This approach will reveal that the higher-order terms of the equations were neglected and constitute the truncation error. Therefore, the equations as written above are an approximate representation of the differential equation. A more formal way of writing the equations would be

$$\frac{dt}{dx} = \frac{t_x - t_{x-\delta x}}{\delta_x} + O\delta_x \qquad (3.172)$$

$$\frac{dt}{dx} = \frac{t_{x+\delta x} - t_x}{\delta_x} + O\delta_x \qquad (3.173)$$

The notation $O\delta_x$ is the truncation error written in terms of the order of δ_x. In backward and forward difference representations, the least truncation error involves δ_x to the first power, which is first-order accurate.

The derivation of central difference expression can be by subtracting the Taylor series representation of the backward difference from the forward. The lowest order term in the truncation error term involves $(\delta_x)^2$. Therefore, the central difference expression is second-order accurate and the most accurate of the three representations.

$$\frac{dt}{dx} = \frac{t_{x+\delta x} - t_{x-\delta x}}{2\delta_x} + O(\delta_x)^2 \tag{3.174}$$

Extending this to the second derivative $\frac{d^2t}{dx^2}$, the rate of change of slope over a distance δ_x so that;

$$\frac{d^2t}{dx^2} = \left\{\frac{t_{x+\delta x} - t_x}{\delta_x} - \frac{t_x - t_{x-\delta x}}{\delta_x}\right\}\frac{1}{\delta_x} \tag{3.175}$$

$$\frac{d^2t}{dx^2} = \frac{t_{x+\delta x} + t_{x-\delta x} - 2t_x}{{\delta_x}^2} + O(\delta_x)^2 \tag{3.176}$$

The solution to the partial differential equation involves the algebraic representation over the discretized domain. For a plate of length l and width w. The faces are at four different temperatures $t_1, t_2, t_3, and\ t_4$ (Figure 3.14). If the heat conduction in the plate is at a steady state and there is no internal heat generation, the Laplace equation can estimate the temperature distribution in the plate.

`

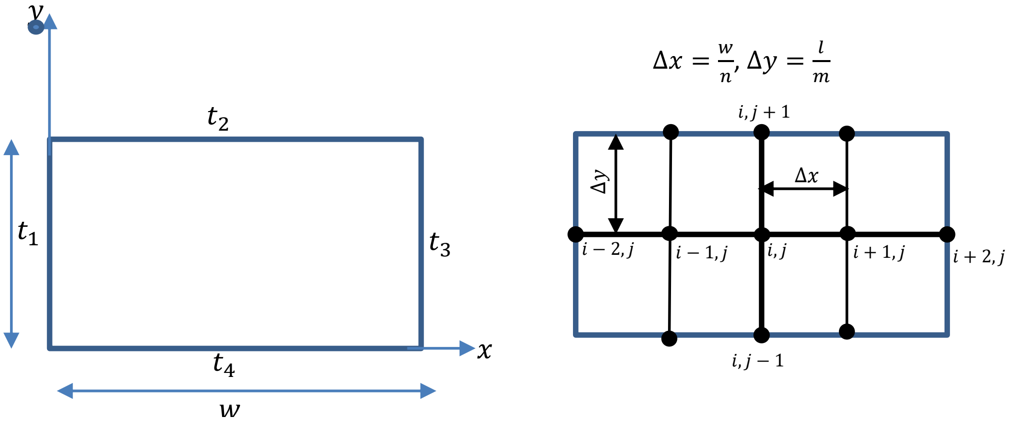

Figure 3.14 Finite difference representation of Laplace equation on a discretized two-dimensional domain

$$\frac{\partial^2 t}{\partial x^2} + \frac{\partial^2 t}{\partial y^2} = 0 \tag{3.177}$$

From $Eqn(3.177)$

$$\frac{\partial^2 t}{\partial x^2}(x, y) = \frac{t_{x+\delta x} + t_{x-\delta x} - 2t_x}{\Delta x^2} \tag{3.178}$$

$$\frac{\partial^2 t}{\partial y^2}(x, y) = \frac{t_{y+\delta y} + t_{y-\delta y} - 2t_y}{\Delta y^2} \tag{3.179}$$

If the node's labels are in terms of (i, j), then the temperature at node i, j will be;

$$\frac{\partial^2 t}{\partial x^2} + \frac{\partial^2 t}{\partial y^2} = \frac{t_{i+1,j} + t_{i-1,j} - 2t_{ij}}{\Delta x^2} + \frac{t_{j+1,i} + t_{j-1,i} - 2t_{ij}}{\Delta y^2} = 0 \tag{3.180}$$

3.4.6 Finite Volume Method

Of all the numerical techniques, the finite volume method is the most adapted to solving problems relating to fluid mechanics due to its local conservation characteristic. This approach involves the division of the computational domain into control volumes and the governing equation integration over the control volumes to yield a discretized equation at its nodal points.

Consider the steady-state diffusion of the property Ø through a one-dimensional domain governed by,

$$\frac{d}{dx}\left[\Gamma\frac{d\emptyset}{dx}\right]=0 \tag{3.181}$$

The plate can be divided into discrete volumes (Figure 3.15) so that the physical and the control volume boundaries will coincide. P is the reference node. Nodes L on the left (l) and R on the right (r) boundaries are midway through P.

The distances between nodes and the boundaries of the control volume with respect to P are as indicated.

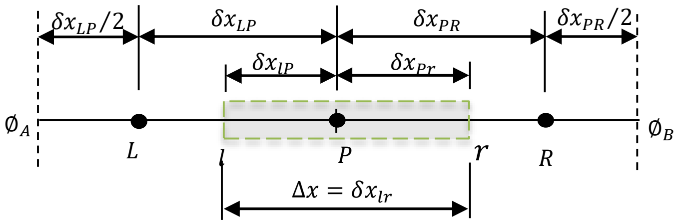

Figure 3.15 Finite volume discretization

Integrating $Eq(3.182)$ over the control volume gives;

`

$$\int_{l}^{r} \frac{d}{dx}\left[\Gamma \frac{d\emptyset}{dx}\right] dx = \left[\Gamma A \frac{d\emptyset}{dx}\right]_r - \left[\Gamma A \frac{d\emptyset}{dx}\right]_l = 0 \tag{3.182}$$

$$\Gamma_r = \frac{\Gamma_P + \Gamma_R}{2} \tag{3.183}$$

$$\Gamma_l = \frac{\Gamma_L + \Gamma_P}{2} \tag{3.184}$$

$$\left[\Gamma A \frac{d\emptyset}{dx}\right]_r = \Gamma_r A_r \left[\frac{\emptyset_R - \emptyset_P}{\delta x_{PR}}\right] \tag{3.185}$$

$$\left[\Gamma A \frac{d\emptyset}{dx}\right]_l = \Gamma_l A_l \left[\frac{\emptyset_P - \emptyset_L}{\delta x_{LP}}\right] \tag{3.186}$$

Substituting Eqn. (3.186) and Eqn. (3.187) into Eqn. (3.183) gives;

$$\Gamma_r A_r \left[\frac{\emptyset_R - \emptyset_P}{\delta x_{PR}}\right] - \Gamma_l A_l \left[\frac{\emptyset_P - \emptyset_L}{\delta x_{LP}}\right] = 0 \tag{3.187}$$

Expansion and arrangement of Eqn. (3.188) gives

$$\Gamma_r A_r \frac{\emptyset_R}{\delta x_{PR}} - \Gamma_r A_r \frac{\emptyset_P}{\delta x_{PR}} - \Gamma_l A_l \frac{\emptyset_P}{\delta x_{LP}} + \Gamma_l A_l \frac{\emptyset_L}{\delta x_{LP}} = 0 \tag{3.188}$$

$$\left[\frac{\Gamma_r A_r}{\delta x_{PR}} + \frac{\Gamma_l A_l}{\delta x_{LP}}\right] \emptyset_P = \frac{\Gamma_r A_r}{\delta x_{PR}} \emptyset_R + \frac{\Gamma_l A_l}{\delta x_{LP}} \emptyset_L \tag{3.189}$$

If

$$\frac{\Gamma_r A_r}{\delta x_{PR}} = k_R \tag{3.190}$$

`

$$\frac{\Gamma_l A_l}{\delta x_{LP}} = k_L \tag{3.191}$$

and

$$\frac{\Gamma_r A_r}{\delta x_{PR}} + \frac{\Gamma_l A_l}{\delta x_{LP}} = k_P \tag{3.192}$$

Eqn. (3.190)

can be written as

$$k_P \emptyset_P = k_R \emptyset_R + k_L \emptyset_L \tag{3.193}$$

Eqn. (3.195) for node P applies only to interior nodes. The boundary nodes (L and R) are different.

Integration of Eqn. (3.182) over the control volume gave

$$\left[\Gamma \mathrm{A} \frac{\mathrm{d}\emptyset}{\mathrm{dx}}\right]_{\mathrm{r}} - \left[\Gamma \mathrm{A} \frac{\mathrm{d}\emptyset}{\mathrm{dx}}\right]_{\mathrm{l}} = 0$$

For the control volume at the left boundary (Figure 3.15)

$$\left[\Gamma A \frac{d\emptyset}{dx}\right]_r = \Gamma_r A_r \frac{\emptyset_P - \emptyset_L}{\delta x_{LP}} \tag{3.194}$$

$$\left[\Gamma A \frac{d\emptyset}{dx}\right]_l = \Gamma_l A_l \frac{2(\emptyset_L - \emptyset_A)}{\delta x_{LP}} \tag{3.195}$$

$$\Gamma_r A_r \frac{\emptyset_P - \emptyset_L}{\delta x_{LP}} - \Gamma_l A_l \frac{2(\emptyset_L - \emptyset_A)}{\delta x_{LP}} = 0 \tag{3.196}$$

$$\frac{\Gamma_r A_r}{\delta x_{LP}} \emptyset_P - \frac{\Gamma_r A_r}{\delta x_{LP}} \emptyset_L - \frac{2\Gamma_l A_l}{\delta x_{LP}} \emptyset_L + \frac{\Gamma_l A_l}{\delta x_{LP}} \emptyset_A = 0 \tag{3.197}$$

$$\left(\frac{\Gamma_r A_r}{\delta x_{LP}} + \frac{2\Gamma_l A_l}{\delta x_{LP}}\right) \emptyset_L = \frac{\Gamma_r A_r}{\delta x_{LP}} \emptyset_P + \frac{\Gamma_l A_l}{\delta x_{LP}} \emptyset_A \tag{3.198}$$

`

The algebraic equation for the control volume at the right-hand is;

$$\left(\frac{\Gamma_l A_l}{\delta x_{PR}}+\frac{2\Gamma_r A_r}{\delta x_{PR}}\right)\emptyset_R=\frac{\Gamma_l A_l}{\delta x_{PR}}\emptyset_P+\frac{\Gamma_r A_r}{\delta x_{PR}}\emptyset_B \tag{3.199}$$

In the algebraic representation of the governing equation for steady-state diffusion, the central differencing scheme is second-order accurate and gives a good approximation. In fluid flow problems, there is a need to account for convection. If the source term is negligible, the steady state fluid flow equation becomes

$$\frac{d}{dx}(\rho u\emptyset)=\frac{d}{dx}\left(\Gamma\frac{d\emptyset}{dx}\right) \tag{3.200}$$

the left-hand side of the Eqn. (3.201) is the net convective flux, and the right-hand side is the diffusive flux.

In discretizing the convective part with the central differencing scheme, the numerical solutions do not always agree with the analytical but rather wiggle or oscillate about the exact value (Versteeg & Malalasekera, An Introduction to Computational Fluid Dynamics, 2007). Therefore, for general-purpose flow computations, the central differencing scheme does not always give a realistic solution for convective terms, hence the need for a different approach. In CFD codes, the discretization of the diffusion term in the flow equation is by a central differencing scheme, while the convection term uses a separate scheme. The schemes available in ANSYS fluent include first-order upwind, second-order upwind, power law, and QUICK (ANSYS Inc, 2009).

In upwind schemes, the computation of the face value quantity of interest is by the upstream quantity values. This accounts for the flow direction, hence an advantage over the central differencing scheme, which does not indicate flow direction.

`

Generally, second-order discretization yields more accurate results than first-order schemes, but they are difficult to converge. However, when the flow is laminar and aligned with the mesh, first-order upwind discretization may give an acceptable result.

The power law scheme will yield the same result as the first-order scheme (ANSYS, Inc., 2010). QUICK is applied to quadrilateral or hexahedral meshes but is not suitable for hybrid mesh and will not give a significant improvement in accuracy over the second-order schemes (ANSYS, Inc., 2010).

3.5 Solution Procedure

. The procedures in this work are the analytical and the finite volume numerical solution. The implementation of the analytical models was on MATLAB, and the 3D numerical solutions on ANSYS fluent.

3.5.1 Analytical Solution on MATLAB

Unlike other programs that only solve predefined equations, MATLAB offers some flexibility because it permits the user to implement models with little or no interference. A correct code will run successfully on MATLAB, be it a 1D, 2D, or 3D model if the hardware resources are sufficient.

The MATLAB code for this investigation consists of the script and some user-defined functions. The user-defined functions are functions predefined by the user to carry out the specified operation when called. These functions do the necessary computation and feed the output to the script.

The following are the procedures for writing the code. First is the definition of the conditions at flow inlet. The code prompts the user to enter the fuel species and their mole fraction, the initial temperature of the fuel/air, and the angle of spread of the jet. It only permits three fuel species- propane, butane, and methane and the entry must follow the order. The physical properties like the fuel density are temperature dependent. Their computation using user-defined functions was at the inlet temperatures and called up as an input to the primary code.

Next is the definition of axial and radial points of interest in the domain and implementation of the analytical model models at the points.

3.5.2 **Numerical Solution Approach**

The procedure for solving the flow equations using ANSYS workbench is geometry/domain creation, grid or mesh generation, problem definition/setup, the solution of the discretized equation over the domain, and presentation/display of the result.

3.5.2.1 **Geometry/Domain creation**

The geometry creation was in ANSYS design modeller. Considering the symmetric nature of the domain and the need to conserve time and computer memory, half of it will suffice. The dimensioning was in millimetres and degrees for lengths and angles, respectively. Creating the geometry will involve the sketch creation of the domain, surface generation, and the revolution of the surface to create the 3D model.

3.5.2.2 **Mesh Generation**

The solution to the linear representation of the flow equations is at the nodes spread throughout the domain, hence, the discretization of the flow domain into small elements called cells or control volumes. The arrays of these cells are the mesh. The solution is approximate, and the accuracy of the CFD solution is affected by the mesh quality (Cengel & Cimbal, 2006).

In ANSYS fluent, 2D meshes are defined using quadrilateral and triangular cells (Figure 3.16), while for 3D meshes, hexahedral, tetrahedral, pyramid, wedge, and polyhedral are used (Figure 3.17) (ANSYS, Inc., 2010).

A mesh can be structured, unstructured, or hybrid. Structured mesh has a regular connectivity i.e., the nodal arrangement is such that the rows and columns are clearly defined. Therefore, a structured 2D mesh will consist of quadrilaterals while it is hexahedral for 3D mesh so that each cell has the same number of neighbours (Figure 3.18).

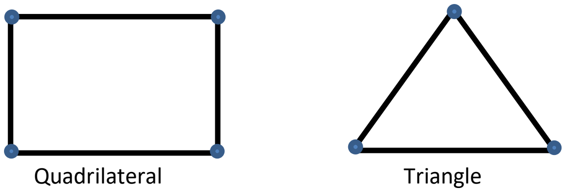

Figure 3.16 2D cell type (ANSYS, Inc., 2010)

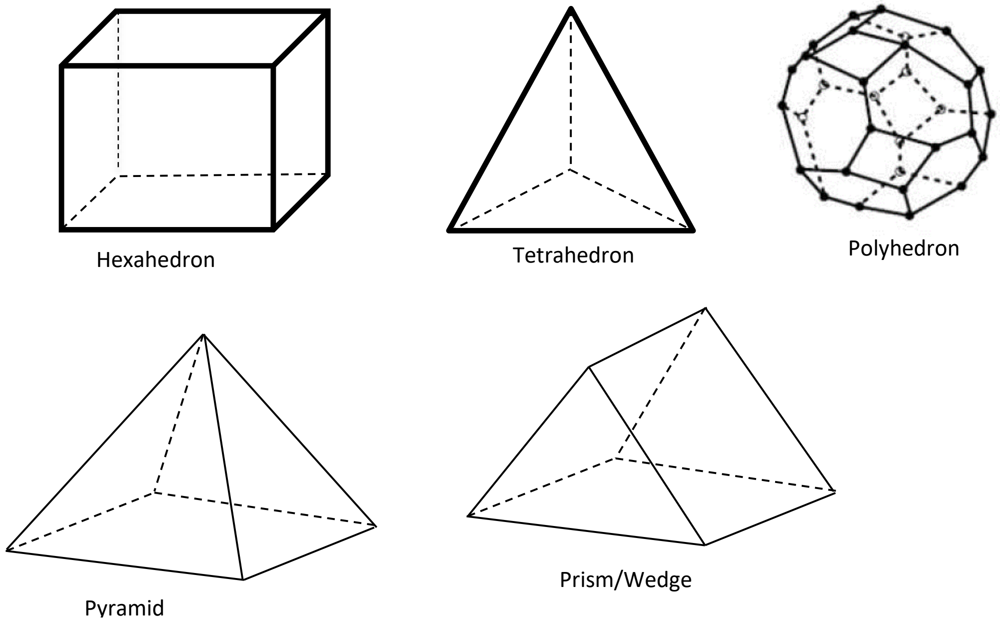

Figure 3.17 3D cell type (ANSYS, Inc., 2010)

The unstructured mesh, unlike the structured ones, is irregular and does not have clearly defined rows and columns. It consists of a quadrilateral or triangle for 2D mesh and a tetrahedron or hexahedron for 3D mesh. Figure 3.18 compares the structured and unstructured mesh for the same domain. Hybrid mesh combines blocks of structured and unstructured mesh. They are often used to achieve varying degrees of mesh density or resolution in the region of interest. Usually, the structured mesh mapping is in sections of the domain, like the wall, that require very high accuracy. The unstructured mesh is for regions far away from the wall or outside the influence of the boundary layer. Regardless of the mesh type, the quality is critical as it plays a significant role in the stability and accuracy of the numerical computation.

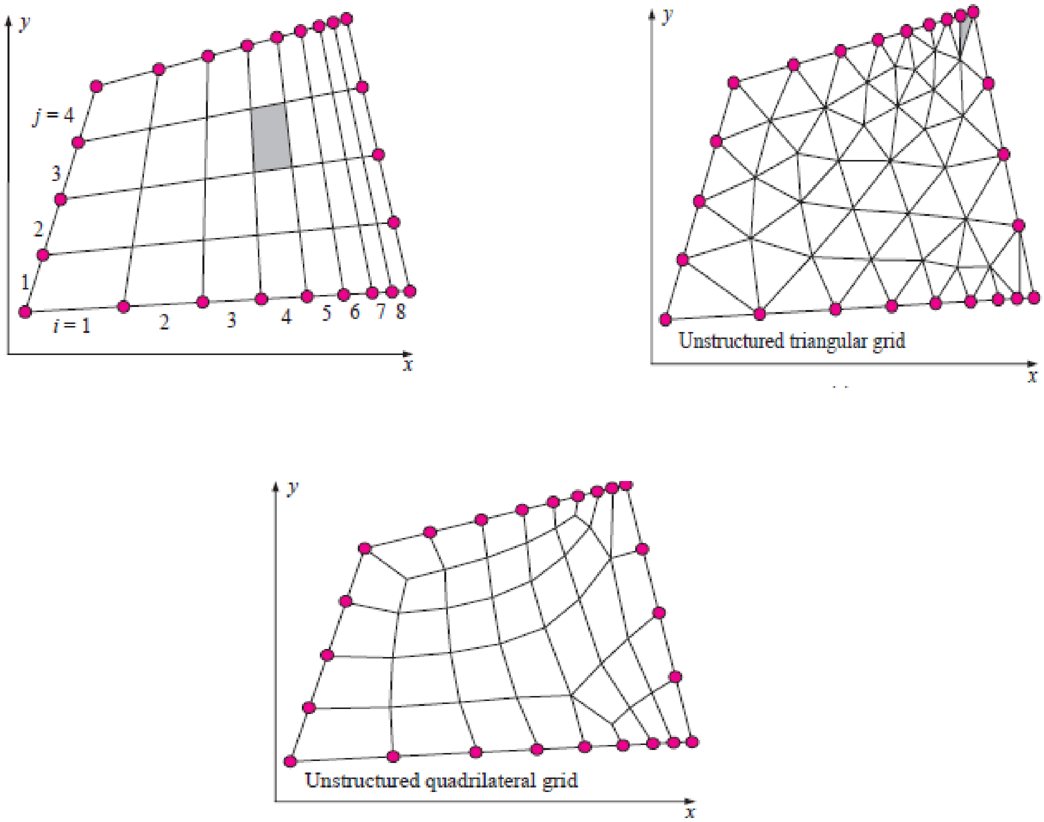

Figure 3.18 Structured and unstructured 2D Grid

`

3.5.2.2.1 **Mesh Quality**

Some measures of mesh grade include the orthogonal quality, aspect ratio, skewness, mesh element distribution, and smoothness.

3.5.2.2.2 **Orthogonal Quality**

For a given cell, the value of orthogonal quality ranges from 0 to 1, with the best cell having a value close to 1. The minimum acceptable value for orthogonal quality is 0.01. It is, however, significantly higher on the average.

3.5.2.2.3 **Aspect Ratio**

The aspect ratio is the measure of the stretching of the cell. It is the ratio of the maximum value to the minimum value of the distance between the cell centroid and the face centroid or the distance between the cell centroid and nodes. It is best to avoid sudden changes in cell aspect ratio, especially in regions where the flow exhibits rapid changes (ANSYS, Inc., 2010).

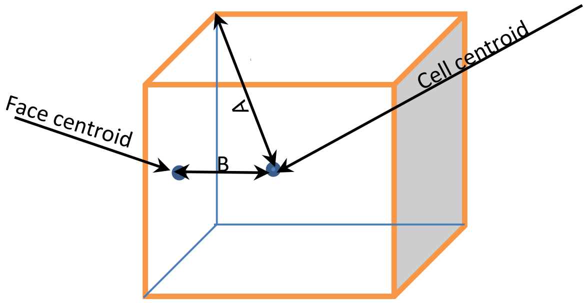

Figure 3.19 Aspect ratio (ANSYS, Inc., 2010)

For Figure 3.19, the aspect ratio will be given by;

$$Aspect\ ratio = \frac{A}{B}$$

The data of the minimum values of orthogonal quality and the maximum values of the aspect ratio of a mesh is in the report quality console on the general task page of ANSYS fluent.

3.5.2.2.4 **Mesh Distribution and Density**

The resolution of critical flow features such as boundary layer, flow separation, and recirculation is better if the mesh density is high. Low mesh density may be applicable in regions far away from the wall or outside the influence of the boundary layer. In critical flow regions like walls in a viscous flow, low-density mesh will give less accurate results. Therefore, the mesh distribution close to the walls should be dense in resolved boundaries.

3.5.2.2.5 **Skewness**

Skewness is a departure from symmetry or the difference between the shape of a mesh and the shape of an equilateral cell of equivalent volume. An example of a highly skewed triangular cell is a shaded cell in the unstructured triangular grid of Figure 3.18. Highly skewed cells can decrease accuracy and destabilize the solution. The general rule is that the maximum skewness of a triangular or tetrahedral mesh should be below 0.95, with an average value that is significantly lower (ANSYS, Inc., 2010).

3.5.2.2.6 **Smoothness**

Unsmoothed mesh has rapid changes in the cell volume of adjacent cells and can cause truncation errors, which is the cause of numerical diffusion. Refining the cell based on cell volume or gradient of cell volume improves smoothness.

3.5.2.3 **Problem Definition/Setup**

The simulation was with ANSYS Fluent - a finite volume CFD code. The first step towards defining the problem is the acceptability of the mesh quality and the calibration of the solver parameters. For mesh quality, the considered parameters are the minimum orthogonal quality and aspect ratio, which were

`

$7.95073e^{-02}$ and $3.20509e^{+1}$, respectively. Others include domain extent, volume, and face area statistics. The discretization was by tetrahedron elements. In addition to stability in the computation process, it is quicker to generate compared to structured mesh because of the complexity of the geometry. The modelling of near-wall flow was by the standard wall function. The first layer thickness of the mesh was set to 4.18e-2 to account for the $Y^{+} \approx 30$ (Figure 3.20 and Figure 3.21).

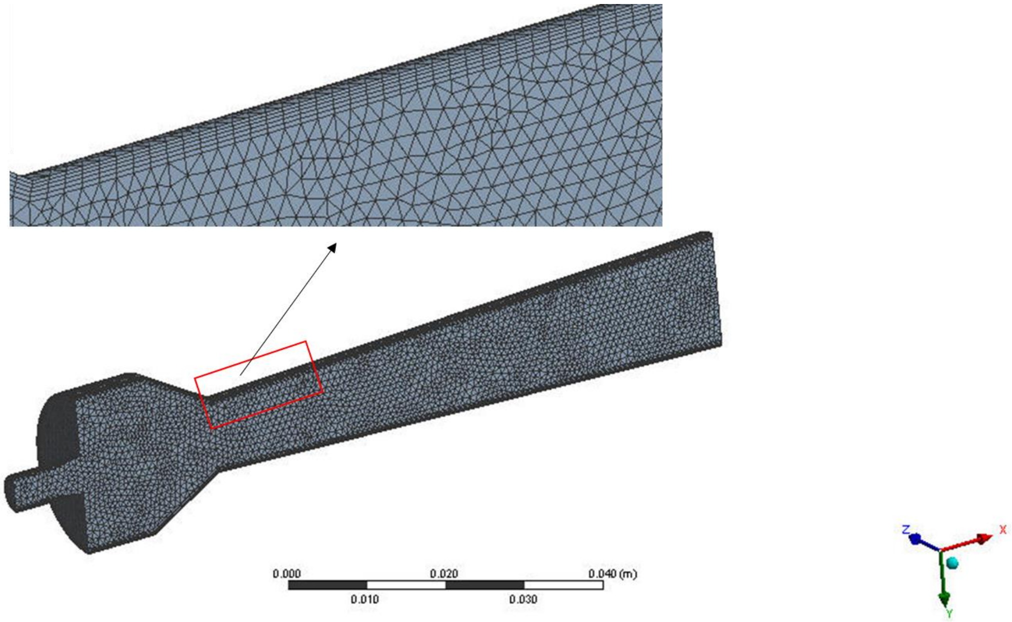

Figure 3.20 Mesh profile for optimum nozzle position

`

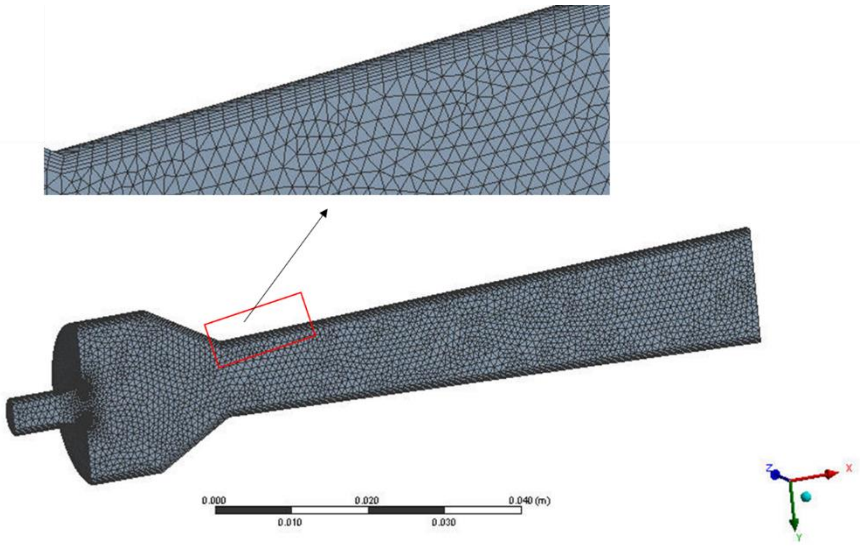

Figure 3.21 Mesh profile for flow modified with ring

3.5.2.3.1 **Grid independence Study**

Considering the critical influence of the mesh on the accuracy and stability of the CFD solution, it is standard practice to confirm that the solution is grid independent i.e., to check that the solution obtained does not vary significantly with an increase in grid resolution.

The investigation of the independence of the simulation result on the number of cells was with four grids. The cell numbers ranged from 69405 to 498754. The plots of the pressure coefficient and mean velocity at the centreline for each of the grids are in Figure 3.22. The mean velocity data (Figure 3.22a), when the mesh quantity was 69405, was distinct from the rest. As the cell numbers increased, the differences became negligible. Also, the variation in pressure coefficient (Figure 3.22b) was more apparent in the diffuser. However, the differences were reduced with the increase in the number of cells. Concerning the mean velocity at the centreline, the highest discrepancy was at $X/d_N = 10$. When the number of cells increased from 231779 to 498754 ($a\ 115.2\%$ increase), the change in centreline velocity and static pressure values, respectively, at $X/d_N = 10$, were 3.2% and 4.3%. Hence, the computation was with ≈230,000 cells for accuracy and optimal computation time.

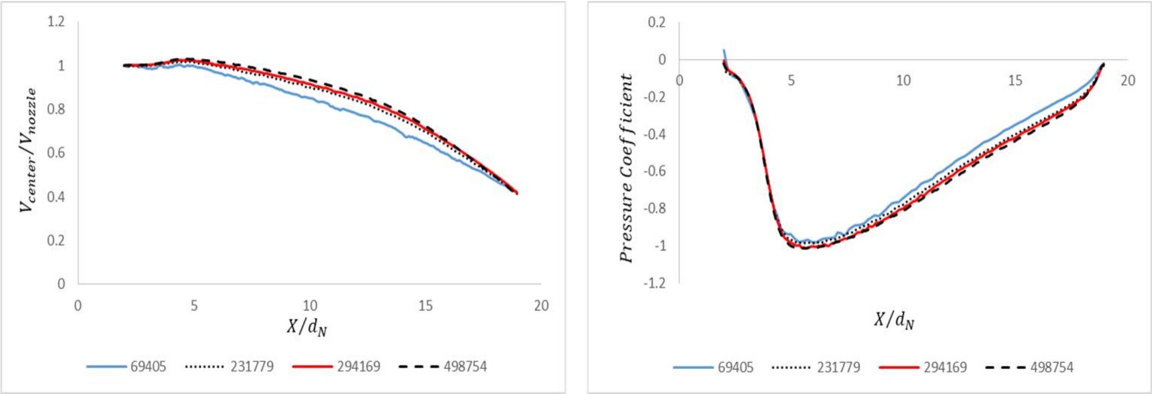

Figure 3.22 Variation in velocity (left) and pressure coefficient (right) at the centreline with number of elements

3.5.2.3.2 **Solution Techniques**

Solution techniques in CFD computations are pressure-based and density-based solvers, which traditionally are for incompressible and compressible flows, respectively. Two formulations exist for each of these techniques; they are explicit and implicit formulations for density-based solvers and segregated and coupled for pressure-based solvers. In pressure-based solvers, the coupling of velocity and pressure using a segregated procedure is with the SIMPLE, SIMPLEC, and PISO algorithms. The COUPLED algorithm is only applicable to coupled pressure-based solvers. SIMPLE, SIMPLEC and COUPLED algorithms are for steady-state flows, while PISO performs well for transient flow calculations with higher time steps because of its stability. SIMPLE and SIMPLEC are, however, advantageous when using turbulence model like LES that requires small time steps because using PISO will increase the computation time.

`

The chosen solver was the pressure-based solver. The computation was for steady-state, and the pressure velocity coupling was by the COUPLED algorithm because of its robustness and efficiency in single-phase steady-state flows.

Because of the symmetric nature of the structure, the computation was carried out in half of the domain to conserve time and computer memory (Figure 3.20 and Figure 3.21). Propane and air were the motive and secondary fluids, respectively, and spatial discretization for momentum and turbulent kinetic energy was by second-order upwind.

3.5.2.3.3 **Boundary Conditions**

The boundary condition is the flow and thermal variables at the boundaries of the system or physical model (ANSYS, Inc., 2010). In CFD applications, the fluid flow equations are the same, irrespective of the domain. Even for problems with similar geometry, the uniqueness of the solution will depend on the boundary and sometimes the initial condition. Therefore, any meaningful solution to the governing flow equations must correctly capture the boundary conditions.

Boundary types are many. The considerations here will be the ones that are relevant to this work, and they include the wall boundaries, inlet boundaries, outlet boundaries, and cell zone conditions.

Wall boundary condition

For stationary walls, the velocity of the viscous fluid layer in contact with the wall is zero. This is known as the no-slip condition. The setup involved solutions to energy equations. Therefore, in addition to the no-slip boundary condition, there was a specification of the wall temperature. The wall roughness was negligible.

Inlet/outlet boundary conditions

`

There is a wide range of options when specifying the conditions at inlet and exit. Some inlet and exit boundary condition options include velocity inlet, pressure inlet, mass flow inlet, pressure outlet, pressure far field, etc. The pressure outlet condition produces better convergence when backflow occurs during iteration, and it is usually specified as atmospheric pressure (zero gauge pressure) in many cases.

Cell zones/Interior boundary

This is the region bounded by the walls. This may be liquid only or a combination of solid and liquid. When the designation is fluid for a group of cells, the CFD code solves the heat, flow, and even turbulence equations. When they are solid, only the heat equation is solved. The only required input in the interior boundary is the specification of the material type. There are options to set sources or fixed values for mass, momentum, heat, and species for a fluid cell zone. For solid cells, the requirements are a heat source and fixed temperatures. The summary of the boundary conditions is in Table 3.1. The turbulence viscosity ratio and turbulence intensity at the inlet were 10, and 5%, respectively.

Table 3.1 Boundary layer parameters used for the simulation

Boundary zone	**Boundary Type**	**Value of Parameters**		
		Velocity $(\boldsymbol{m/s})$	**Pressure** $(\boldsymbol{Pa})$	**Specie mass fraction**
Air inlet	Pressure inlet	0	0	0.233 (O_2)
Fuel inlet	Velocity inlet	2	-	1 (C_3H_8)
symmetry	Axis	-	-	-
Outlet	Pressure outlet	-	0	-
Walls	Wall	No slip	-	-

3.5.2.3.4 **Closure models**

The closure options explored were the Realizable $k-\varepsilon$ and Reynolds stress model (RSM). The equations are as presented.

1) The Realizable $k-\varepsilon$ model relates Reynolds stress to the mean velocity gradient as

$$-\rho\overline{u'}_i\overline{u'}_j = \left(\frac{\partial u_i}{\partial x_j}+\frac{\partial u_j}{\partial x_i}\right)-\frac{2}{3}\delta_{ij}\left(\rho k+\mu_t\frac{\partial u_k}{\partial x_k}\right) \qquad (3.202)$$

In the Realisable k-ε model, the transport equations for k and ε, respectively, are

$$\rho u\frac{\partial k}{\partial x}+\rho v\frac{\partial k}{\partial y}+\rho w\frac{\partial k}{\partial z}=\left(\mu+\frac{\mu_t}{\sigma_k}\right)\left[\frac{\partial^2 k}{\partial x^2}+\frac{\partial^2 k}{\partial y^2}+\frac{\partial^2 k}{\partial w^2}\right]+G_k+G_b-\rho\varepsilon-Y_M-S_k \qquad (3.203)$$

and

$$\rho u\frac{\partial \varepsilon}{\partial x}+\rho v\frac{\partial \varepsilon}{\partial y}+\rho w\frac{\partial \varepsilon}{\partial z}=\left(\mu+\frac{\mu_t}{\sigma_\varepsilon}\right)\left[\frac{\partial^2 \varepsilon}{\partial x^2}+\frac{\partial^2 \varepsilon}{\partial y^2}+\frac{\partial^2 \varepsilon}{\partial w^2}\right]+\rho C_1 S_\varepsilon-\rho C_2\frac{\varepsilon^2}{k+\sqrt{v\varepsilon}}+C_{1\varepsilon}\frac{\varepsilon}{k}C_{3\varepsilon}G_b+S_\varepsilon \qquad (3.204)$$

where

$$\mathrm{C}_1=\left[0.43,\frac{\eta}{\eta+5}\right],\quad \eta=S\frac{k}{\varepsilon},\quad S=\left(2S_{ij}S_{ij}\right)^{1/2},\quad S_{ij}=\frac{1}{2}\left(\frac{\partial u_i}{\partial x_j}+\frac{\partial u_j}{\partial x_i}\right)$$

G_k is the term for turbulent kinetic energy generation, G_b represents the generation of turbulence due to buoyancy, $\mathrm{Y_M}$ is the contribution of fluctuating dilation in compressible turbulence to overall dissipation rate $C_2 = 1.9$ and $C_{1\varepsilon} = 1.44$ are constants, $\sigma_k = 1$ and $\sigma_\varepsilon = 1.2$ are turbulent Prandtl numbers for k and ε respectively. $\mathrm{S_k}$ and $\mathrm{S_\varepsilon}$ are user-defined source terms. $\mathrm{C}_{3\varepsilon} = 1$ for buoyant shear in the main flow direction; and zero for shear layers perpendicular to the gravitational vector.

$$\mu_t=\rho C_\mu\frac{k^2}{\varepsilon} \qquad (3.205)$$

Where

$$C_\mu=\frac{1}{A_o+A_s\frac{kU^*}{\varepsilon}},\quad A_o=4.04,\quad A_s=\sqrt{6}\,cos\,\phi\quad,\quad \phi=\frac{1}{3}cos^{-1}\left(\sqrt{6W}\right),W=\frac{S_{ij}S_{jk}S_{ki}}{\check{S}^3},\quad \check{S}=\left(S_{ij}S_{ij}\right)^{1/2}$$

`

and

$$U^* = \left(S_{ij}S_{ij}\breve{\Omega}_{ij}\breve{\Omega}_{ij}\right)^{1/2} \quad \breve{\Omega}_{ij} = \Omega_{ij} - 2\varepsilon_{ijk}\omega_k, \qquad \Omega_{ij} = \bar{\Omega}_{ij} - \varepsilon_{ijk}\omega_k$$

$\bar{\Omega}_{ij}$ is the mean rate of rotation tensor with angular velocity ω_k

2) The summary of the Reynolds stress $-\rho\overline{u'_i u'_j}$ transport equations are (ANSYS Inc, 2009) (Versteeg & Malalasekera, An introduction to Computational Fluid Dynamics an Introduction, 1995) (Chung T. J., 2002)

$$\frac{\partial}{\partial t}\left(\rho\overline{u'_i u'_j}\right) + \frac{\partial}{\partial x_k}\left(\rho u_k\overline{u'_i u'_j}\right) = -\frac{\partial}{\partial x_k}\left(\rho\overline{u'_k u'_i u'_j} + p\overline{\left(\delta_{kj}u'_i + \delta_{ik}u'_j\right)}\right) + \frac{\partial}{\partial x_k}\left[\mu\frac{\partial}{\partial x_k}\left(\overline{u'_i u'_j}\right)\right]$$

$$-\rho\left(\overline{u'_i u'_k}\,\frac{\partial u_j}{\partial x_k} + \overline{u'_j u'_k}\,\frac{\partial u_i}{\partial x_k}\right) - \rho\beta\left(g_i\overline{u'_j\theta} + g_j\overline{u'_i\theta}\right) + p\overline{\left(\frac{\partial u'_i}{\partial x_j} + \frac{\partial u'_j}{\partial x_i}\right)} - 2\mu\overline{\frac{\partial u'_i}{\partial x_k}\frac{\partial u'_j}{\partial x_k}}$$

$$-2\Omega\rho_k\left(\overline{u'_j u'_m}\varepsilon_{ikm} + \overline{u'_i u'_m}\varepsilon_{jkm}\right) + S_{user} \tag{3.206}$$

The first term on the left-hand side of the equation is the local time derivative, and the second is the convective term. On the right-hand side, the first term is turbulent diffusion, the second is molecular diffusion, the third is the stress production term, and the fourth, fifth, and sixth represent buoyancy production, pressure strain, and dissipation. The seventh and eighth terms are production by system rotation and user-defined function.

3.5.2.3.5 **Wall Treatment**

Turbulence models like Ke, RSM, and even LES are primarily for flows far away from walls. Close to solid boundaries, the flow behaves differently because of the dominance of viscous forces, and the mean flow velocity will depend on the distance from the wall, the density of the fluid, and wall shear stress. The near-wall treatment weighs strongly on the accuracy of wall-bounded flows. The flow near the walls is either resolved or modeled. Resolving the flow will require a high concentration of cells near the walls, which is expensive per CUP resources and time. The modeling alternative is by wall function approach. This is economical because the run time is fast due to the smaller number of cells. It is also robust and reasonably accurate, hence, a practical option for industrial flow simulation.

3.5.2.3.6 Yplus

Y+ is a dimensionless quantity used to measure the distance from the wall in viscous lengths. It distinguishes the different near-wall regions. The viscous sub layer and the buffer layer fall below Y+= 30, and the modeling was with the standard wall function. The centroid of the first mesh was in the log law region between (30<Y+ < 300). Outside this boundary, errors may arise in the computation at the first cell and will affect the credibility of the entire result.

3.5.2.3.7 **Convergence Criteria**

The residual level and physical solution quantities are the metrics for evaluating convergence. The considered physical quantity is the mass-weighted average of the velocity magnitude. At the end of each solver iteration is the computation and storage of the sum of the residual for each variable. This residual decays to some small values and levels out as the iteration progresses. The default globally scaled residual value for convergence of all equations except for the energy equation in Fluent is 10^{-3}. The criterion for the energy equation is 10^{-6}. The computation will stop once all the variable reaches the (ANSYS, Inc., 2010)specified residual value. The set globally scaled residual value was 10^{-6} for all parameters to improve accuracy.

3.5.2.4 **Model Validation**

The model was validated using the experiment by Binder and Kian (Binder & Kian, 1983). The geometry, dimensions, and flow conditions at the inlet for the experiment are in Figure *3.23*. The flow conditions are similar to the case under consideration. Realizable $k - \varepsilon$ and RSM were the models considered. The velocity decay data from the experiment and simulation showed acceptable agreement in the potential core and the early stages of flow development (Figure *3.24*). The discrepancies were apparent towards the outlet but more pronounced in the $k-\varepsilon$ model. Therefore, RSM was adjudged superior to the Realisable $k-\varepsilon$ model.

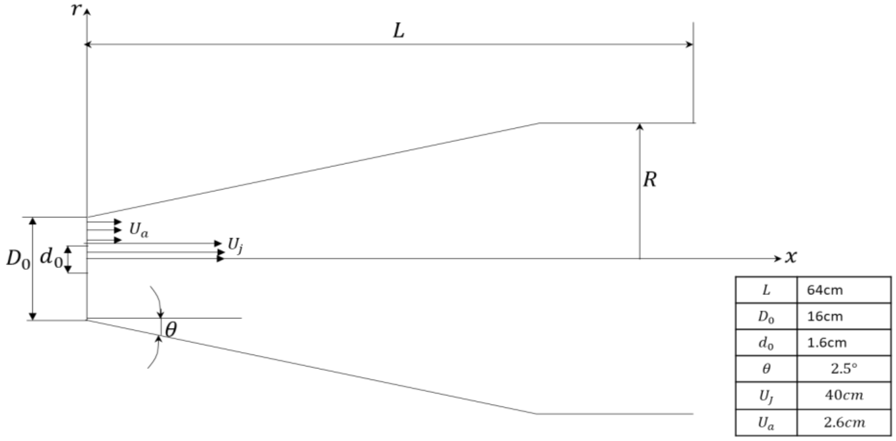

L	64cm
D_0	16cm
d_0	1.6cm
θ	2.5°
U_j	$40cm$
U_a	$2.6cm$

Figure 3.23 Geometry of Binder and Kian experiment *(Binder & Kian, 1983)*

`

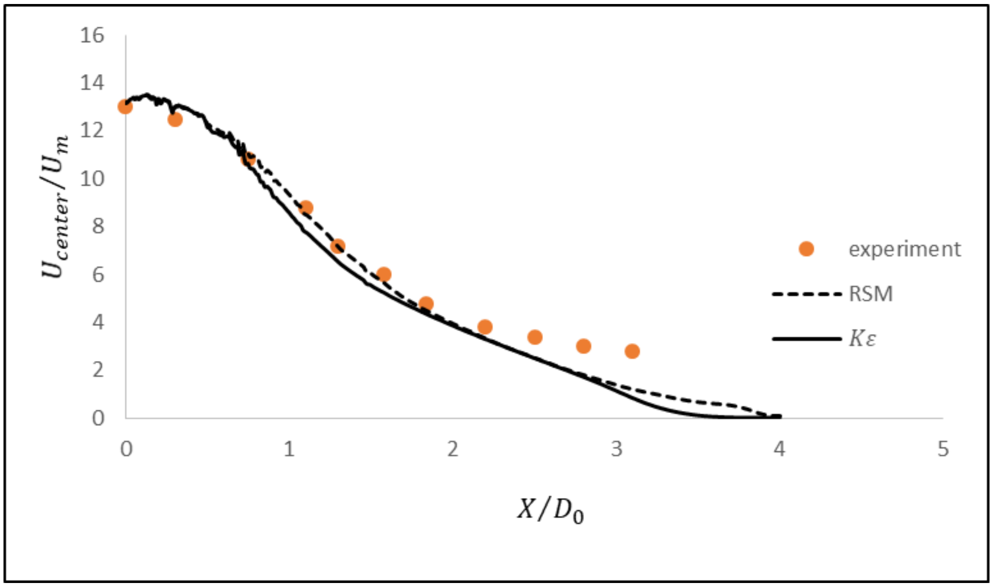

Figure 3.24 Centreline velocity decay from models and experiment

3.5.3 **Outline for The numerical Simulation**

The first simulation was to vary the axial coordinate of the nozzle to investigate the effect on flow behavior and the system performance and to determine the optimum entrainment and mixing position. The flow geometry creation (Figure 3.25) was in the Fluent design modeler with parameters as in Table 3.2

`

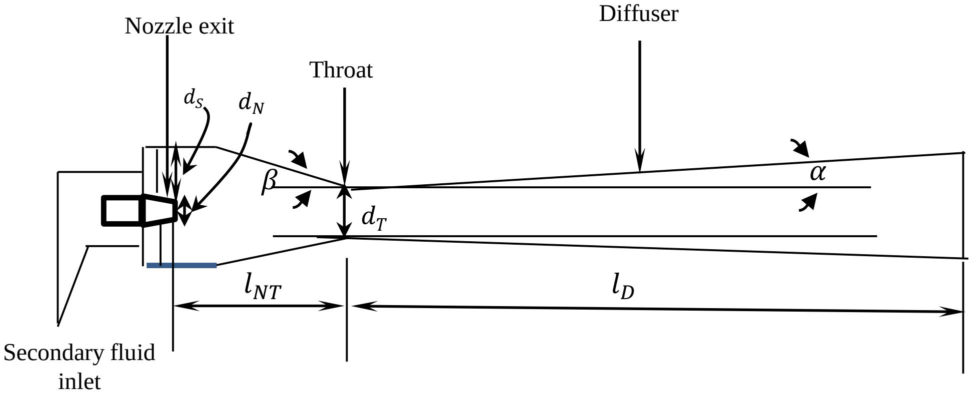

Figure 3.25 The ejector model

Table 3.2 Ejector Parameters

Parameter	Value (mm)
Nozzle diameter (d_N)	5
Suction chamber diameter (d_S)	16
Diffuser length (l_d)	75
Convergence angle (β)	30°
Divergence angle (α)	2°
Nozzle Exit position relative to the throat (l_{TN}) mm	5, 10, 15, 20
Throat diameter (d_T)mm	10

The focus of the second simulation was on the boundary layer modification and alterations in flow characteristics upstream and downstream of the nozzle exit. Tabs enhanced entrainment and mixing in the free jet. A characteristic feature of tabbed flow includes spread angle increase and vortex generation. This, for a wall-bounded flow, will mean early interruption of the flow by the wall and the attendant complexities. Trip rings, on the contrary, reduced spread and suppressed turbulence in the free jet. This implies that the primary/secondary stream interaction will progress well into the tube before reaching the walls. Also, turbulence draws from the mean flow, and high near-stream turbulence will likely reduce the energy needed for entrainment. In this light, the considered modification option was the trip rings.

The schematics of the ring position in the nozzle exit and their dimensions are in Figure 3.26 and Table 3.3, respectively. A reference ejector and three others with 4.9mm, 4.7mm, and 4.5mm rings installed at the trailing edge were the subject of the investigation.

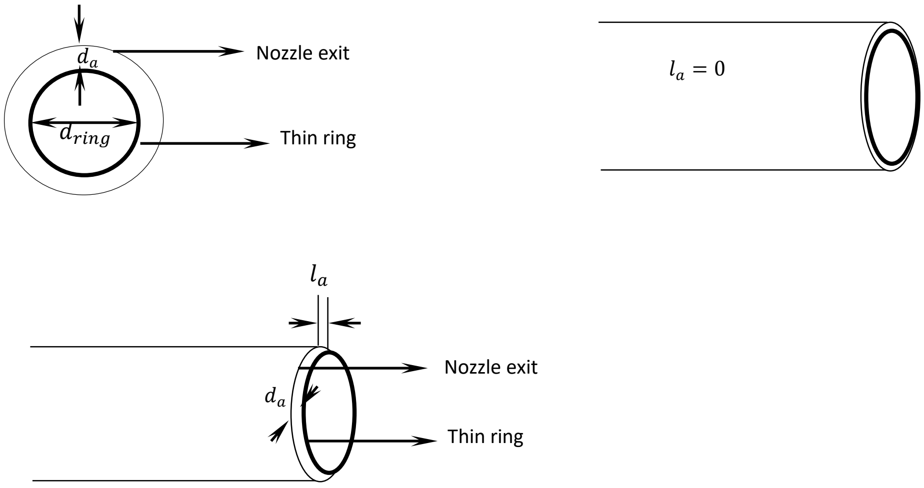

Figure 3.26 Passive ring installation at the nozzle exit

Table 3.3 Ring profile and dimensions

Parameter	**Value (mm)**
The outer diameter of the ring (d_{ring})	4.9, 4.7 and 4.5
Ring thickness	0.5
Annular diameter (d_a)	0.05, 0.15 and 0.25
Axial ring position from nozzle exit (l_a)	0

3.5.4 **Analytical Model Implementation**

The implementation of the models in section 3.2 was with MATLAB. The input arguments were air density (ρ_a), fuel density($\rho_{f,}$)fuel inlet velocity(u_f), and jet angle ($\emptyset$). In Eqn. (3.23), the parameters $u_f, \rho_a, \rho_{f,} and\ \emptyset$ must be known to proceed with the computation. The values of ρ_a at different temperatures are in thermodynamic tables. This requires a linear interpolation function (APPENDIX III) to compute the ρ_a at any temperature within the temperature limits in thermodynamic tables.

The fuel is LPG and comprises propane, butane, and methane in different proportions. The code considered ρ_f as a function of the fuel species proportion. The interpolation function that computes ρ_f at any given temperature is in Appendix III. The algorithm has the individual species proportion and temperature as input and is applicable at temperatures within the limits of those found in the thermodynamics tables.

The simplest form of the natural draft burner in use is the domestic gas stove. The parameters $l\ and\ d$, the length of the mixing tube, and the diameter of the fuel nozzle at the inlet, respectively, were the average design values for this appliance, and the measurement was with vernier calipers.

The spread angle $\emptyset$ estimate was by graphical method (Figure *3.27*). The assumption was that the jet would take the form of the mixing tube and that the adverse pressure, the associated toroidal recirculation, wall effects like friction, and no-slip conditions were negligible.

Figure 3.27 Spread angle determination

u_f is the fuel velocity at the nozzle exit, and the determination was by empirical method. The LPG cylinder had an EBO $-$pressure regulator with a capacity of $1.5\,Kg/h$ max installed. The regulator permits a safe supply of the LPG to the stove.

To empirically determine the mass flow rate of fuel m_f, the flame was stable at the ports and bluish-green, which was an indication of a complete combustion

There was a weighing and recording of the cylinder mass and the LPG content before initiating the combustion process. The combustion progressed until the drop in the mass of the cylinder containing the LPG was measurable. The chart of the consumed mass of vs. the period for nine procedures is in Figure *3.28* The slope of the graph is the average mass flow rate of the fuel ($\dot{m}_f$).

Figure 3.28 Consumed mass of fuel

The computation of fuel velocity u_f was from the Eqn.

$$\dot{m}_f = \rho_f u_f A_f$$

Where $A_f = \pi R^2$ and $R -$ radius of the fuel nozzle.

3.5.5 **Parameters for adiabatic flame temperature computation**

The code neglected the effect of disassociation in lean and stoichiometric mixtures. The computation of combustion products and their quantities in fuel-rich mixtures only factored in the dissociation of CO_2 to $CO\ and\ O_2$ and H_2O to $H_2\ and\ O_2$. Effectively, neglecting the minor species contributions to reduce the complexity of the code.

The function that computes the log of dissociation constant at any given temperature is in Appendix VI. The enthalpy is the product of specific heat and temperature. The script that calculates the specific heat and enthalpy of the reactants and the combustion products at a given temperature are in Appendix X and Appendix IV, respectively. The heat of formation of the fuels and their products at 1 bar and 25℃ are in Table 3.4

`

Table 3.4 The heat of formation of the fuels and their products at 1 bar and 25°C

Substance	Propane	Butane	Methane	CO_2	H_2O	CO	O_2	N_2
Heat of formation$(Kj/Kmol)$	-102900	-126150	-74870	-393520	-241830	-110530	0	0

The computation of the adiabatic temperature started with an initial guess flame temperature of 1300K. The iteration was at an increment of $20K$ until Eqn. (3.73) is satisfied.

3.5.5.1 Flame Speed Parameters

A critical parameter in flame speed computation is the reaction rate $(\mathrm{r_f})$. The calculation was with Eqn. (3.82). While keeping the activation energy E and the reaction orders $\mathrm{n_1}$ and $\mathrm{n_2}$ constant at the values suggested by Westbrook & Dryer (1981), the pre-exponential factor A varied until the determined flame speed in Eqn. (3.91) at atmospheric pressure and stoichiometric condition coincides with the experimental value. Thermal diffusivity λ a variable in Eqn. (3.91) was computed as $\frac{K}{\rho C_p} = \lambda$.

`

CHAPTER 4

4 RESULT AND DISCUSSION

4.1 Results

4.1.1 The nozzle position optimization

4.1.1.1 Velocity distribution at different nozzle coordinate

`

`

`

4.1.1.2 Turbulence analysis at different nozzle coordinate

`

4.1.1.3 Pressure Distribution at Different Nozzle Coordinate

`

4.1.1.4 Mixing and Entrainment at Different Nozzle Coordinate

`

4.1.2 Modification with Passive Rings at the Nozzle Exit

4.1.2.1 Velocity Distribution at Different Ring Diameter

`

Figure 4.1 Velocity distribution in front of the ring ($X/d_N = 0.06$)

Figure 4.2 Evolution of velocity downstream of the trailing edge for an ejector installed with 4.5mm ring

Figure 4.3 Centreline velocity decay

`

4.1.2.2 Turbulence Analysis at Different Ring Diameter

`

4.1.2.3 Pressure Analysis at Different Ring Diameter

Figure 4.4 Pressure contours for (a) The reference ejector and (b) The ejector fitted with 4.9mm ring

Figure 4.5 Relationship between the cross sectional area of the ring and the pressure drop between the nozzle and the throat

4.1.2.4 Entrainment and Mixing at Different Ring Diameter

`

Figure 4.6 O_2 Mass fraction contours

`

`

4.1.3 **Velocity Analysis using the Developed Models**

4.1.3.1 Velocity Analysis at Different Spread Angle

Figure 4.7 Radial velocity profile of jet at RE= 2072 and 10 degrees spread angle

Figure 4.8 Variation in radial velocity profile of jet with spread angle at RE= 2072 and x/d=3

Figure 4.9 Variation in radial velocity profile of jet with spread angle at RE= 2072 and x/d=20

Figure 4.10 Variation in centreline velocity with spread angle at RE= 2072

Figure 4.11 Momentum flux ratio at different spread angle, and $Re = 2072$

`

Figure 4.12 Jet spread at different spread angles

4.1.3.2 Velocity Analysis at Different Density Ratio

Figure 4.13 Velocity profile of jet with different fuel species at x/d=20 and 10 degrees spread

Figure 4.14 Variation in centreline velocity with density at 10 degrees spread

Figure 4.15 momentum flux ratio of fuel species of different density

4.1.3.3 Velocity Analysis at Different Reynolds Number

Figure 4.16 Radial velocity profile at x/d=3 and different Re

Figure 4.17 Radial velocity profile at x/d=20 and different Re

4.1.3.4 Velocity Analysis at Different Air Inlet Temperature

Figure 4.18 Variation in radial velocity profile with preheat temperature at $x/d = 20$

`

Figure 4.19 Variation in centreline velocity with ambient air temperature

Figure 4.20 Axial variation of momentum flux ratio at different temperatures of ambient air

Figure 4.21 variation in decay rate with density ratio

4.1.3.5 Velocity Analysis at Different Port Area

Figure 4.22 Variation in radial velocity profile with port area

Figure 4.23 Variation in centreline velocity decay rate with exit port area

Figure 4.24 Variation in momentum flux ratio with exit port area

4.1.4 Entrainment Analysis using the Developed Model

4.1.4.1 Entrainment Analysis at Different Spread Angle

Figure 4.25 Entrainment at different angle of spread with respect to downstream distance

4.1.4.2 Entrainment Analysis at Different Density Ratio

Figure 4.26 Rate of entrainment downstream of the mixing tube for different fuel species

`

4.1.4.2.1 Entrainment Analysis at Different Air Inlet Temperature

Figure 4.27 Rate of entrainment downstream of the mixing tube at different air temperature with propane as fuel

4.1.4.3 Entrainment Analysis at Different Port Area

Figure 4.28 Variation in the mass of entrained air with port area.

4.1.5 Combustion Analysis using the Flame Equations

4.1.5.1 Primary Aeration Analysis at Different Spread Angle and Fuel

Figure 4.29 variation in primary aeration of propane with respect to port area

Figure 4.30 variation in primary aeration of methane with respect to port area.

Figure 4.31 average velocity of propane/air mixture through the ports

4.1.5.2 Adiabatic Flame Temperature of Propane at Different Equivalence Ratio

Figure 4.32 Comparison of computed adiabatic flame temperature of propane with that from experiment

4.1.5.3 Laminar Flame Speed of Propane at Different Equivalence Ratio

Figure 4.33 Comparison of computed flame speed of propane with that from experiment

`

`

4.1 Discussion

4.1.1 The Nozzle Position Optimisation

The following are the discussion of the results for the nozzle position optimisation. The Re of the flow based on the diameter of the nozzle and velocity at the nozzle exit was ≈ 2960.

4.1.1.1 Velocity Analysis

The mean velocity chart at the nozzle exit ($1mm$ from nozzle exit), the throat($X/d_N = 4$), and the mixer outlet ($X/d_N = 17$) are in **Error! Reference source not found.**. The chart showed a mean velocity gradient between the primary and the secondary streams and between the secondary stream and the solid boundary due to the no-slip condition. There was a consistent streamwise decline in the gradients and an increase in shear layer spread due to entrainment and momentum loss from the primary to the secondary stream.

Error! Reference source not found. and **Error! Reference source not found.** are the velocity contours and the centreline mean velocity chart, respectively. The centreline velocity data indicated a potential core (horizontal portion) and the decay portion. The core length and the decay rate increased with l_{TN}/d_T ratio (**Error! Reference source not found.** and Table 4.1). The end of the potential core, which also marked the beginning of the transition to full-scale turbulence, coincided with the throat, irrespective of the nozzle position. The spread was linear (**Error! Reference source not found.**) and increased with the l_{TN}/d_T ratio following a longer period of primary/secondary stream interaction. This is because the proximity of the nozzle edge and the secondary stream inlet are closer at a high l_{TN}/d_T ratio, as evident in **Error! Reference source not found.**

The flow attained a self-preserving state after $X/d_N = 6$. The self-preserving curve at $7 \geq X/d_N \geq 17$ for $l_{TN}/d_T = 1$ was in **Error! Reference source not found.**. The equation of the curve as a function of the ratio of radial distance R and shear layer width δ was;

`

$$\frac{V_R}{V_{max(x)}} = f(\aleph) \tag{4.1}$$

Where $\aleph = \frac{\mathrm{R}}{\delta}$, V_R is the velocity at radial position R standardized by the maximum velocity at the axial point of interest $V_{\max(x)}$. For $X/d_N \geq 7$, the function $\mathrm{f}(\aleph)$ was independent of distance X in the flow direction, and the estimate was;

$$f(\aleph) = -0.1486\aleph^4 + 0.7416\aleph^3 - 1.2382\aleph^2 + 0.1522\aleph + 0.9968 \tag{4.2}$$

Table 4.1 l_{TN}/d_T ratio and the corresponding potential core length

Potential core length (X/d_N)	1.5	2.5	3.5	4.5
l_{TN}/d_T ratio	0.5	1	1.5	2

4.1.1.2 Turbulence Analysis

The vortex formed at the nozzle exit, which was also amplified by paring when both streams at different velocities came in contact, broke down into small-scale eddies after a short distance from the origin leading to turbulence (Versteeg & Malalasekera, 1995). This distance traversed from the nozzle exit to the throat independent of the nozzle position and was a function of the transition Reynolds number ($Re_{tr} = \Delta u \delta_x / \upsilon$). The Re_{tr} value at the throat for the l_{TN}/d_T ratios considered was ≈ 1000. The length scale (δ_x) is the half-width of the flow or the radial distance from the centreline to the place where the velocity is half the centreline value; the symbol (Δu) is the difference between the centreline and the outer stream velocities and υ is the kinematic viscosity.

`

Turbulence appears as fluctuations in flow properties such as velocity about a mean value and is hence, measured by the r.m.s value of the fluctuating velocity components $(u', v', and\ w')$, which estimates the average magnitude of the velocity fluctuations. **Error! Reference source not found.** shows the plot of the mean velocity (V_R) and the r.m.s data of the fluctuating components standardized by the mean centreline values at $X/d_N = 4$ and $X/d_N = 17$, respectively. The mean velocity values decreased sharply, away from the centre. At the throat (**Error! Reference source not found.**a), the fluctuations were maximum in the shear layers (between the streams and adjacent to the wall) due to high turbulence production and minimum at the centre of the streams where shear and turbulence production was zero. The u' component fluctuated the most, thus highlighting the anisotropic nature of the turbulence.

At the outlet (**Error! Reference source not found.**b), the velocity gradient adjacent to the wall and the associated turbulence production had decreased significantly. Hence the magnitude of the fluctuations was in a downward trend.

The fluctuating velocity component $\left(u^{'}\right)$ at the centreline for the test cases are in **Error! Reference source not found.**. Apparent from **Error! Reference source not found.** is the uniform portion upstream of the throat ($X/d_N \leq 4$), the transition stage ($4 \geq X/d_N \leq 12$), and the evolution to full-scale turbulence ($12 \geq X/d_N \leq 19$). Also shown are $u^{'}$ values at $X/d_N = 4$ and $X/d_N = 17$ in **Error! Reference source not found.**. The graph shows the different stages of turbulence development.

There was a large production of turbulence adjacent to the wall at the throat, and a decline at the outlet (**Error! Reference source not found.**). Also observed was the independence of near-wall turbulence production on the l_{TN}/d_T ratio, particularly far-stream, due to the damping effect and decline in turbulence production. The consequence of l_{TN}/d_T ratio on turbulence production was only significant in the shear region between the streams. At $X/d_N = 4$, this was proportional to the l_{TN}/d_T ratio; but

`

the reverse was the case at $X/d_N = 17$. Therefore for systems with short diffuser lengths ($X/d_N < 15$), the turbulence at the ejector outlet will be higher at high l_{TN}/d_T ratio.

4.1.1.3 Pressure Analysis

4.1.5.4 Pressure Distribution at Different Nozzle Coordinate

`

is the pressure coefficient plot at the centreline for each nozzle position. The pressure decreased to a minimum at $X/d_N \approx 5$ and increased gradually in the diffuser because of the decrease in flow velocity. The pressure difference between the throat and the nozzle exit and the pressure recovery rate in the diffuser increased with the l_{TN}/d_T ratio. However, the minimum pressure value and the point where it occurred were independent nozzle positions.

4.1.1.4 Entrainment and Mixing Performance

The entrainment and the mixing performance were estimated using the magnitude of the mass fraction of air (ma_f) at the centreline and its radial distribution in the system, respectively. **Error! Reference source not found.** shows the ma_f data at $X/d_N = 4$ and $X/d_N = 17$. Also in **Error! Reference source not found.**were the ma_f chart along the centreline.

The primary stream entrained and mixed with the surrounding secondary fluid as the flow advanced downstream, causing the air distribution to decrease at the wall where they were in high concentration and increase at the centre where the concentration was low. At $X/d_N = 4$, the mixing process progressed at different rates, as indicated by the values of ma_f at the walls and the centre of the stream (**Error! Reference source not found.**). There was also measurable progress in the mixing values for l_{TN}/d_T ratios 2 and 1.5 due to early start of the mixing and entrainment processes because of the proximity of the nozzle exit to the air or secondary stream inlet. The processes, however, had barely begun for ratios 1 and 0.5 because of the lag. At $X/d_N = 17$ (**Error! Reference source not found.**), the mixing had advanced considerably, and the curve was about flat, with $l_{TN}/d_T = 2$ giving the best performance. **Error! Reference source not found.** shows the growth of ma_f along the centerline. The ma_f and r.m.s velocity curve in **Error! Reference source not found.**; showed that they correlate very strongly, thus highlighting the principal role of turbulent eddies in the entrainment of air and its mixing with the primary stream.

`

4.1.2 Modification with Passive Rings at the Nozzle Exit

4.1.2.1 Velocity Analysis

The study of the mean velocity distribution in the flow was at $Re = 2.14e^{03}$. The premise for the Re computation was the mean flow velocity at the nozzle exit and the diameter of the nozzle. The chart of the mean velocity data normalized by the local centreline values at the nozzle exit ($X/d_N = 0.06$), the throat $(X/d_N = 4)$, and the ejector outlet $(X/d_N = 17)$ for the reference ejector and the ejector modified with 4.5mm diameter ring is in **Error! Reference source not found.**. The width of the shear layer increased progressively in the streamwise direction but more slowly and independent of the ring diameter when the ring was attached (**Error! Reference source not found.**). The reduced spread was because of the interaction of the wake downstream of the ring with the streamwise vortices, both of which are of the opposite sign. The wake-vortex interaction caused an early breakdown of the vortical structure and suppression of the shear layer growth. This prognosis was evident in the power density spectra deconstructions by Sadeghia and Pollard (2012). The free jet modified with rings showed near-stream coherent structure suppression and turbulence reduction.

The velocity distribution in the wake was rather complex (Figure 4.1). The changes in the near-stream flow dynamics due to wake formation were local and did not extend beyond a third of the nozzle diameter from the origin (Figure 4.2). The wake decayed swiftly in the flow direction and faded completely at $X/d_N = 0.3$.

The centreline velocity chart has a horizontal portion known as the potential core and a decaying part marked by rapid mixing and entrainment (Figure 4.3). There was a spike in the nozzle exit velocity due to cross-sectional area reduction when the ring was attached. Also, the potential core length grew to $4.8d_N$ from $4.2d_N$ in the reference. The breakdown of the coherent structure and the production of replete

`

small-scale eddies happened at the end of the potential core. This process initiated the transition to full-scale turbulence. The decay process was slower with the ring due to the rise in nozzle exit velocity and the suppression of the streamwise vortices independent of its diameter.

4.1.2.2 Turbulence Analysis

The jet from the nozzle thrust and made contact with the secondary stream. Because the layers of the fluid streams in touch are at different velocities, what followed was the Kelvin-Helmholtz instability that prompted the streamwise vortices. The vortices broke down to small-scale eddies a short distance from the origin and caused turbulence or random fluctuation of the flow variables. The root mean squared (r.m.s) data $(u', v', and\ w')$ gave the turbulence estimate or the magnitude of the fluctuating velocity component. Other statistical descriptors of turbulence in literature include variance, turbulent kinetic energy, and turbulent intensity. The r.m.s data $u'\ at\ X/d_N = 0.06$, $X/d_N = 4$, and $X/d_N = 17$ are in **Error! Reference source not found.**. Also in **Error! Reference source not found.** is the chart of u' at the centerline.

The magnitude of u' was highest in the shear layers because of turbulence production associated with sheared mean flows and least at the jet centre where there is no shear and turbulence production (**Error! Reference source not found.**a and **Error! Reference source not found.**b). The fluctuation at the centre was high, given the negligible turbulence production. The significant centerline turbulence was due to the transport of turbulent eddies from the adjacent shear region across the boundary.

At the throat (**Error! Reference source not found.**b), the increase in fluctuation close to the wall was independent of the ring or its diameter because of the no-slip condition. At $\mathrm{X/d_N} = 17$ (**Error! Reference source not found.**c), the trend for the near-wall turbulence was downward because of the degeneration of the shear forces responsible for turbulence production. The reason for this was the decay of the mean velocity gradient far stream (**Error! Reference source not found.**b).

`

The near-stream turbulence suppression varied inversely with the ring diameter (**Error! Reference source not found.**). The magnitude of fluctuation in the reference ejector peaked at $\mathrm{X/d_N} = 17$ and remained steady. For modified ejectors, the differences in their magnitude of fluctuation were negligible at the outlet. It, however, continued to increase beyond $X/d_N = 17$. Therefore, for systems with $X/d_N \leq 15$, the reference ejector will perform better per turbulence production, while for units with $X/d_N \geq 17$, modification with a ring would be adequate.

The mean velocity and the turbulence distribution chart are in (**Error! Reference source not found.**). The inequality of the fluctuating components was apparent and underscored the anisotropic nature of turbulence. The component $\mathrm{u'}$ fluctuated the most (Versteeg & Malalasekera, 1995). At the throat (**Error! Reference source not found.**a), the mean velocity gradient adjacent to the wall was large and guaranteed steady turbulence production. This turbulence production, however, reduced significantly and approach isotropy with the shear layer spread and mean velocity gradient decay in the diffuser (**Error! Reference source not found.**b).

4.1.2.3 Pressure Analysis

The centreline pressure coefficient for the reference ejector and those with concentric rings at the trailing edge of the nozzle is in **Error! Reference source not found.**. Also in Figure 4.4 are the pressure contours for the reference and the ejector modified with a 4.9mm ring. The presence of the ring obstructed the flow and reduced the cross-sectional area of the nozzle at the exit. Just upstream of the ring is the stagnation region, which showed a significant increase in pressure. Downstream of the ring, the flow expanded with a corresponding pressure drop. Overall, the modification with the ring increased the pressure difference between the nozzle exit and the throat. The relationship between the ring diameters or cross-sectional area and this pressure difference was linear (Figure 4.5).

`

4.1.2.4 Entrainment and Mixing

The secondary stream entrainment estimate was by the mass fraction of air ($\mathrm{m_{af}}$) at the centreline. The degree of mixing evaluation was by the radial distribution of the $\mathrm{m_{af}}$ near stream ($\mathrm{X/d_N} = 4$) and far stream($\mathrm{X/d_N} = 17$). Concerning the entrainment chart (**Error! Reference source not found.**), the modification with a 4.9mm diameter ring gave the best performance. The $\mathrm{m_{af}}$ value increased from 0.47 in the outlet of the reference ejector to 0.56 in the model with a 4.9mm ring. This increase was about 19.15%. The O2 mass fraction contours in Figure 4.6 showed pictorial evidence of the reduction in the width of the shear layer when modified with the ring and its dependence on the ring diameter. Because the near-stream shear layer spread was higher in the reference ejector, the development advanced to the ejector wall at a shorter distance downstream of the throat ($\mathrm{X/d_N} \approx 7$) than the modified ones. This interruption at the wall occurred at $\mathrm{X/d_N} \approx 11$ in the ejector with a 4.9mm ring installed. The entrainment values were higher near-stream of the reference ejector because of the increased spread but peaked at $\mathrm{X/d_N} \approx 15$ because of the early obstruction.

The graph of the trailing edge-to-throat pressure differential as a function of entrainment data at the outlet shown in **Error! Reference source not found.** was linear. The linear profile was relatable because an increase in the pressure difference between the trailing edge of the nozzle and the throat will typically increase the mass flux of the secondary stream in the ejector. The plot in **Error! Reference source not found.** also showed that the turbulence fluctuation accounted for over 96% variability in the entrained mass of air. Hence, the entrainment value was a function of spread, the pressure differential between the nozzle exit and the throat, and turbulence growth in the unit.

In **Error! Reference source not found.**, at $\mathrm{X/d_N} = 4$, the $\mathrm{m_{af}}$ gradient was 1.33 for the reference and 3.17 for others, irrespective of the ring diameter. Going by these, the ring diameter had little effect on mixing. The lower gradient of the reference ejector indicated a better near-stream mixing performance. This edge

`

was because the turbulence responsible for mixing, was suppressed near-stream when the ring was present. At $X/d_N = 17$ (**Error! Reference source not found.**), the curves were flat and parallel. Hence, the mixing performance at the outlet was near perfect and independent of the ring diameter. Their incongruence followed the improvement in entrainment values with ring diameter.

4.1.3 Flow Analysis using the Developed Models

Three features of the flow along the ejector as investigated using 1D model and how they are affected by spread angle, fuel specie, air temperature at inlet and area of the burner ports would be presented and discussed. The features in other in which they were discussed are velocity decay, air entrainment and pressure drop.

4.1.3.1 Velocity Analysis at Different Spread Angle

Increase in the flow spread angle has been achieved using tabs with delta tabs being the most effective (Zaman, Reeder, & Samimy, 1994). While passive rings placed at nozzle exit has been used to suppress same (Parker, Rajagopalan, & Antonia, Control of an Axisymetric Jet Using a Passive Ring, 2001) and (Sadeghi & Pollard, 2012) . The jet spread angle estimated using the method described in section 3.5.4 was $\approx 11°$. The angles considered in the study of the effect of spread angle on centerline velocity decay were 10, 11 and 12 degrees, respectively.

The radial velocity profile at different axial positions when gas (propane) at 10 degrees spread angle and 300K and air preheated to 400K flows through the mixing tube is shown in Figure 4.7. The vertical scale $(u_r)$was normalized by the mean jet velocity at nozzle exit u_f while the horizontal scale (x) was normalized by the nozzle diameter d . From the plot, centerline velocity decays with axial distance. The decay process can be evaluated or quantified using some parameters such as decay rate, momentum flux ratio and spread rate. Although not directly related to mixing, centreline velocity decay in a good number

`

of cases gives a clue as per the extent of mixing that has taken place in the system. Exception being in cases where the flow vectors considerably or bifurcations. A good example of this is the rapid decay of centreline velocity due to bifurcation when two delta tabs where placed $180°$ apart (Zaman, Reeder, & Samimy, 1994).

Similar profile as in Figure 4.7 was obtained even though with different decay and spread rates when the spread angle was varied to 11 and 12 degrees respectively while keeping the mass flow rate constant. From Figure 4.8 and Figure 4.9 which are the plots of the variation in radial velocity profile with spread angle at $x/d = 3$ and at $x/d = 20$ respectively, it is obvious that the center line velocity decay rate is faster with respect to axial distance when the spread angle is increased.

Referring to Figure 4.8, the ratio of radial to jet velocity $\left(u_r/u_f\right)$ at the center of the jet is approximately one at 10 degrees spread and at the given axial distance and less at higher spread angles (11 and 12 degrees respectively). The axial location where $u_r/u_f = 1$ coincides with the nozzle exit therefore at 10 degrees spread, the distance from the virtual origin to the leading edge of the nozzle is very close to $x/d = 3$ and somewhat less at higher spread angles.

I. Decay Rate

The plot of inverse decay of centreline velocity with axial distance (Figure 4.10), gives a more accurate representation of variation in distance from virtual origin to the nozzle exit with angle of spread as well as centreline velocity decay with respect to axial distance. The plot showed that, velocity decay traced a linear part which agrees with the experiment by Pope (2000) and Hussein, Capp, & George (1994) in self similar or fully developed region. Similar experiment by Subramanian, et al. (2018) and Liepmann & Gharib (1992) showed that in the period leading to full transition of the flow, upto $x/d \approx 4$, u_f/u_{max} remained constant before increasing linearly. However on a general note, the decay of centreline velocity is usually modelled using a linear function. At the nozzle exit, $u_f/u_{max} = 1$ hence the distance between the origin

`

and the point in x axis corresponding $u_f/u_{max} = 1$ (Figure 4.10), gives length of the virtual origin which from the graph ranged between $2.5\ to\ \approx 3.0$ depending on the spread. It is evident that the distance from the virtual origin to the leading edge of the nozzle decreased with spread angle. The inverse of the slope gives the decay constant and considering that the centreline velocity u_{max} is at the denominator in the vertical axis, it then follows that the lower the decay constant, the higher the decay rate. The decay constant at 10, 11 and 12 degrees spread respectively 5.5, 4.9 and 4.5. Some values of decay constant and virtual origin obtained by other researchers are presented in Table 4.2

Table 4.2 Values of decay constant and virtual origin by other researchers

Reference	Parameter	Value in reference	Present work
Decay constant	(Hussein, Capp, & George, 1994)	5	$5.5 - 4.5$
	(Gazzah, Boughattas, Belmabrouk, & Said, 2010)	5.025	
	(Subramanian, et al., 2018)	6.12	
Virtual origin	(Hussein, Capp, & George, 1994)	2.7	2.4-3.0
	(Subramanian, et al., 2018)	4	
	(Pope, 2000)	2.8	

`

II. Momentum Flux Ratio

Considering that momentum is conserved in the system, it follows that the momentum loss by the jet is proportional to that gained by the entrained air. High entrainment velocity would mean an increase in centreline velocity decay rate or mixing activity. Hence the momentum flux ratio of the entrained fluid to main jet at given axial position could be used as a measure of mixing activity or decay at that point. The higher the momentum flux ratio the greater the decay. From the plot of momentum flux ratio at different axial position and angle of spread (Figure 4.11), the decay process is highest at the nozzle exit and decreases as the flow progressed downstream toward the end of the mixing tube. Also from the plot, centreline velocity decay increased with spread angle starting from the leading edge of the nozzle up to $x/d \approx 10$ the.

III. Jet Spread

To characterize the jet spread, the velocity half width $r_{0.5}$ defined as radial distance from the jet axis to the point where the velocity is 0.5 times the centerline velocity was used. Both the vertical and the horizontal axis were normalized with d- the nozzle diameter(Figure 4.12).The slope of the graph gives the jet spread rate. The jet spread rate at 10, 11 and 12 degrees respectively were 0.104, 0.117 and 0.121. As expected the higher the spread angle the higher the spread rate.

Evidently, increasing the angle of spread will reduce the distance between the leading edge of the nozzle and the virtual origin causing the velocity decay process to start early. Also, the momentum flux ratio as well as spread rate is increased culminating into an increase in the rate at which the centreline velocity decays with axial distance.

`

4.1.3.2 Velocity Analysis at Different Density Ratio

Density ratio is the ratio of air to fuel density (ρ_{air}/ρ_{fuel}) at the nozzle exit. The value therefore depends on the fuel specie involved and the temperature of the fuel/air. Effect of density ratio on centreline velocity decay would be considered in two parts- first would be variation of the ratio with fuel species while the second would the variation of the ratio with air temperature.

I. Density of Fuel Species

Just as with the analysis that was carried out using propane at different spread angles, the initial temperatures of fuel and air were maintained at 300K and 400K respectively. The analysis was carried out assuming $10°$ spread and constant mass flow rate ($6.6667\mathrm{e}-05\mathrm{kg/s}$) regardless of the fuel specie. The velocity ratio ($u_{entrainment}/u_f$) at $10°$ spread were 0.0879, 0.0879 and 0.0876 for propane, butane and methane respectively. The variation in velocity ratio is insignificant and therefore can be considered as constant.

The density ratio for propane, butane and methane respectively were 0.2916, 0.2182 and 0.8126. The higher the ratio, the faster the decay (Figure 4.13) and (Figure 4.14). From Figure 4.14 following the same order, the decay constant at 10 degrees spread were 5.5, 6.1 and 3.1 and also as expected, the momentum flux ratio (Figure 4.15) followed the same trend.

Keeping the mass flow constant and using fuels of varying densities also means that Re is different for each of the flow process. For example the Re for flow processes involving propane, butane and methane respectively were 2.0727e+03, 2.2735e+03 and 1.5250e+03. To be sure that the variation observed in Figure 4.13 and Figure 4.14 are fully accounted for by differences in density ratio, the computation was made for the gases at different Re. The Re which was based on jet exit diameter and velocity and was varied by increasing\reducing the mass flow rate ($6.6667\mathrm{e}-05\mathrm{kg/s}$) by a factor of 1.5 and 0.5 respectively. The radial velocity profile for propane at different Re and $x/d = 3\ and\ x/d = 20$

`

respectively are shown in Figure 4.15 and Figure 4.16. The Re were 2.0727e+03, 3.1090e+03 and 1.0363e+03 and the result showed an overlap in decay pattern of the flow.

II. Air Inlet Temperature

Atmospheric temperature varies so also the air temperature. A rise in air temperature will bring about an increase in the initial temperature of combustible mixtures which causes some measure of increase in the adiabatic flame temperature. To increase the flame temperature or meet some other performance criteria, it is common to preheat the air prior to entrainment. One of the consequences of this preheating is the reduction in density of the entrained air which in turn will affect the velocity decay/momentum transfer process in the mixing tube. The density ratio at nozzle exit, for propane at 300k and air preheated to 300K, 350K and 400K respectively would be 0.3434, 0.3175 and 0.2916. From Figure 4.18, just as with the analysis involving fuel species of different densities, the decay process with the decay constants of 5, 5.2 and 5.5 at 300K 350K and 400K respectively proceeds faster with increase in density ratio. Similarly, the momentum flux ratio is higher when the entrained air temperature is lower (Figure 4.20). One of the things of note so far is the use of momentum flux ratio in determining the extent of mixing or centreline velocity decay rate. Higher flux ratio will always lead to better mixing enhancement or decay rate.

The values of decay constant was plotted against density ratio in Figure 4.21. Generally, the decay rate would increase with density ratio. Hence any change in the system that causes a significant variation of density ratio from the design values will alter the performance of the system.

From Figure 4.13 and Figure 4.14, and Figure 4.18, Figure 4.19 and Figure 4.21 it is obvious that compared to change in ambient or preheat temperature, the mixing process will be affected much more if the fuel for which a system was designed for is changed especially when the density difference is significant. As a matter of fact the preheat temperature may be varied with minimal effect on the performance but that

`

cannot be said of fuels when there is a significant change in density without altering the design of the combustion unit.

4.1.3.3 Velocity Analysis at Different Exit Port Area

So far the discussion has progressed with the assumption that the port area at the exit of the burner is the same with the cross-sectional area at the end of the mixing tube. However, this may be varied to achieve some design objective. The variation in radial velocity profile of the jet with exit port area at $x/d = 20$ is shown in Figure 4.22. Also plotted were the inverse of centerline velocity normalized by the value of the average velocity at the exit of the nozzle u_f and momentum flux ratio in axial direction (Figure 4.23 and Figure 4.24). The plots showed that the effect of port area in the mixing or centerline decay process is rather insignificant. In Figure 4.24, the exit port area A_{port} was normalized by A_{max} the maximum cross-sectional area of the mixing tube which corresponds to the area at the end of the tube.

4.1.4 Air Entrainment Analysis using the Developed Model

The stability and the efficiency of the combustion unit will depend to a great extent on the amount of primary air entrained. Insufficient air entrainment can lead incomplete combustion while excess air is associated with stability issues such as to flash back, flame lift and blow off. The momentum/velocity difference between the ambient fluid and high speed is resposible for air entrainment. The momentum difference causes shear and subsequent Kelvin-Helmholtz instability which produces two types of structures the 2D vortical Structures and 3D counter rotating streamwise structure (Nastase, Meslem, & Gervals, 2008) and (Liepmann & Gharib, 1992). Entrainment process is primarily contolled by the streamwise vortices which evolve and develop in the braid region between two primary vortical structures (Liepmann & Gharib, 1992). Therefore, the amount of fluid entrained will depend on both the strength and persistence of the streamwise structure. The initial instability/shear which produce these structures is due to velocity difference between the fluid streams and these structures can only be sustained if this

`

velocity difference is sustained. However, for jet flow, velocity begins to decay towards the end of the potential core causing a decrease in velocity difference between the ambient fluid and the jet thus attenuating the shear that surports the vortical structure.

Entrainment is defined in Eqn (2.30) and Eqn(2.33) as the spatial derivative of the volume flux i.e. dQ/dx (Liepmann & Gharib, 1992) or mass per unit length entrained by the flow (ρ_{air} (dQ/dx)) (Hussein, Capp, & George, 1994). How this parameter will vary with changes in spread angle, density ratio and exit port area and the mechanism that trigers the changes would be discussed in the following.

4.1.4.1 Air Entrainment Analysis at Different Spread Angle

Variation in entrainment mass as a function of downstream distance is shown in Figure 4.25. the vertical axis, was normalised using d/m_{fuel} while the horizontal axis was normalised using d the diameter of the nozzle. The rate of entrainment increased from zero at the nozzle exit and approaches a constant value as the flow progressed downstream. The experiment by Liepmann & Gharib (1992) and Nastase, Meslem, & Gervals (2008) sugests similar pattern. Also more fluid is entrained when the angle of spread is increased.

For a given mass flow rate, fuel specie and leading edge diameter of the fuel nozzle, an increase in the angle of spread will be due to the nature of K-H instability introduced at the leading edge of the nozzle. When the instability is such that streamwise vortices are added to the velocity field, the angle of spread will increase. The vissible effect of this is identation of the jet core.

The side view of LIF images of jet (Figure 2.3), showed that secondary instabilities that emerge from the braid region is attached to the main flow and stretches round the primary vortex upstream. This secondary structure are always attached to the main flow and stretches outward (Liepmann & Gharib, 1992). The stretching of the secondary structure will determine the identation that would be made on the core. In between the stretched secondary structure is the ambient fluid. The more the stretch or spread

`

the more the indentation and the ambient fluid that will be entrained as the secondary structure move radially in and out with passage of the vortex ring.

The density ratio is constant (0.2916) while the ratio of entrainment to average velocity at the nozzle exit $(u_{entrainment}/u_f)$ are 0.0879, 0.0925 and 0.0966 at 10, 11and 12 degree spread respectively. This actually indicates higher values of entraiment velocity relative to the average velocity of fuel when the spread is increased. The higher the value $(u_{entrainment}/u_f)$ the more the entrainment.

4.1.4.2 Air Entrainment at Different Density Ratio

Mass per unit length entrained by the flow downstream of the tube was plotted as shown in Figure 4.26. The density ratio ρ_{air}/ρ_{fuel}, for propane, butane and methane respectively were 0.2916, 0.2182 and 0.8126. The rate at which air is entrained increased from the nozzle exit and approached a constant value downstream of the tube. For a given density of air, entrainment rate would be higher when the fuel is less dense. Similar trend was observed in Figure 4.27 when the air temperature was varied from 300K to 400K. The density ratios here were 0.3434, 0.3175 and 0.2916 at 300K, 350K and 400K respectively. This agrees with the result from experiment by Dimotakis (1991) and Brown & Roshko (1974) which showed that shear layer growth increased with density ratio.

4.1.4.3 Air Entrainment at Different Exit Port Area

The effect of exit port area on mass of entrained air was plotted in Figure 4.28. The total port area plotted in x axis was normalized by the cross-sectional area of the mixing tube exit. While the total mass of entrained air i.e. The mass fraction of air flowing from the ports per time was normalized by that of fuel. The mass of entrained air increased with port area.

The total amount of air required for complete combustion consists of entrained primary air and secondary air and can easily be computed from chemical equation if the gas composition is known. This is so because secondary air must always get to the flame through the space between the burner and the heated object

`

even though not all of it may be involved in the reaction process. Therefore when the entrained air is much, in addition to susceptibility to stability issues associated with it, the percentage of secondary air that are not involved in the reaction process is rather high and they end up carrying away heat thereby reducing efficiency. On the other hand if the entrained air is small, then secondary air supply may not be sufficient or be able to get to the flame on time to achieve mixing at a molecular level with the gas to take part in the reaction causing an incomplete combustion. For optimum performance, a balance is necessary between the primary and secondary air supply.

Since the primary air will most likely take part in the combustion reaction considering the time available for mixing. Increasing the primary air by say an amount x will mean that the secondary air requirement will reduce by more than x. From Figure 4.28 primary air entrainment can be increased by increasing the port area. This is usually achieved by designing the unit to consist of very numerous small sized ports so that the overall area is increased.

Another method of increasing air entrainment as discussed in section 4.1.4.1 is by increasing the angle of spread which also can be achieved by placing tabs at the leading edge of the gas nozzle. This though would require an increase in the dimension of the mixing tube to accommodate the spread.

The stability issues can be improved upon by the design of the ports. Lifting or blow off would be prevented by increasing the port size or reducing the flow velocity while the reverse would be the case when the system is prone to flash back.

From the discussion in section 0, if a fuel other than that for which a combustion unit was designed for is to be used in the unit, two things are obvious; if a lighter gas is to be used their will be issues with stability because more primary air than necessary would be entrained while for denser gases the combustion may not likely proceed to completion because of insufficient air entrainment. Going by the plot of Figure 4.28 adjusting the area of port will help adapt the unit to the new fuel. If the new fuel is denser than the default

`

fuel, the total area of ports should be increased and should be reduced if it is lighter. In the dealing with stability issues which is a function of flow velocity the size of the ports can be reduced to prevent flash back or increased to prevent lifting

4.1.5 Combustion Analysis using the Flame Equations

Primary air entrainment and how it is affected by jet spread, density ratio and exit port area was investigated using flame models. Considering the fact that the ultimate goal is to achieve a stable and efficient combustion unit, this will be discussed further with stoichiometric air/fuel requirement in view. To this end the parameter- primary aeration defined as the ratio of entrained air/fuel ratio to stoichiometric air/fuel ratio (Brandon, 2019) will be used.

$$primary\ aeration = \left(\frac{entrained\,\frac{air}{fue}\,ratio}{stoichiometric\,\frac{air}{fuel}\ ratio}\right) * 100$$

4.1.5.1 Variation in Primary Aeration at Different Port Area and Fuel Specie

The plots of the variation in primary aeration with respect to port area normalized by the area of the tube at exit for propane and methane gases were plotted respectively in Figure 4.29 and Figure 4.30. From both figures, primary aeration increased with port area. However the rate of increase varied with gas specie and the angle of spread. In Figure 4.29, at $A_{port}/A_{tube} = 3$ the values of primary aeration for propane at 10, 11 and 12 degrees spread respectively were 38, 43 and 47, whereas for methane (Figure 4.30) the values were 59, 65 and 72 at the same A_{port}/A_{tube} value and angle of spread. For burners using natural gas at standard pressure, the primary aeration ranged between 30 to 60% at design capacity (Selas, 2021) and (Brandon, 2019).

`

Whereas primary aeration increased with port area, the extent to which these parameters can be varied will depend on the stable operation of the burner, the flammability limits of the fuel, the desired dimension of the flame and perhaps the space available for the burner layout

For stable operation, the flow velocity of air/fuel mixture through the burner ports must be within a range usually fixed by the laminar burning velocity of the mixture. As the port area is increased and more primary air entrained, the average flow velocity of the mixture through the ports decreases as shown in Figure 4.31. The flow velocity computed as Q/A_{port} was normalized by the maximum laminar burning velocity of the fuel. Where Q is the volumetric flow of the air/fuel mixture through the port of cross-sectional area A_{port} and given in Eqn. (3.36). If the flow velocity is considerably higher than the burning velocity of the mixture, flame lift will occur and when it is significantly low relative to the burning velocity of the mixture, the flame front will move very close to the burner with consequent increase in temperature and wear rate and in extreme cases propagates into the burner a phenomena known as flash back.

4.1.5.2 Adiabatic Flame Temperature and Laminar Flame Speed

Laminar flame speed which is a function of reaction rate and flame temperature varies with mixture strength or equivalence ratio with maximum at equivalence ratio close to 1. This understanding can also be employed both in regulating the flame velocity/stability and addressing safety concerns such as flash back. The further away the mixture strength is from stoichiometric value the lower flame velocity and the chances of flash back. The computed values of the adiabatic flame temperature and laminar flame speed of propane was plotted against equivalent ratios in Figure 4.32 and Figure 4.33 respectively. The deviations in the computed values with respect to those measured from experiment is quite obvious especially in the rich spectrum of the divide. This however is due to the simplifications adopted in the computation process. The result may be considered acceptable or reasonably accurate especially in the light of the ease they offer.

`

Another way of mitigating against flash back is the choice of port size. Flame propagation within a tube is affected by two phenomena- heat loss from the flame to the tube walls and destruction of active radicals as they collide. As the size of the tube is reduced, surface area to volume ratio within the tube is increased (Irvin & Richard, 2008). Consequently, the volumetric heat loss will increase as well as frequency of collision and the rate of destruction of active radicals. The size of the tube in which this increase volumetric heat loss and radical quenching will not permit the propagation of the flame within it is known as quenching distance. Therefore if the diameter of the individual ports are drilled to coincide with the quenching distance then flame flash back will as well be prevented.

Another limiting factor to the volume of air that can be entrained is the flammability limit of the fuel which is the mixture composition or concentration beyond which the flame propagation cannot be sustained once the ignition source is removed and it occurs both in the rich and lean concentration spectrum. If the rate and heat of reaction of the fuel oxidizer mixture is such that the rate of external heat loss by the flame is higher than the rate of heat generation the flame will not be self-supported. However this limit can be broadened with increase in temperature of the reacting species.

Flame dimension (size and shape) affects the efficiency of heat transfer to the process load and can be controlled by combined effect of primary aeration, port number, size and orientation For a steady oblique flame front, stabilized at the ports for example, the laminar flame speed can be related to the flow velocity of the unburnt mixture using Eqn. (3.92) i.e. $S_L = S_u \sin\alpha$. If S_u the flow velocity of the unburnt mixture is increased, then the cone angle of the flame α will reduce to keep the flame stabilized at the ports. The implication of this will be an increase in flame height which may or may not help for efficient transfer of heat to the process load depending on the extent to which the flame is exposed to the atmosphere. If the design of the combustion chamber, with respect to the size and shape of the process load is compact the

`

elongation will help for more efficient transfer of heat however if it is such that the flame front is over exposed to the atmosphere, a substantial amount of heat will be lost.

`

CHAPTER 5

5 CONCLUSION AND RECOMMENDATIONS

5.1 Conclusion

This study investigated the changes in flow behaviour in ejectors for natural draft burner with nozzle exit at different axial coordinates (l_{TN}/d_T ratio). The flow was described by velocity, pressure, turbulence, entrainment, and mixing data. The data analysis was at the centreline, the throat ($X/d_N = 4$), and the outlet($X/d_N = 17$). The velocity profile at the throat showed two gradients or shear layers between the streams and adjacent to the wall, respectively. As the flow evolved, the shear layer width increased, and the gradients reduced due to the entrainment of the outer stream and momentum exchange. The shear layer spread and the velocity decay rates were proportional to l_{TN}/d_T ratio.

Turbulence was estimated using the r.m.s values of the fluctuating velocity. The turbulence production at the throat was significantly high in the shear layers and low at the centre. However, adjacent to the wall, at $X/d_N = 17$, the gradient reduced significantly, and the turbulence production was low and trending downward.

The entrainment and mixing performance description was by the magnitude of the mass fraction of air (ma_f) at the centerline and its radial distribution in the system, respectively. As the flow advanced, the air concentration decreased at the wall and increased at the centre where the concentration was low. The mixing process had evolved significantly at the ejector outlet, and the curve was almost flat. However, the mixing and the entrainment process lagged behind when the nozzle was positioned closer to the throat or at low l_{TN}/d_T values.

`

In ejectors, the in-flow conditions can change the flow dynamics, not just near-stream but also far-stream, and affect system performance. In this study, the in-flow conditions were disrupted by placing thin circular rings of 4.9mm, 4.7mm, and 4.5mm diameters at the trailing edge of the nozzle.

There was a suppression of turbulent activities and shear-layer growth near-stream when the wake that formed downstream of the ring interacted with the streamwise vortices.

The outcome was a reduced centreline decay rate, low entrainment values, and delayed mixing from the origin to $X/d_N = 15$.

Because of the reduced shear layer spread, the entrainment process went far in the diffuser before interruption by the ejector wall. Therefore, the entrainment and turbulence increase was gradual but consistent and well beyond the values in the reference ejector at $X/d_N > 16$.

The entrainment values improved in the modified ejector, but the mixing data at the outlet was independent of the ring. Also, the nozzle exit/ throat pressure differential was proportional to the ring diameter due to stagnation and pressure increase upstream of the ring and suction at the throat.

5.2 Recommendations

In the design of the ejector unit, the initial flow conditions must support near-stream turbulence suppression. This is because the turbulence draws from the mean flow and reduces the energy for entrainment. The near stream turbulence suppression in this work was by rings installed at the trailing edge of the nozzle, and the performance improvement was significant. Therefore, it is crucial to consider another passive device like mesh and rings with different cross-section geometry installed at different positions from the shear layer to the jet core.

`

The closure models considered were the Realizable ke and the RS models. The near wall flow modeling was with standard wall function. However, getting the cell centroid adjacent to the wall to conform to (30<Y+<300) was tedious.

kw sst models, in contrast, come with automatic wall treatment, and the mesh requirement is the same even for near-wall or low-Re investigations. Kw sst performs well for wall-bounded flows. Therefore, the model performance assessment alongside the Realizable ke and RS model is pivotal.

The mesh in this work was unstructured. The ease of generation and the stability of the computation process informed this choice. A structured mesh, though more demanding to generate, can achieve accurate results with smaller mesh size and lower run time and should be considered.

One of the assumptions during the development of the analytical models was a negligible wall effect. Though the model correctly captured the flow structure at the jet's core, it did not account for the shear due to no-slip conditions at the wall. The recommendation is a correction term addition to the model to account for the wall effect.

The CFD investigations should also include combustion analysis for clarity and a broader understanding.

5.3 Contribution to Knowledge

The model implementation was with a code written in MATLAB. The code provided with the required input at the prompt can carry out a parametric study of the jet flow and combustion analysis. The implication is that further investigation can take place beyond the range of temperature, molar concentration of the fuel species, and equivalence ratio in this study.

For this study, the code provides a simple and less expensive alternative to CFD per time and CPU resources as it captures the flow parameters correctly.

The performance of the unit improved with the passive ring. This understanding can apply to the burner mixer design.

A great deal of work exists on free jet and its modification. The wall-bounded jet flow is not as popular. One highlight of this work was the impact of the wall and its geometry on the flow. This work adds to the body of knowledge by validating the existing research works and opening new research frontiers.

`

References

Abdulnaser, S. (2009). *Computational Fluid Dynamics.* Ventus Publishing ApS.

Agrawal, K. S. (2013). Performance of Venturi Scrubber. *International Journal of Engineering Research and Development, VII*(11), 53-69.

Ali, H., & Mohammed, B. (2020). CFD Analysis of Operating Condition Effects on Optimum Nozzle Exit Position of a Supersonic Ejector using the Refrigerant R134a. *Comptes Rendus Mécanique,* 1-14. doi:10.5802/crmeca.60

Andre, B. (2006). *Applied Computational Fluid Dynamics.* Retrieved September 21, 2018, from http://www.bakker.org

ANSYS Inc. (2009). *Ansys Fluent Theory Guide.* Southpointe: ANSYS Inc.

ANSYS, Inc. (2010). *ANSYS FLUENT User's Guide.* Southpointe: ANSYS, Inc.

Asim, M. (2008). *A Study of Subsonic Air-Air Ejector with Short Bent Mixing Tubes.* Queen's University, Department of Mechanical and Material Engineering. Ontario: Queen's University.

Baumgartner, G. M. (2014). *Flame Flashback in Premixed Hydrogen-Air Combustion Systems.* Munchen: Technische Universitat Munchen.

Behrouzi, P., & McGuirk, J. J. (2006). Effect of Tab Parameters on Near-Field Jet Plume Development. *Journal of Propulsion and Power, XXII*(3), 576-586.

Bengt, A., Ronnie, A., Love, H., Mikael, M., Rahman, S., & Beren, V. W. (2012). *Computational Fluid Dynamics for Engineers.* New York: Cambridge University Press.

Bernal, L. P., & Roshko, A. (1986). Streamwise Vortex Structure in Plane Mixing Layers. *Journal of Fluid Mechanics, CLXX*, 499-525.

Binder, G., & Kian, K. (1983). Cofined Jets in a Divergin Nozzle. *Turbulent Shear Flow 4*, (pp. 18-23). Karlsruhe.

Brandon, H. F. (2019). *An Exploration in Atmospheric Gas Burners.* Chanttanooga: The University of Tennessee.

Brandon, H. F. (2019). *An Exploration in Atmospheric Gas Burners.* Chanttanooga: University of Tennessee.

Brown, G. L. (1974). Entrainment and Large Structure in Turbulent Mixing Layer. *Fifth Australasian Conference on Hydraulics and Fluid Mechanics* (pp. 352-359). Christchurch: University of Adelaide.

Brown, G. L., & Roshko, A. (1974). On Density Effects and Large Structure in Turbulent Mixing Layers. *Journal of Fluid Mechanics, LXIV*(4), 775-816.

Bureau of Indian Standards. (2002). *Domestic Gas Stove for Use With Liquified Petroleum Gas.* New Delhi: Bureau of Indian Standards.

Callender, B., Gutmark, E., & Martens, S. (2008). Near Field Investigation of Chevron Nozzle Mechanism. *XLVI*(1). doi:10.2514/1.17720

Cengel, Y. A., & Cimbal, J. M. (2006). *Fluid Mechanics Fundamentals and Application.* New York: MCGraw- Hill.

Charles, B. E. (2003). *Idustrial Burners.* London: CRC Press LLC.

Chen, J., Hayes, B. S., & Fletcher, D. F. (1999). A Numerical and Experimental Study of Tangentially Injected Swirling Pipe Flow. *Second International Conference on CFD in Mineral and Process Industry*, (pp. 485-490). Melbourne.

Chung, L. K. (2006). *Combustion Physics.* New York: Cambridge University Press.

Chung, T. J. (2002). *Computational Fluid Dynamics.* Hunstvile: Cambridge University Press.

David, H. (2013, February 6). Application of of Ejector Technology to Subsea Fields of the future. pp. 1-10.

Demetris, V., Robert, H., & Wes, B. (2003). Radiant Wall Burners. In B. E. Charles, *Industrial Burners Hand Book* (pp. 505-520). New York: CRC Press LLC.

Department of Commerce Bureau of Standards. (1931). *Design of Gas Burners for Domestic Use.* washington D.C: Department of Commerce Bureau of Standards.

Dimotakis, P. E. (1991). *Turbulence Free Shear Layer Mixing and Combustion.* California: California Institute of Technology.

Dimotakis, P. E. (2005). Turbulent Mixing. *Annual Review of Fluid Mechanics, XXXVII*, 329-356. doi:10.1146/annurev.flui.36.050802.122015

Ecke, R. E. (2017). From 2D to 3D in Fluids: Unexpected Critical transition. *Focus on Fluids, DCCCXXVIII*, 1-4. doi:doi:10.1017/jfm.2017.507

El-Zahaby, A. M., Hamed, M. H., Omara, Z. M., & Eldesoukey, A. M. (2017). Study of Configuration and Performance of Air-Air Ejector Based on CFD Simulation. *Journal of Aeronautics and Aerospace Engineering, VI*(4), 1-9.

Enle, X., Xiaofeng, J., & Long, D. (2020). Optimizing Conical Nozzle of Venturi Ejector in Ejector Loop Reactor using Computational Fluid Dynamics. *Korean J.Chem.Eng.,, XXXVII*(11), 1829-1835. doi:10.1007/sl1814-020-0607-1

Erwin, P., Charles, B. P., & John, Z. H. (2013). *Process Burners 101.* New York: AICHE.

Faivre, V., & Poisnot, T. (2020). Experimental and Numerical Investigation of Jet Active Control for Combustion Application. *Journal of Turbulence*.

Fatong, J., Dazhang, Y., & Jing, X. (2021). Numerical Investigation on the Performance of Two-Throat Nozzle Ejectors with Different Mixing Chamber Structural Parameters. *energies, XIV*(6900), 1-16. doi:10.3390/en14216900

Gazzah, M. H., Boughattas, N., Belmabrouk, H., & Said, R. (2010). The Dynamic Field in Turbulent Round jet Discharging into a Co-Flowing Stream. *Natural Science, II*(6), 635-640.

Ghahremanian, S., & Moshfegh, B. (2011). Numerical and Experimental Verification of Initial, Transitional and Turbulent Regions of Free Turbulent Round Jet. *20th AIAA Computational Fluid Dynamics Conference* (pp. 1-12). Honolulu: American Institute of Aeronautics and Astronautics.

Glassman, I., & Yetter, R. (2008). *Combustion* (Fourth ed.). California: Elsevier.

Hadi, R. (2017). *Investigation of Radial flow Ejector Performance throough Experiment and Computational simulation.* Southern Queens Land : University of Southern Queens Land Australia.

Hafiz, A. M., Hafiz, M. A., Zabdur, R., Beomjoon, L., Young-Jin, B., Jongjae, C., . . . Muhammad, S. B. (2020). Numerical Modeling of Ejector and Development of Improved Methods for Design of Ejector-Assisted Refrigeration System. *Energies, XIII*(5835), 1-19.

Hussein, H. J., Capp, S. P., & George, W. K. (1994). Velocity Measurement in A High-Reynolds-number, Momentum-Conserving, Axisymetric, Turbulent Jet. *J.Fluid Mech, CCLVIII*, 31-75.

Irvin, G., & Richard, Y. A. (2008). *Combustion* (fourth ed.). California: Elsevier.

Juan, M., Carmen, P. V., Benito, D. A., Guilherme, D. B., & Denise, V. V. (2016). Geometry and Head Loss in Venturi Injectors Through Computational Fluid Dynamics. *Journal of the Brazilian Association of Agricultural Engineering, XXXVI*(3), 482-491. doi:10.1590/1809-4430

Kalantari, A. (2018). *Boundary Layer Flash Back of Turbulent Premixed Jet Flame at Elevated Pressure and Temperature.* Irvine: eScholarship.org.

Kemal, A., Sen, F., & Iskender, O. (2013). The Investigation of Gas Ejector Performance Using CFD Modelling. *TEM Journal*, 130-135.

Kenya Bureau of Standards. (2013). *Domestic Biogas Stove-Specification.* Nairobi: Kenya Bureau of Standards.

Keribo, K. F., & Barinaadaa, T. N. (2018). Adaptation of Ejector Refrigeration System to Gas Turbine Power Plant for Performance improvement. *Global Scientific Journals, VI*(10), 10-17.

Khodadadi, J. M., & Vlachos, N. S. (1988). Experimental and Numerical Study of Confined Coaxial Turbulent Jet. *AIAA Journal, XXVII*(5), 542-541.

Krzysztof, S., & Robert, G. (2017). The mixing Hydrodynamics and Efficiency of the Venturi Jet Mixer . *Technical Transaction*, 95-106.

Labus, T. L., & Symons, E. P. (1972). *Experimental Investigation of an Axisymmetric Free Jet With an Axially Uniform Velocity Profile.* Lewis Research Center. Washington, D. C: National Aeronautics and Space Administration.

Lawn, C. J. (2002). A simple Method for Design of Gas Burners ejectors. *Journal of Mechanical Science*, 1-31.

Lee, I. (2015). *An Experimental and Numerical Study of Confined and Non Reacting Turbulent Jet to Facilitate Homegenous Combustion in Industrial Furnaces.* University of Michigan, Department of Mechanical Engineering. Michigan: University of Michigan.

Liberzon, D., & Fernando, H. J. (2014). Pressure Distribution in Confined Jet Flow. *Journal of Fluids Engineering, CXXXVI*(031202), 1-4.

Liepmann, D., & Gharib, M. (1992). The Role of Streamwise Vorticity in Near-Field Entrainment of Round Jets. *Journal of Fluid Mechanics, CCXLV*, 643-668.

`

Lorenzo, G. (2008). *A Study of Fluid Dynamics of Domestic Gas Burners.* Bologna: University of Bologna.

Manisha, B., & Bhim, C. M. (2017). Prediction of Hydro dynamic Characteristics of a Venturi Scrubber by Using CFD Simulation. *South African Journal of Chemical Engineering, XXIV*(2017), 222-231.

Matrio, P., Florian, W., Christian, J., Stefan, P., Bernhard, S., Franz, W., & Michael, H. (2021). Design and Simulation of Gas Burner Ejectors. *Carbon Resources Conversion, IV*(2021), 28-35.

Mohsen, J. (2011). *Excited Jet and its Application.* Sverige: Chalmers University of Technology.

Mustafa, A., & Cuneyt, E. (2019). Three dimensional CFD modeling of a Steam Ejector. *Taylor & Francis Group*, 1-12. doi:10.1080/15567036.2019.1649326

Nakagawa, M., Berana, M. S., & Harada, A. (2008). Shock Waves in Supersonic Two-Phase Flow of CO2 in Converging-Diverging Nozzles. *International Refrigeration and Air Conditioning Conference* (pp. 1-7). Purdue: Purdue e-Pubs.

Nandita, N., Sruthi, R., Suriyaprabha, Sundaram, M., & Arun, K. P. (2018). Flow Visualisation of the Jet Exiting a Chevron nozzle. *Aeron Aero Open Acces J, II*(2), 62-65.

Nastase, I., Meslem, A., & Gervals, P. (2008). Primary and Secondary Vortical Structures Contribution in The Entrainment of Low Reynolds Number Jet Flows. *Exp.Fluids, XLIV*(2008), 1027-1033. doi:10.1007/s00348-008-0488-2

Parker, R., Rajagopalan, S., & Antonia, R. A. (2001). Control of an Axisymetric Jet Using a Passive Ring. *14th Australasian Fluid Mechanic Conference* (pp. 769-772). Adelaide: Adelaide University.

Peter, T., Robert, C., & Darren, S. (2016). *Research and Development of Natural Draft Ultra-Low Emissions Burners for Gas Appliances.* California: Lawrence Berkeley National Laboratory.

Philip, O. (1997). *Low NOx Combustion Utilizing a Coanda Ejector Burner.* Shefield: University of Shefield.

Pope, S. B. (2000). *Free Shear Flows.* Cambridge: Cambridge University Press.

Ragland, K. W., & Bryden, K. M. (2011). *Combustion Engineering* (2nd ed.). New York: CRC Press.

Rajagopalan, S., & Antonia, R. A. (2007). Turbulence and Drag Control in Jet and Wake Flow. *Sadhana, XXXII*(1 & 2), 133-144.

Reeder, M. F., & Samimy, M. (1996). The Evolution of a Jet With Vortex-Generating Tabs: Real-Time Visualisation and Quantitative Measurement. *Journal of Fluid Mechanics, 311*, 73-118.

Rengasamy, K., & Alakesh, M. C. (2017). Experiment on Effective tripping device in a Zero Gradient Turbulent Boundary Layer. *Journal of Physics, DCCCXXVI*(2017).

Revuelta, A., Martinez-Bazan, C., Sanchez, A., & Amable, L. (2004). Laminar Craya-Curtet Jets. *Physics of Fluids, XVI*(1), 208-211.

Reynolds, W. C., Parekh, D. E., Juvet, P. J., & Lee, M. J. (2003). Bifurcuting and Blooming Jet. *Annu. Rev. Fluid Mech, XXXV*, 295-315. doi:doi:10.1146/annurev.fluid.35.101101.161128

Robert, J. P. (2010). *Design of Atmospheric Gas Burners.* Meadow: PDH Online/PDH Center.

Sadeghi, H., & Pollard, A. (2012). Effects of Passive Control Rings Position in Shear Layer and Potential Core of a Turbulent Round Jet. *Physics of Fluid, XXIV*(115103), 1-22. doi:doi:10.1063/1.4767535

Sadeghia, H., & Pollard, A. (2012). Effects of Passive Control Rings Positioned in the Shear Layer and Potential Core of a Turbulent Round Jet. *Physics of Fluids, XXIV*(115103), 1-22. doi:10.1063/1.4767535

Saponaro, A., Senneca, O., Cerciello, F., Brand, D. J., Torresi, M., Cesareo, F., . . . Panebianco, V. (2020). CFD modelling: A powerful Tool for High Efficiency Burner Design. *INFUB* (pp. 1-13). Porto: INFUB.

Schmidt, R., & Hupfer, A. (2021). Design and Numerical Simulation of Ejector Nozzles for Very Small Turbojet Engines. *CEAS Aeronautical Journal, XII*(2021), 923-940. doi:10.1007/s13272-0121-00537-3

Scott, D., Aidoun, Z., Bellache, O., & Ouzzane, M. (2008). CFD simulation of a Supersonic Ejector for Use in Refrigeration Application. *International Refrigeration and Ir Condition Conference*, (pp. 1-8). Purdue.

Selas. (2021). *Atmospheric Gas Burners.* Ohio: Selas Heat Technology Company.

Slessor, M. D., Bond, C. L., & Dimotakis, P. E. (1998). Turbulent Shear Lyer Mixing at High Reynolds Number: Effects of Inflow Condition. *Journal of Fluid Mechanics, CCCLXXVI*, 115-138.

Sobieski, W. (2003). Performance of an Air-Air Ejector: An Attempt at Numerical Modeling. *Task Quarterly, VII*(3), 449-457.

Subramanian, H. G., Nagarjun, S., Kumar, S. K., Kumar, A. B., Srikanth, V., & Srikrishnan, A. R. (2018). Mixing Ehancement Using Chevron Nozzle Studies on Free Jets and Confined Jets. *Sadhana, XLIII*(109). doi:10.1007/s1204-018-0898-7

Vashahi, F., Ra, S., Choi, Y., & Lee, J. K. (2017). Influence of Design Parameters on The Air/Liquid Ratio of an Air Induction Nozzle. *Journal of Mechanics*. doi:10.1017/jmech.2017.12

Versteeg, H. K., & Malalasekera, W. (1995). *An introduction to Computational Fluid Dynamics an Introduction.* New York: Longman Scientific and Technical.

Versteeg, H. K., & Malalasekera, W. (2007). *An Introduction to Computational Fluid Dynamics* (2nd ed.). Harlow: Pearson Education Limited.

Voropayev, S. I., Sanchez, X., Nath, C., Webb, S., & Fernando, H. J. (2011). Evolution of Confined Turbulent Jet in a Long Cylindrical Cavity: Homogenous Fluid. *Physics of Fluid, XXIII*(115106), 1-11.

Westbrook, C. K., & Dryer, F. L. (1981). Simplified Reaction Mechanism for Oxidation of Hydrocarbons Fuels in Flame. *Combustion Science and Technology, XXVII*, 31-43.

William, O. M., José, A. P., Iván, D. P., Johan, S. Z., & John, A. H. (2020). Analysis of a Jet Pump Performance under Different Primary Nozzle Positions and Inlet Pressures using two Approaches: One Dimensional Analytical Model and Three Dimensional CFD Simulations . *Journal of Applied and Computational Mechanics, VI*(2020), 1228-1244 .

Yanqi, S., & Wenquan, N. (2012). Simulating the Effects of Structural Parameters on the Hydraulic Performances of VenturiTube. *Modelling and Simulation in Engineering, MMXII*, 1-7. doi:10.1155/2012/458368

Zaman, K. B. (2001). *Effect of Delta Tabs on Free Jet from Complex Nozzle.* Cleveland: NASA.

Zaman, K. B., Reeder, M. F., & Samimy, M. (1994). Control of an Axisymetric Jet Using Vortex Generators. *Phys. Fluids, VI*(2).

Zhang, J. K. (2017). Analysis on the Effect of Venturi Tube Structural Parameters on Fuid Flow. *AIP Advances*, 1-7. doi:10.1063/1.4991441

Zihzhen, W., Tianyang, L., Fangxiang, W., Lin, G., & Rui, Z. (2020). Numerical Simulation of Polymer Dispersion Systems for Polymer Injection on Offshore Platforms. *Acs Omega, V*, 20343-20352.

`

Appendices

Appendix I Code for jet flow performance computation

```
%--------------------------------------------------------------------%
%             SPREAD ANGLE EFFECT ON JET VELOCITY PROFILE
%--------------------------------------------------------------------%
```

INTRODUCTORY STATEMENT

This code creates several plots in different figure windows to compare the variation in radial and axial velocity profile of a jet at different spread angles. It prompts the user to key in certain parameters which are required to carry out the computations the parameters include: The jet angle (tt) The diameter (d) of the fuel nozzle length of the mixing tube Air density (rhoa) Fuel density (rhof) Velocity of fuel passing through the nozzle Number of points along and across the jet axis where the computation would be executed

```
clear
```

INSTRUCTION FOR USERS

```
fprintf('\n');
disp('PLEASE READ THE FOLLOWING INSTRUCTIONS');
disp('LPG- is assumed to consist of ');
disp('PROPANE');
disp('BUTANE  and');
disp('METHANE');
disp('The mole fraction of the fuel should be entered in that order when prompted');

fprintf('\n');

disp('The variation in angle of jet flow affects the entrainment ratio considerably');
disp('three of such angle at which flow parameters are to be compared should be entered at the prompt');
disp('-----------------------------------------------------------------------------------');
fprintf('\n');
```

```
PLEASE READ THE FOLLOWING INSTRUCTIONS
LPG- is assumed to consist of
PROPANE
BUTANE  and
METHANE
The mole fraction of the fuel should be entered in that order when prompted

The variation in angle of jet flow affects the entrainment ratio considerably
three of such angle at which flow parameters are to be compared should be entered at the prompt
-----------------------------------------------------------------------------------
```

`

SPECIFY THE CONDITION AT INLET

```
fuel_specie1=input ('Enter the mole fraction of PROPANE in the fuel; ');
fuel_specie2=input ('Enter the mole fraction of BUTANE in the fuel;  ');
fuel_specie3=input ('Enter the mole fraction of METHANE in the fuel; ');
mole_ratio=[fuel_specie1,fuel_specie2,fuel_specie3];

Tin=input('Enter the initial temperature of fuel in Kelvin; ');

T=input('Enter the initial temperature of air in Kelvin; ');

NE= 3;
tt=zeros(1,NE);
for j=1:NE
    jet_angle=input('Enter the jet the angles in degrees; ');
   tt(j)= jet_angle;
end

AFR=input('Enter the STOICHIOMETRIC air/fuel ratio of the fuel; ');
```

SPECIFY SOME OTHER PARAMETERS/PHYSICAL PROPERTIES OF SPECIES

```
mm=(6.6667e-05);             % mass flow rate of gas in kg/m3
d=0.0050;                    % diameter of gas tube at inlet
R=d/2;                       % radius of gas tube at inlet
l=0.1000;                    % length of the mixing tube
rhoa=density_air(T);         % density of air at inlet
molarmair=28.96;             % molar mass of air

rhopropane=density_propane(Tin);   % density of propane at inlet
rhobutane=density_butane(Tin);     % density of butane at inlet
rhomethane=density_methane(Tin);   % density of methane at inlet
rho=[rhopropane,rhobutane,rhomethane];
rhof=sum(mole_ratio.*rho);     % overall density of the fuel/gas species

Af=pi*d^2/4;             % crossectional Area of gas tube at inlet
uf=mm/(Af*rhof);         % velocity of gas at inlet
q=uf*Af;                 % Volumetric flow of gas fuel per seconds
np=50;                   % no of computational points along the mixing tube

viscosity_propane=Kviscosity_propane(Tin); % viscosity of propane at inlet
viscosity_butane=Kviscosity_butane(Tin);   % viscosity of butane at inlet
viscosity_methane=Kviscosity_methane(Tin); % viscosity of methane at inlet
viscosity=[viscosity_propane,viscosity_butane,viscosity_methane];
viscosity_fuel=sum(mole_ratio.*viscosity); % overall density of gas species


RE=d*uf/(viscosity_fuel);                  % Reynolds number at inlet

molarma_propane=44;                        % molar mass of propane
molarma_butane=58;                         % molar mass of butane
molarma_methane=16;                        % molar mass of methane
```

```
molar_mass=[molarma_propane,molarma_butane,molarma_methane];
molarmafuel=sum(mole_ratio.*molar_mass);   % molar mass of fuel/gas species

specific_ratio_propane=1.126;
specific_ratio_butane=1.091;
specific_ratio_methane=1.299;

R_propane=188.5;    %J/Kg.K  gas constant propane
R_butane=143.3;     %J/Kg.K  gas constant for butane
R_methane=518.2;    %J/Kg.K  gas constant for methane
UniversalR=8314.5;  %J/mol.K  universal gas constant
```

COMPUTE THE MACH NUMBER OF THE FLOW AT INLET

```
if mole_ratio(1)==1
Mach_number=uf/sqrt(specific_ratio_propane*R_propane*Tin);
else
    if  mole_ratio(2)==1
        Mach_number=uf/sqrt(specific_ratio_butane*R_butane*Tin);
    else
         Mach_number=uf/sqrt(specific_ratio_methane*R_methane*Tin);
    end
end
```

COMPUTE THE RADIAN EQUIVALENT OF THE SPECIFIED ANGLES

```
t=zeros(1,length(tt));
for i=1:length(tt)
    theta=(2*pi*tt(i))/360;
    t(i)=theta;
end
```

DIVIDE THE DOMAIN INTO np EQUAL POINTS STARTING FROM ORIGIN

```
X=linspace(0,l,np);

% Normalise the computational points X by dividing with nozzle diameter
Xnorm=zeros(1,length(X));
for i=1:length(X);
    x=X(i)/d;
    Xnorm(i)=x;
end

% locate the point where Xnorm is above 2.8. That marks the nozzle exit
inv=Xnorm(1);                   % set the initial value to Xnorm(1)
for i=1:length(Xnorm);
if inv < 2.8;
    inv=Xnorm(i+1);
    k=i+1;
    %xnorm(1)=xnorm(i+1);
```

`

```
end
end
```

COMPUTE THE RADIUS OF THE JET AT THE POINTS/ANGLE SPECIFIED ABOVE

```
jetRadius=zeros(length(tt),np);
for i=1:length(tt)
    for j=1:np
    r=X(j)*tan(t(i));
    jetRadius(i,j)=r;
    end
end
```

COMPUTE THE CROSS-SECTIONAL AREA OF THE JET Am AT THE SPECIFIED POINTS

```
Am=zeros(length(tt),np);
for i=1:length(tt);
    for j=1:np
       Am(i,j)=pi*jetRadius(i,j).^2;
    end
end
```

COMPUTE THE AXIAL VOLUMETRIC FLUX OF MIXTURE Q FOR EACH OF THE ANGLES

```
Q=zeros(length(tt),np);
for i=1:length(tt);
   for  j=1:np;
    %Q(i,j)= (q*(rhoa - rhof) + (q^2*(rhoa - rhof)^2 +
(4*Am(i,j)*rhoa*rhof*q^2)/Af)^(1/2))/(2*rhoa);
    Q(i,j)=((q^2*(rhoa - rhof)^2 + 4*R^2*(X(j)*tan(t(i)))^2*pi^2*rhoa*rhof*uf^2)^(1/2) + q*(rhoa
- rhof))/(2*rhoa);
   end
end
%
```

COMPUTE THE DENSITY OF THE MIXTURE ALONG THE TUBE FOR EACH OF THE ANGLES

```
%Compute the density of the mixture
%for each of the spread angles at each X position along the tube
rhom=zeros(length(tt),np);
for i=1:length(tt);
    for j=1:np;
    rhom(i,j)=rhoa+(q/Q(i,j))*(rhof-rhoa);
    end
end
```

COMPUTE THE AVERAGE CENTERLINE VELOCITY umax ALONG THE TUBE

`

```
umax=zeros(length(tt),np);
 for i=1:length(tt);
     for j=1:np;
       um=uf*R./jetRadius(i,j)*((rhof./rhom(i,j)))^0.5;
       umax(i,j)=um;
     end
 end
```

COMPUTE THE ENTRAINMENT VELOCITY uradial ALONG THE TUBE

```
uradial=zeros(length(tt),np);
 for i=1:length(tt);
     for j=1:np;
       ur=uf*R./(2*X(j))*(rhof./rhom(i,j))^0.5;
       uradial(i,j)=ur;
     end
 end
center_line_velocity=umax;
entrainment_velocity=uradial;
Jflux=rhoa*uradial.^2/(rhof*uf^2);
momentum_flux_ratio=Jflux;
```

```
%Extract from the matrix jetRadius all the elements of the first row
jetrp1=jetRadius(1,:);
jetp1=zeros(np,np);
for i=1:length(jetRadius)
    %call the function radial_p to divide each of the extracted elements
    %corresponding to a specified angle into 'np' equal parts
    jetrp=radial_p(jetrp1(i),np);
    jetp1(i,:)=jetrp;
end

% compute the velocity at each of the jetp1 positions
urp1=zeros(np,np);
for i=k:length(Xnorm);
    %Call the function uradial_p to compute velocities at each
    %jetp1 value along the tube
    VV=uradial_p(umax(1,i),jetp1(i,:),X(i),t(1));
    urp1(i,:)=VV;
end
% compute the rms of the velocities urp1
urpsq1=urp1.^2;
urpsq1=urpsq1';
urrms1=(mean(urpsq1)).^0.5;

jetrp2=jetRadius(2,:);
jetp2=zeros(np,np);
for i=1:length(jetRadius)
    %call the function radial_p to divide each of the extracted elements
    %corresponding to a specified angle into 'np' equal parts
    jetrp=radial_p(jetrp2(i),np);
    jetp2(i,:)=jetrp;
```

`

```
end

% compute the velocity at each of the jetp2 positions
urp2=zeros(np,np);
for i=k:length(X);
    %Call the function uradial_p to compute velocities at each
    %jetp2 value along the tube
    VV=uradial_p(umax(2,i),jetp2(i,:),X(i),t(2));
    urp2(i,:)=VV;
end

% compute the rms of the velocities urp2
urpsq2=urp2.^2;
urpsq2=urpsq2';
urrms2=(mean(urpsq2)).^0.5;

jetrp3=jetRadius(3,:);
jetp3=zeros(np,np);
for i=1:length(jetRadius)
    %call the function radial_p to divide each of the extracted elements
    %corresponding to the third specified angle into 'np' equal parts
    jetrp=radial_p(jetrp3(i),np);
    jetp3(i,:)=jetrp;
end

% compute the velocity at each of the jetp3 positions
urp3=zeros(np,np);
for i=k:length(X);
    %Call the function uradial_p to compute velocities at each
    %jetp3 value along the tube
    VV=uradial_p(umax(3,i),jetp3(i,:),X(i),t(3));
    urp3(i,:)=VV;
end

% compute the rms of the velocities urp3
urpsq3=urp3.^2;
urpsq3=urpsq3';
urrms3=(mean(urpsq3)).^0.5;
```

```
ma1=(Q(1,1:end)-q)*rhoa;
ma2=(Q(2,1:end)-q)*rhoa;
ma3=(Q(3,1:end)-q)*rhoa;

mfuel=q*rhof;
mar1=ma1./mfuel;
mar2=ma2./mfuel;
mar3=ma3./mfuel;
massRatio=[mar1;mar2;mar3];
```

```
mfraction_air1=ma1./(rhom(1,1:end).*Q(1,1:end));
mfraction_air2=ma2./(rhom(2,1:end).*Q(2,1:end));
mfraction_air3=ma3./(rhom(3,1:end).*Q(3,1:end));
```

```
specificR1= UniversalR./((mfraction_air1.*molarmair)+((1-mfraction_air1).*molarmafuel));
specificR2= UniversalR./((mfraction_air2.*molarmair)+((1-mfraction_air2).*molarmafuel));
specificR3= UniversalR./((mfraction_air3.*molarmair)+((1-mfraction_air3).*molarmafuel));

%staticp1=rhom(1,1:end).*specificR1*(0.5*T+0.5*Tin);
staticp1=rhom(1,1:end).*specificR1.*(mfraction_air1.*T+(1-mfraction_air1).*Tin);
staticp2=rhom(2,1:end).*specificR2.*(mfraction_air2.*T+(1-mfraction_air2).*Tin);
staticp3=rhom(3,1:end).*specificR3.*(mfraction_air3.*T+(1-mfraction_air3).*Tin);

% compute dynamic pressure
 Urms=[urrms1;urrms2;urrms3];
 dynamicp=0.5.*rhom.*Urms.^2;


totalp1=staticp1+dynamicp(1,1:end);
totalp2=staticp2+dynamicp(2,1:end);
totalp3=staticp3+dynamicp(3,1:end);

%Specify the points along the length of the tube
% where the velocity profile will be ploted

po=round(linspace(k,length(Xnorm),5));
jetR=jetRadius(:,po);

% plot the velocity profiles at the specified points for a specified
% angle of spread.
figure(1)
p=po(1);
jetR11=linspace(-jetR(1,1),jetR(1,1),np);
u11=umax(1,p)*exp(-(jetR11).^2/(0.5*(X(p)).^2*(tan(t(1)))^2));
plot(jetR11./d,u11./uf)
f11=sprintf('x/d= %.2f', round(Xnorm(p)));
hold on

p=po(2);
jetR12=linspace(-jetR(1,2),jetR(1,2),np);
u12=umax(1,p)*exp(-(jetR12).^2/(0.5*(X(p)).^2*(tan(t(1)))^2));
plot(jetR12./d,u12./uf)
f12=sprintf('x/d= %.2f', round(Xnorm(p)));
hold on

p=po(3);
jetR13=linspace(-jetR(1,3),jetR(1,3),np);
u13=umax(1,p)*exp(-(jetR13).^2/(0.5*(X(p)).^2*(tan(t(1)))^2));
plot(jetR13./d,u13./uf)
f13=sprintf('x/d= %.2f', round(Xnorm(p)));
hold on



p=po(4);
jetR14=linspace(-jetR(1,4),jetR(1,4),np);
u14=umax(1,p)*exp(-(jetR14).^2/(0.5*(X(p)).^2*(tan(t(1)))^2));
plot(jetR14./d,u14./uf)
```

`

```
f14=sprintf('x/d= %.2f', round(Xnorm(p)));
hold on

p=po(5);
jetR15=linspace(-jetR(1,5),jetR(1,5),np);
u15=umax(1,p)*exp(-(jetR15).^2/(0.5*(X(p)).^2*(tan(t(1)))^2));
plot(jetR15./d,u15./uf)
f15=sprintf('x/d= %.2f', round(Xnorm(p)));
hold off
title1=sprintf('Radial velocity profile of jet at RE= %d and %d degrees spread',RE, tt(1));

legend(f11,f12,f13,f14,f15);
title(title1)
xlabel('r/d')
ylabel('ur/uf')

% plot the velocity profiles at the specified points for a 2nd specified
% angle of spread.
figure(2)
p=po(1);
jetR21=linspace(-jetR(2,1),jetR(2,1),np);
u21=umax(2,p)*exp(-(jetR21).^2/(0.5*(X(p)).^2*(tan(t(2)))^2));
plot(jetR21./d,u21./uf)
f21=sprintf('x/d= %.2f', round(Xnorm(p)));
hold on

p=po(2);
jetR22=linspace(-jetR(2,2),jetR(2,2),np);
u22=umax(2,p)*exp(-(jetR22).^2/(0.5*(X(p)).^2*(tan(t(2)))^2));
plot(jetR22./d,u22./uf)
f22=sprintf('x/d= %.2f', round(Xnorm(p)));
hold on

p=po(3);
jetR23=linspace(-jetR(2,3),jetR(2,3),np);
u23=umax(2,p)*exp(-(jetR23).^2/(0.5*(X(p)).^2*(tan(t(2)))^2));
plot(jetR23./d,u23./uf)
f23=sprintf('x/d= %.2f', round(Xnorm(p)));
hold on



p=po(4);
jetR24=linspace(-jetR(2,4),jetR(2,4),np);
u24=umax(2,p)*exp(-(jetR24).^2/(0.5*(X(p)).^2*(tan(t(2)))^2));
plot(jetR24./d,u24./uf)
f24=sprintf('x/d= %.2f', round(Xnorm(p)));
hold on

p=po(5);
jetR25=linspace(-jetR(2,5),jetR(2,5),np);
u25=umax(2,p)*exp(-(jetR25).^2/(0.5*(X(p)).^2*(tan(t(2)))^2));
plot(jetR25./d,u25./uf)
f25=sprintf('x/d= %.2f', round(Xnorm(p)));
```

`

```
hold off
title1=sprintf('Radial velocity profile of jet at RE= %d and %d degrees spread',RE, tt(2));

legend(f21,f22,f23,f24,f25);
title(title1)
xlabel('r/d')
ylabel('ur/uf')

% plot the velocity profiles at the specified points for a third specified
% angle of spread.
figure(3)
p=po(1);
jetR31=linspace(-jetR(3,1),jetR(3,1),np);
u31=umax(3,p)*exp(-(jetR31).^2/(0.5*(X(p)).^2*(tan(t(3)))^2));
plot(jetR31./d,u31./uf)
f31=sprintf('x/d= %.2f', round(Xnorm(p)));
hold on

p=po(2);
jetR32=linspace(-jetR(3,2),jetR(3,2),np);
u32=umax(3,p)*exp(-(jetR32).^2/(0.5*(X(p)).^2*(tan(t(3)))^2));
plot(jetR32./d,u32./uf)
f32=sprintf('x/d= %.2f', round(Xnorm(p)));
hold on

p=po(3);
jetR33=linspace(-jetR(3,3),jetR(3,3),np);
u33=umax(3,p)*exp(-(jetR33).^2/(0.5*(X(p)).^2*(tan(t(3)))^2));
plot(jetR33./d,u33./uf)
f33=sprintf('x/d= %.2f', round(Xnorm(p)));
hold on



p=po(4);
jetR34=linspace(-jetR(3,4),jetR(3,4),np);
u34=umax(3,p)*exp(-(jetR34).^2/(0.5*(X(p)).^2*(tan(t(3)))^2));
plot(jetR34./d,u34./uf)
f34=sprintf('x/d= %.2f', round(Xnorm(p)));
hold on

p=po(5);
jetR35=linspace(-jetR(3,5),jetR(3,5),np);
u35=umax(3,p)*exp(-(jetR35).^2/(0.5*(X(p)).^2*(tan(t(3)))^2));
plot(jetR35./d,u35./uf)
f35=sprintf('x/d= %.2f', round(Xnorm(p)));
hold off
title1=sprintf('Radial velocity profile of jet at RE= %d and %d degrees spread', tt(3));

legend(f31,f32,f33,f34,f35);
title(title1)
xlabel('r/d')
ylabel('ur/uf')
```

`

```
% locate the radial position in the jet where the vlocity um is equal to
% half of the maximum velocity
figure(4)
p=po(1);
for i=1:np/2
    um=0.5*umax(1,p);
    if u11(i)<=um;
        n=i;

    end
end
%normalise u11 with umax and plot the values against the radial points jetR11
%normalised with jetR11(n) correspondin to u11= 0.5*umax1.
plot(jetR11./(jetR11(n)),u11./umax(1,p),'k-')
hold on


p=po(2);
% locate the radial position in the jet where the vlocity um is equal to
% half of the maximum velocity
for i=1:np/2
    um=0.5*umax(1,p);
    if u12(i) <= um;
        n=i;

    end
end

%normalise u12 with umax and plot the values against the radial points jetR12
%normalised with jetR12(n) correspondin to u12= 0.5*umax1.
plot(jetR12./(jetR12(n)),u12./umax(1,p),'g*')
hold on

p=po(3);
% locate the radial position in the jet where the vlocity um is equal to
% half of the maximum velocity
for i=1:np/2
    um=0.5*umax(1,p);
    if u13(i)<=um;
        n=i;

    end
end

%normalise u13 with umax and plot the values against the radial points jetR13
%normalised with jetR13(n) correspondin to u13= 0.5*umax.
plot(jetR13./(jetR13(n)),u13./umax(1,p),'bo')
hold on

p=po(4);
% locate the radial position in the jet where the vlocity um is equal to
% half of the maximum velocity
for i=1:np/2
    um=0.5*umax(1,p);
```

```
    if u14(i)<= um;
        n=i;

    end
end

%normalise u14 with umax and plot the values against the radial points jetR11
%normalised with jetR14(n) correspondin to u14= 0.5*umax.
plot(jetR14./(jetR14(n)),u14./umax(1,p),'r>')
hold on

p=po(5);
% locate the radial position in the jet where the vlocity um is equal to
% half of the maximum velocity
for i=1:np/2
    um=0.5*umax(1,p);
    if u15(i)<= um;
        n=i;

    end
end

%normalise u15 with umax and plot the values against the radial points jetR15
%normalised with jetR15(n) correspondin to u15= 0.5*umax.
plot(jetR15./(jetR15(n)),u15./umax(1,p),'ks')
hold off
legend(f21,f22,f23,f24,f25);
legend('boxoff')
title1=sprintf('similarity profile of axial velocity  at RE= %d and %d degrees spread',RE,
tt(1));
xlabel('r/r50%')
ylabel('u/umax')
title(title1)

figure(5)
% locate the radial position in the jet where the vlocity um is equal to
% half of the maximum velocity
p=po(1);
for i=1:np/2
    um=0.5*umax(2,p);
    if u21 <= um;
        n=i;

    end
end

%normalise u21 with umax and plot the values against the radial points jetR21
%normalised with jetR21(n) correspondin to u21= 0.5*umax.
plot(jetR21./(jetR21(n)),u21./umax(2,p),'k-')
hold on


p=po(2);
%locate the radial position in the jet where the vlocity um is equal to
```

`

```
% half of the maximum velocity
for i=1:np/2
    um=0.5*umax(2,p);
    if u22(i)<=um;
        n=i;

    end
end
%normalise u22 with umax and plot the values against the radial points jetR22
%normalised with jetR22(n) correspondin to u22= 0.5*umax.
plot(jetR22./(jetR22(n)),u22./umax(2,p),'g*')
hold on

p=po(3);
%locate the radial position in the jet where the vlocity um is equal to
%half of the maximum velocity
for i=1:np/2
    um=0.5*umax(2,p);
    if u23(i)<=um;
        n=i;

    end
end

%normalise u23 with umax and plot the values against the radial points jetR23
%normalised with jetR23(n) correspondin to u23= 0.5*umax.
plot(jetR23./(jetR23(n)),u23./umax(2,p),'bo')
hold on

p=po(4);
%locate the radial position in the jet where the vlocity um is equal to
%half of the maximum velocity
for i=1:np/2
    um=0.5*umax(2,p);
    if u24(i)<=um;
        n=i;

    end
end
%normalise u24 with umax and plot the values against the radial points jetR24
%normalised with jetR24(n) correspondin to u24= 0.5*umax.
plot(jetR24./(jetR24(n)),u24./umax(2,p),'r>')
hold on

p=po(5);
%locate the radial position in the jet where the velocity um is equal to
%half of the maximum velocity
for i=1:np/2
    um=0.5*umax(2,p);
    if u25(i)<=um;
        n=i;

    end
end
```

`

```
%normalise u25 with umax and plot the values against the radial points jetR25
%normalised with jetR25(n) correspondin to u25= 0.5*umax.
plot(jetR25./(jetR25(n)),u25./umax(2,p),'ks')
hold off
legend(f21,f22,f23,f24,f25);
legend('boxoff')
title1=sprintf('similarity profile of axial velocity  at RE= %d and %d degrees spread',RE,
tt(2));

xlabel('r/r50%')
ylabel('u/umax')
title(title1)
```

```
figure(6)
p=po(1);
%locate the radial position in the jet where the vlocity um is equal to
%half of the maximum velocity
for i=1:np/2
    um=0.5*umax(3,p);
    if u31(i)<=um;
        n=i;

    end
end

%normalise u31 with umax and plot the values against the radial points jetR31
%normalised with jetR31(n) correspondin to u31= 0.5*umax.
plot(jetR31./(jetR31(n)),u31./umax(3,p),'k-')
hold on


p=po(2);
%locate the radial position in the jet where the vlocity um is equal to
%half of the maximum velocity
for i=1:np/2
    um=0.5*umax(3,p);
    if u32(i)<=(um);
        n=i;

    end
end

%normalise u32 with umax and plot the values against the radial points jetR32
%normalised with jetR32(n) correspondin to u32= 0.5*umax.
plot(jetR32./(jetR32(n)),u32./umax(3,p),'g*')
hold on

p=po(3);
%locate the radial position in the jet where the vlocity um is equal to
%half of the maximum velocity
for i=1:np/2
    um=0.5*umax(3,p);
    if u33(i)<= um;
        n=i;
```

`

```
    end
end
%normalise u33 with umax and plot the values against the radial points jetR33
%normalised with jetR33(n) corresponding to u33= 0.5*umax.
plot(jetR33./(jetR33(n)),u33./umax(3,p),'bo')
hold on

p=po(4);
%locate the radial position in the jet where the vlocity um is equal to
%half of the maximum velocity
for i=1:np/3
    um=0.5*umax(3,p);
    if u34(i)<= um;
        n=i;

    end
end
%normalise u34 with umax and plot the values against the radial points jetR33
%normalised with jetR34(n) corresponding to u34= 0.5*umax.
plot(jetR34./(jetR34(n)),u34./umax(3,p),'r>')
hold on

p=po(5);
%locate the radial position in the jet where the vlocity um is equal to
%half of the maximum velocity
for i=1:np/2
    um=0.5*umax(3,p);
    if u35(i)<=(um);
        n=i;

    end
end

%normalise u35 with umax and plot the values against the radial points jetR35
%normalised with jetR35(n) corresponding to u35= 0.5*umax.
plot(jetR35./(jetR35(n)),u35./umax(3,p),'ks')
hold off
legend(f21,f22,f23,f24,f25);
legend('boxoff')
title1=sprintf('similarity profile of axial velocity  at RE= %d and %d degrees spread',RE,
tt(3));
xlabel('r/r50%')
ylabel('u/umax')
title(title1)
```

plot the maximum velocity along the tube for each specified angle

```
figure(7)
ufr1=(uf./umax(1,:));
plot(Xnorm,ufr1)
legend1=sprintf('%d degrees spread <', tt(1));
hold on
```

`

```
ufr2=(uf./umax(2,:));
plot(Xnorm,ufr2)
legend2=sprintf('%d degrees spread <', tt(2));
hold on

ufr3=(uf./umax(3,:));
plot(Xnorm,ufr3)
legend3=sprintf('%d degrees spread <', tt(3));
hold off
legend(legend1,legend2,legend3,'location','northwest')
legend('boxoff')
xlabel('x/d')
ylabel('uf/umax')
title1=sprintf('Axial variation of maximum velocity at RE=%d ',RE);
title(title1)

% plot the volume of air/fuel mixture along the tube for each specified angle
figure(8)
plot(Xnorm(1:end),Q(1,1:end))
hold on

plot(Xnorm(1:end),Q(2,1:end))
hold on

plot(Xnorm(1:end),Q(3,1:end))
hold off
legend(legend1,legend2,legend3,'location','northwest')
legend('boxoff')
xlabel('x/d')
ylabel('Volume of air/fuel mixture (m^3)')
title1=sprintf('Axial variation in volume of air/fuel mixture at RE=%d ',RE);
title(title1)

figure(9)

plot(Xnorm(k:end),urrms1(k:end))
hold on
plot(Xnorm(k:end),urrms2(k:end))
hold on
plot(Xnorm(k:end),urrms3(k:end))
hold off
legend(legend1,legend2,legend3,'location','northeast')
legend('boxoff')
xlabel('x/d')
ylabel('RMS velocity (m/s)')
title1=sprintf('RMS velocity profile at RE=%d ',RE);
title(title1)

figure(10)
plot(jetR11/d,u11/uf)
hold on
plot(jetR21/d,u21/uf)
```

`

```
hold on
plot(jetR31/d,u31/uf)
title1=sprintf('Variation in velocity profile with jet spread at RE=%d and x/d= %d
',RE,round(Xnorm(po(1))));
hold off
legend(legend1,legend2,legend3,'location','northeast')
legend('boxoff')
xlabel('r/d')
ylabel('ur/uf')
title(title1)
```

```
figure(11)
plot(jetR12/d,u12/uf)
hold on
plot(jetR22/d,u22/uf)
hold on
plot(jetR32/d,u32/uf)
title1=sprintf('Variation in velocity profile with jet spread at RE=%d and x/d= %d
',RE,round(Xnorm(po(2))));
hold off
legend(legend1,legend2,legend3,'location','northeast')
legend('boxoff')
xlabel('r/d')
ylabel('ur/uf')
title(title1)
```

```
figure(12)
plot(jetR13/d,u13/uf)
hold on
plot(jetR23/d,u23/uf)
hold on
plot(jetR33/d,u33/uf)
title1=sprintf('Variation in velocity profile with jet spread at RE=%d and x/d= %d
',RE,round(Xnorm(po(3))));
hold off
legend(legend1,legend2,legend3,'location','northeast')
legend('boxoff')
xlabel('r/d')
ylabel('ur/uf')
title(title1)
```

```
figure(13)
plot(jetR14/d,u14/uf)
hold on
plot(jetR24/d,u24/uf)
hold on
plot(jetR34/d,u34/uf)
title1=sprintf('Variation in velocity profile with jet spread at RE=%d and x/d= %d
',RE,round(Xnorm(po(4))));
hold off
legend(legend1,legend2,legend3,'location','northeast')
legend('boxoff')
xlabel('r/d')
ylabel('ur/uf')
title(title1)
```

`

```
figure(14)
plot(jetR15/d,u15/uf)
hold on
plot(jetR25/d,u25/uf)
hold on
plot(jetR35/d,u35/uf)
title1=sprintf('Variation in velocity profile with jet spread at RE=%d and x/d= %d
',RE,round(Xnorm(po(5))));
hold off
legend(legend1,legend2,legend3,'location','northeast')
legend('boxoff')
xlabel('r/d')
ylabel('ur/uf')
title(title1)



figure(15)
plot(Xnorm(k:end),ma1(k:end))
hold on
plot(Xnorm(k:end),ma2(k:end))
hold on
plot(Xnorm(k:end),ma3(k:end))
hold off
legend(legend1,legend2,legend3,'location','northwest')
legend('boxoff')
xlabel('x/d')
ylabel('Mass of entrained air (Kg)')
title1=sprintf('Effect of spread angle on air entrainment at RE= %d',RE);
title(title1)
```

```
figure(16)
plot(Xnorm,mar1)
hold on
plot(Xnorm,mar2)
hold on
plot(Xnorm,mar3)
hold off
legend(legend1,legend2,legend3,'location','northwest')
legend('boxoff')
xlabel('x/d')
ylabel('Mair/Mfuel')
title1=sprintf('Effect of spread angle on air entrainment ratio at RE= %d',RE);
title(title1)
```

```
figure(17)
plot(Xnorm(k:end),totalp1(k:end))
hold on
plot(Xnorm(k:end),totalp2(k:end))
hold on
plot(Xnorm(k:end),totalp3(k:end))
hold off
legend(legend1,legend2,legend3,'location','northeast')
```

`

```
legend('boxoff')
xlabel('x/d')
ylabel('Pressure (N)')
title1=sprintf('Effect of spread angle on total pressure at RE= %d',RE);
title(title1)
```

```
figure(18)
plot(Xnorm(k:end),staticp1(k:end))
hold on
plot(Xnorm(k:end),staticp2(k:end))
hold on
plot(Xnorm(k:end),staticp3(k:end))
hold off
legend(legend1,legend2,legend3,'location','northeast')
legend('boxoff')
xlabel('x/d')
ylabel('Pressure (N)')
title1=sprintf('Effect of spread angle on static pressure at RE= %d',RE);
title(title1)
```

```
figure(19)
plot(Xnorm(k:end),dynamicp(1,k:end))
hold on
plot(Xnorm(k:end),dynamicp(2,k:end))
hold on
plot(Xnorm(k:end),dynamicp(3,k:end))
hold off
legend(legend1,legend2,legend3,'location','northeast')
legend('boxoff')
xlabel('x/d')
ylabel('Pressure (N)')
title1=sprintf('Effect of spread angle on dynamic pressure at RE= %d',RE);
title(title1)
```

```
figure(20)
Pcoef1=totalp1(1:end)./totalp1(k);
Pcoef2=totalp2(1:end)./totalp2(k);
Pcoef3=totalp3(1:end)./totalp3(k);

plot(Xnorm(k:end),Pcoef1(k:end))
hold on
plot(Xnorm(k:end),Pcoef2(k:end))
hold on
plot(Xnorm(k:end),Pcoef3(k:end))
hold off
legend(legend1,legend2,legend3,'location','northeast')
legend('boxoff')
xlabel('x/d')
ylabel('Pressure loss coeficient')
title1=sprintf('Effect of spread angle on pressure loss at RE= %d',RE);
title(title1)

figure(21)
Ax1=Am(1,end);                 % cross- sectional area of tube at exit
XX=linspace(0.5,3,np);         % Create 50 partitions from 0.5 to 2
```

`

```
AXX=Ax1.*XX;                 % compute the port area assuming they ranged
%between 0.5 to 2 of the crossectional area of the tube exit
QA= (q*(rhoa - rhof) + (q^2*(rhoa - rhof)^2 + (4*AXX*rhoa*rhof*q^2)/Af).^(1/2))/(2*rhoa);
VA=QA./AXX;                  % velocity of the mixture at the ports
mair=(QA-q)*rhoa;            % mass of air entrained
mR=mair/mm;                  % air/fuel ratio by mass
plot(AXX/Ax1,(mR/AFR)*100)   % plot the variation of air/fuel wrt to port area
hold on
```

```
Ax2=Am(2,end);               % cross- sectional area of tube at exit
XX=linspace(0.5,3,np);       % Create 50 partitions from 0.5 to 2
AXX2=Ax2.*XX;                % compute the port area assuming they ranged
%between 0.5 to 2 of the crossectional area of the tube exit
QA2= (q*(rhoa - rhof) + (q^2*(rhoa - rhof)^2 + (4*AXX2*rhoa*rhof*q^2)/Af).^(1/2))/(2*rhoa);
VA2=QA2./AXX2;               % velocity of the mixture at the ports
mair2=(QA2-q)*rhoa;          % mass of air entrained
mR2=mair2/mm;                % air/fuel ratio by mass
plot(AXX2/Ax2,(mR2/AFR)*100) % plot the variation of air/fuel wrt to port area
hold on
```

```
Ax3=Am(3,end);               % cross- sectional area of tube at exit
XX=linspace(0.5,3,np);       % Create 50 partitions from 0.5 to 2
AXX3=Ax3.*XX;                % compute the port area assuming they ranged
%between 0.5 to 2 of the crossectional area of the tube exit
QA3= (q*(rhoa - rhof) + (q^2*(rhoa - rhof)^2 + (4*AXX3*rhoa*rhof*q^2)/Af).^(1/2))/(2*rhoa);
VA3=QA3./AXX3;               % velocity of the mixture at the ports
mair3=(QA3-q)*rhoa;          % mass of air entrained
mR3=mair3/mm;                % air/fuel ratio by mass
plot(AXX3/Ax3,(mR3/AFR)*100) % plot the variation of air/fuel wrt to port area
hold off
```

Published with MATLAB® R2015a

Appendix II Code for computing the flame speed and adiabatic temperature

```
%--------------------------------------------------------------------%
%             Adiabatic Flame Temperature Computation of LPG
%--------------------------------------------------------------------%

%INTRODUCTORY STATEMENT
```

This code computes the adiabatic flame temperature of LPG. LPG consists of Propane and Butane and some traces of Methane. It prompts the user to key in certain parameters which are required to carry out the computations the parameters include: The mole fraction of PROPANE The mole fraction of BUTHANE The mole fraction of METHANE Percentage excess air (ms) Initial temperature of the reactants (T1)

```
clear
clc
disp('PLEASE READ THE FOLLOWING INSTRUCTIONS');
disp('This code was written to compute the combustion parameters of LPG');
disp('The asumption is that LPG consists of propane and butane in different proportions');
disp('The second assumption is that there may be traces of methane in the gas which may');
disp('or may not affect the combustion properties of the fuel depending on the mole fraction');
disp('in entering the fuel parameters, PROPANE comes first followed by BUTANE and METHANE');
disp('and the sum of the mole fraction of the fuel species must be equal to one');
disp('---------------------------------------------------------------------------------');
disp('---------------------------------------------------------------------------------');
fprintf('\n');
```

```
PLEASE READ THE FOLLOWING INSTRUCTIONS
This code was written to compute the combustion parameters of LPG
The asumption is that LPG consists of propane and butane in different proportions
The second assumption is that there may be traces of methane in the gas which may
or may not affect the combustion properties of the fuel depending on the mole fraction
in entering the fuel parameters, PROPANE comes first followed by BUTANE and METHANE
and the sum of the mole fraction of the fuel species must be equal to one
---------------------------------------------------------------------------------
---------------------------------------------------------------------------------
```

INPUT DATA

```
filename=input('Enter in BLOCK LETTERS the title of the analysis:','s');

mole_propane= input('Enter the mole fraction of PROPANE in the fuel;    ');
disp('---------------------------------------------------------------------------------');
fprintf('\n');

mole_butane= input('Enter the mole fraction of BUTANE in the fuel;      ');
disp('---------------------------------------------------------------------------------');
fprintf('\n');
```

`

```
mole_methane= input('Enter the mole fraction of METHANE in the fuel;    ');
disp('-----------------------------------------------------------------------------------');
fprintf('\n');

ms=input('Enter the PERCENTAGE EXCESS AIR;                              ');
disp('-----------------------------------------------------------------------------------');
fprintf('\n');

T1=input('Enter the initial TEMPERATURE OF THE REACTANTS;               ');
disp('-----------------------------------------------------------------------------------');
fprintf('\n');
```

COMPUTATION PROCEDURE

```
mole_ratio=[mole_propane,mole_butane,mole_methane];
carbon=[3,4,1];          % carbon content of propane, butane and methane
hydrogen=[8,10,4];       % hdrogen content of propane, butane and methane
oxygen=[0,0,0];          % oxygen content of the fuel
T0=298.15;               % Referrence temperature
T2=1300;                 % initial guess temperature
E=-2;                    % initial enthalpy of combustion
j=1;
T=zeros(1,j);
ee=zeros(1,j);
while E<0
    T2=T2+20;
% Composition of the reactants
Equivalence_ratio=1/(ms+1);                % compute the equivalence ratio
T_carbon=sum(dot(carbon,mole_ratio));      % compute the total moles of carbon in the fuel
T_oxygen=sum(dot(oxygen,mole_ratio));      % compute the total moles of oxygen in the fuel
T_hydrogen=sum(dot(hydrogen,mole_ratio));  % compute the total moles of hydrogen in the fuel
T_mole=sum(mole_ratio);
molarm_air=28.96;                           % molar mass of air

khc=10^dissk_hydrocarbon(T2);
kh2o= 10^dissk_h2o(T2);
kco2=10^dissk_co2(T2);


phi=Equivalence_ratio;
m=T_carbon;
n=T_hydrogen;
z=T_oxygen;
ka=m+(n/4)-(z/2);     % no of moles of oxygen
c=(ka/phi)*(79/21);   % no of moles of nitrogen
p=1.01325;
R=8.3145; %KJ/Kmol*K

mole_air=(ka/phi)*(1+(79/21));
mass_air=mole_air*molarm_air;
```

`

```
Nmole_reactant=1+(ka/phi)+(79/21)*(ka/phi);
%PV=nRT
V1=(Nmole_reactant*R*T1)/(1.01325*10^5);
V2=(V1*T2)/T1;
ratiop2_n2=p*V1*T2/(Nmole_reactant*V2*T1);



if ms<0
    syms a b d e real
    f=0;
    eqn=[a+d==m,2*b+2*e==n,2*a+b+d==2*ka/phi,b*d/e*a==khc];
    [a,b,d,e]= solve(eqn);
   a=double(a);b=double(b); d=double(d);e=double(e);

if m>1

for i=1:length(a);
d=real(d);
a=real(a);
if (a(i)<m && a(i)>=1)
a1=a(i);
w=i;
d=d(w);
%d=m-a1;
end
end

else
for i=1:length(a);
d=real(d);
a=real(a);
if (a(i)<m && a(i)>=0)
a1=a(i);
w=i;
%d=d(w);
d=m-a1;
end
end
end

 for i=1:length(b);
 b=real(b);
 e=real(e);
if b(i)>0 && b(i)<n/2;
 b1=b(i);
 w=i;
 %e=e(w);
 e=n-b1;
end
 end


    nt=a1+b1+c+d+e+f;
```

`

```
else
    syms b e f real
    a=m;
    b=n/2;
    d=0;
    e=0;
    f=(ka/phi)-ka;
    %eqn=[2*b+2*e==n,2*a+b+2*f-z==2*(ka/phi),(b/(e*f^0.5))*(1/ratiop2_n2)^0.5==kh2o];
    %[b,e,f]= solve(eqn);
    b=double(b); e=double(e); f=double(f);
    nt=a+b+c+d+e+f;
end


mass_of_fuel=12*m+1*n+z*16;
AFR=mass_air/mass_of_fuel;
%REACTANT0
cp_propane0=cp_propane(T0);
cp_butane0=cp_butane(T0);
cp_methane0=cp_methane(T0);

%REACTANT1

cp_propane1=cp_propane(T1);
cp_butane1=cp_butane(T1);
cp_methane1=cp_methane(T1);

ho21= enthalpyo2(T1);
hn21=enthalpyn2(T1);

%PRODUCT0

hco20=enthalpyco2(T0);
hh2o0=enthalpyh2o(T0);
hn20=enthalpyn2(T0);
hco0= enthalpyco(T0);
hh20=enthalpyh2(T0);
ho20= enthalpyo2(T0);

%PRODUCT2

hco22=enthalpyco2(T2);
hh2o2=enthalpyh2o(T2);
hn22=enthalpyn2(T2);
hco2= enthalpyco(T2);
hh22=enthalpyh2(T2);
ho22= enthalpyo2(T2);

%heat of formation

hf_propane=-102900;
hf_butane=-126150;
hf_methane=-74870;

hf_O2=0;
hf_H2O=-241830;
```

`

```
hf_CO2=-393520;
hf_CO=-110530;


cp_fuel0=[cp_propane0,cp_butane0,cp_methane0];
cp_fuel1=[cp_propane1,cp_butane1,cp_methane1];


HR0= sum(dot(mole_ratio,cp_fuel0))*T0+(ka/phi)*ho20+c*hn20;
HR1= sum(dot(mole_ratio,cp_fuel1))*T1+(ka/phi)*ho21 +c*hn21;
```

Compute the standard enthalpy of combustion of fuel when the mixture is fuel rich

```
if ms <0
    DH0_propane=(a1*hf_CO2+b1*hf_H2O+d*hf_CO)-hf_propane;
    DH0_butane=(a1*hf_CO2+b1*hf_H2O+d*hf_CO)-hf_butane;
    DH0_methane=(a1*hf_CO2+b1*hf_H2O+d*hf_CO)-hf_methane;

    DH0=[DH0_propane,DH0_butane,DH0_methane];
    DH0_sum=sum(dot(mole_ratio,DH0));

HP0=(a1*hco20)+ (b1*hh2o0)+ c*hn20 +d*hco0 + e*hh20 + f*ho20;
HP2=(a1*hco22)+ (b1*hh2o2)+ c*hn22 +d*hco2 + e*hh22 + f*ho22;
```

Compute the standard enthalpy of combustion of fuel when the mixture is lean or at stoichiometric value

```
else
    DH0_propane=(a*hf_CO2+b*hf_H2O+d*hf_CO)-hf_propane;
    DH0_butane=(a*hf_CO2+b*hf_H2O+d*hf_CO)-hf_butane;
    DH0_methane=(a*hf_CO2+b*hf_H2O+d*hf_CO)-hf_methane;

    DH0=[DH0_propane,DH0_butane,DH0_methane];
    DH0_sum=sum(dot(mole_ratio,DH0));
    HP0=(a*hco20)+ (b*hh2o0)+ c*hn20 +d*hco0 + e*hh20 + f*ho20;
    HP2=(a*hco22)+ (b*hh2o2)+ c*hn22 +d*hco2 + e*hh22 + f*ho22;
end
```

Compute the heat released in the cause of the combustion

```
E=(HR0-HR1)+DH0_sum+(HP2-HP0);


ee(j)=E;
T(j)=T2;
fprintf('%1.8f\n',ee(j))
j=j+1;
plot(T,ee,'r*')
```

`

```
shg
pause(0.2)

end
ep=length(ee);
Tp=length(T);
Tadiabatic=((0-ee(ep-1))/(ee(ep)-ee(ep-1)))*(T(Tp)-T(Tp-1))+T(Tp-1);


n_initial=1/(82.05*Tadiabatic);
n_propane=(n_initial)/(Nmole_reactant);
n_butane=(n_initial)/(Nmole_reactant);
n_methane=(n_initial)/(Nmole_reactant);

air_propane=n_propane*mole_air;
air_butane=n_butane*mole_air;
air_methane=n_methane*mole_air;

A_propane=1.56*10^10;
A_butane=3.0*10^10;
A_methane=4.6*10^4;

a_propane=0.1;
b_propane=1.65;

a_butane=0.15;
b_butane=1.6;

a_methane=-0.3;
b_methane=1.3;

E_propane=30*1000;%Cal/mol
E_butane=30*1000; %Cal/mol
E_methane=30*1000; %Cal/mol


K_propane1=thermalK_propane(T1);
K_butane1=thermalK_butane(T1);
K_methane1=thermalK_methane(T1);

rho_propane1=density_propane(T1);
rho_butane1=density_butane(T1);
rho_methane1=density_methane(T1);
Rrho_fuel=[rho_propane1,rho_butane1,rho_methane1];
rho_fuel=0.001*sum(dot(mole_ratio,Rrho_fuel));

thermal_diffpropane1=10000*(K_propane1)/(rho_propane1*cp_propane1/0.044);
thermal_diffbutane1=10000*(K_butane1)/(rho_butane1*cp_butane1/0.058);
thermal_diffmethane1=10000*(K_methane1)/(rho_methane1*cp_methane1/0.016);
tthermal_diff=[thermal_diffpropane1,thermal_diffbutane1,thermal_diffmethane1];
thermal_diff=sum(dot(mole_ratio,tthermal_diff));


Zeldovich_number=(Tadiabatic^2)/(Tadiabatic-T1)*(1.987/E_butane);
```

`

```
r_propane=A_propane*exp(-
E_propane/(1.987*Tadiabatic))*(n_propane^a_propane)*(air_propane^b_propane);
r_butane=A_butane*exp(-E_butane/(1.987*Tadiabatic))*(n_butane^a_butane)*(air_butane^b_butane);
r_methane=A_methane*exp(-
E_methane/(1.987*Tadiabatic))*(n_methane^a_methane)*(air_methane^b_methane);


        if mole_ratio(1)==1;
            r_reaction=(r_propane);
             SL=((r_reaction*thermal_diff)/(rho_fuel*Zeldovich_number))^0.5;

        else
            if mole_ratio(3)==1;
                r_reaction=(r_methane);
                SL=((r_reaction*thermal_diff)/(rho_fuel*Zeldovich_number))^0.5;
            else
                r_reaction=(r_butane);
                SL=((r_reaction*thermal_diff)/(rho_fuel*Zeldovich_number))^0.5;
            end
        end


flame_thickness=thermal_diff/SL;
flashback_gradient=SL/flame_thickness;
```

Published with MATLAB® R2015a

`

Appendix III Density Interpolation Functions

```
function kk=density_propane(x)
```

BACKGROUND INFORMATION

```
%This function calculates the DENSITY OF PROPANE Kg/m3
%when the temperature x in kelvin is given
% THE SYNTAX FOR THE FUNCTION IS;
% k=thermalK_propane(x);
% where K is the DENSITY OF METHANE at 1 bar and x temperature
% the data set used for this computation are from https://www.engineeringtoolbox.com
```

DATA SET

```
T=[231,248,263,268,273,278,298,303,323,348,373,398,423,448,473,523,573,623,673,773];
density=[2.38,2.205,2.069,2.028,1.988,1.949,1.809,1.777,1.661,1.537,1.432,1.341,1.262,1.192,1.129
,1.019,0.927,0.85,0.786,0.688];
```

INTERPOLATION FUNCTION

```
a=[T;density];
a=a';
[r ,c]=size(a);
for i=1:r;
    for j=1:c;
    if a(i,1)==x;
        k=i;
        kk=a(k,2);
    else
        if a(i,1)<x;
        k=i;
        lower_x=a(k,1);
        upper_x=a(k+1,1);
        lower_e=a(k,2);
        upper_e=a(k+1,2);
        kk=((x-lower_x)/(upper_x-lower_x))*(upper_e-lower_e)+lower_e;
        end

    end
    end
end
```

Published with MATLAB® R2015a

`

```
function kk=density_methane(x)
```

BACKGROUND INFORMATION

```
%This function calculates the DENSITY OF METHANE Kg/m3
%when the temperature x in kelvin is given
% THE SYNTAX FOR THE FUNCTION IS;
% k=thermalK_methane(x);
% where K is the DENSITY OF METHANE at 1 bar and x temperature
% the data set used for this computation are from https://www.engineeringtoolbox.com
```

DATA SET

```
T=[283,293,303,323,348,373,398,423,448,473,523,573,623,673,773];
K=[0.683,0.66,0.638,0.598,0.555,0.518,0.485,0.456,0.431,0.408,0.369,0.337,0.31,0.287,0.25];
```

```
%INTERPOLATION CODE
```

```
a=[T;K];
a=a';
[r ,c]=size(a);
for i=1:r;
    for j=1:c;
    if a(i,1)==x;
        k=i;
        kk=a(k,2);
    else
        if a(i,1)<x;
        k=i;
        lower_x=a(k,1);
        upper_x=a(k+1,1);
        lower_e=a(k,2);
        upper_e=a(k+1,2);
        kk=((x-lower_x)/(upper_x-lower_x))*(upper_e-lower_e)+lower_e;
        end

    end
    end
end
```

Published with MATLAB® R2015a

`

```
function kk=density_butane(x)
```

BACKGROUND INFORMATION

```
%This function calculates the density of butane at 1 bar in Kg/m3
%when the temperature x in kelvin is known
% THE SYNTAX FOR THE FUNCTION IS;
% k=density_butane(x);
% where K is the density of butane at 1 bar
% the data set used for this computation are from https://www.engineeringtoolbox.com
```

DATA SET

```
T=[283,293,303,323,348,373,398,423,448,473,523];
density=[2.561,2.464,2.374,2.214,2.044,1.9,1.776,1.668,1.572,1.487,1.342];
```

INTERPOLATION CODE

```
a=[T;density];
a=a';
[r ,c]=size(a);
for i=1:r;
    for j=1:c;
    if a(i,1)==x;
        k=i;
        kk=a(k,2);
    else
        if a(i,1)<x;
        k=i;
        lower_x=a(k,1);
        upper_x=a(k+1,1);
        lower_e=a(k,2);
        upper_e=a(k+1,2);
        kk=((x-lower_x)/(upper_x-lower_x))*(upper_e-lower_e)+lower_e;
        end

    end
    end
end
```

Published with MATLAB® R2015a

`

```
function kk=density_air(x)
```

```
%BACKGROUND INFORMATION
```

```
%This function calculates the density of air in
%Kg/m^3
%when the temperature x in kelvin is known
% THE SYNTAX FOR THE FUNCTION IS;
% KK=density_air(x);
% where K is the DENSITY OF AIR
% the data set used for this computation are from https://www.engineeringtoolbox.com
```

DATA SET

```
T=[0,5,10,15,20,30,40,50,60,80,100,200,300,400,500,600,700,800,900,1000];
air_density=[1.292,1.268,1.246,1.225,1.204,1.164,1.127,1.093,1.06,1,0.9467,0.7451,0.6168,0.5238,0
.4567,0.4043,0.3626,0.3289,0.3009,0.2773];
```

INTERPOLATION CODE

```
a=[T;air_density];
a=a';
[r ,c]=size(a);
for i=1:r;
    for j=1:c;
    if a(i,1)==x;
        k=i;
        kk=a(k,2);
    else
        if a(i,1)<x;
        k=i;
        lower_x=a(k,1);
        upper_x=a(k+1,1);
        lower_e=a(k,2);
        upper_e=a(k+1,2);
        kk=((x-lower_x)/(upper_x-lower_x))*(upper_e-lower_e)+lower_e;
        end

    end
    end
end
```

Published with MATLAB® R2015a

`

Appendix IV Enthalpy Interpolation Function

```
function e=enthalpyoh(x)
```

BACKGROUND INFORMATION

This function calculates the enthalpy of OH when given the temperature x in kelvin THE SYNTAX FOR THE FUNCTION IS; H=enthalpyoh(x); where H is the enthalpy. The unit of the enthalpy is in KJ/KMOL. The data set used for the computation are those given in THERMODYNAMICS AND TRANSPORT PROPERTIES OF FLUID SI UNITS COMPILED BY G.F.C. ROGERS AND Y.R.MAYHEW

DATA SET

```
t=[0;100;200;298.150000000000;300;400;600;800;1000;1200;1400;1600;1800;2000;2200;2400;2600;2800;3
000;3200;3400;3600;3800;4000];
u=[-9171;-6138;-
2975;0;54;3033;8941;14878;20933;27158;33568;40150;46890;53760;60752;67839;75015;82266;89584;96960
;10439;111860;119380;126940];
```

INTERPLOATION CODE

```
a=[t,u];
[r ,c]=size(a);
for i=1:r;
    for j=1:c;
    if a(i,1)==x;
        k=i;
        e=a(k,2);
    else
        if a(i,1)<x;
        k=i;
        lower_x=a(k,1);
        upper_x=a(k+1,1);
        lower_e=a(k,2);
        upper_e=a(k+1,2);
        e=((x-lower_x)/(upper_x-lower_x))*(upper_e-lower_e)+lower_e;
        end

    end
    end
end
```

Published with MATLAB® R2015a

`

```
function e=enthalpyo2(x)
```

BACKGROUND INFORMATION

This function calculates the enthalpy of O2 when given the temperature x in kelvin THE SYNTAX FOR THE FUNCTION IS; H=enthalpyo2(x); where H is the enthalpy. The unit of the enthalpy is in KJ/KMOL. The data set used for the computation are those given in THERMODYNAMICS AND TRANSPORT PROPERTIES OF FLUID SI UNITS COMPILED BY G.F.C. ROGERS AND Y.R.MAYHEW

DATA SET

```
t=[0;100;200;298.150000000000;300;400;600;800;1000;1200;1400;1600;1800;2000;2200;2400;2600;2800;3
000;3200;3400;3600;3800;4000];
u=[-8682;-5778;-
2866;0;54;3029;9247;15841;22707;29765;36966;44279;51689;59199;66802;74492;82274;90144;98098;10613
0;114230;122400;130630;138910];
```

```
%INTERPOLATION CODE
```

```
a=[t,u];
[r ,c]=size(a);
for i=1:r;
    for j=1:c;
    if a(i,1)==x;
        k=i;
        e=a(k,2);
    else
        if a(i,1)<x;
        k=i;
        lower_x=a(k,1);
        upper_x=a(k+1,1);
        lower_e=a(k,2);
        upper_e=a(k+1,2);
        e=((x-lower_x)/(upper_x-lower_x))*(upper_e-lower_e)+lower_e;
        end

    end
    end
end
```

Published with MATLAB® R2015a

`

```
function e=enthalpyn2(x)
```

BACKGROUND INFORMATION

This function calculates the enthalpy of N2 when given the temperature x in kelvin THE SYNTAX FOR THE FUNCTION IS; H=enthalpyn2(x); where H is the enthalpy. The unit of the enthalpy is in KJ/KMOL. The data set used for the computation are those given in THERMODYNAMICS AND TRANSPORT PROPERTIES OF FLUID SI UNITS COMPILED BY G.F.C. ROGERS AND Y.R.MAYHEW

```
% DATA SET
```

```
t=[0;100;200;298.150000000000;300;400;600;800;1000;1200;1400;1600;1800;2000;2200;2400;2600;2800;3
000;3200;3400;3600;3800;4000];
u=[-8669;-5770;-
2858;0;54;2971;8891;15046;21460;28108;34936;41903;48982;56141;63371;70651;77981;85345;92738;10016
0;107610;115080;122570;130080];
```

```
%INTERPLOATION CODE
```

```
a=[t,u];
[r ,c]=size(a);
for i=1:r;
    for j=1:c;
    if a(i,1)==x;
        k=i;
        e=a(k,2);
    else
        if a(i,1)<x;
        k=i;
        lower_x=a(k,1);
        upper_x=a(k+1,1);
        lower_e=a(k,2);
        upper_e=a(k+1,2);
        e=((x-lower_x)/(upper_x-lower_x))*(upper_e-lower_e)+lower_e;
        end

    end
    end
end
```

Published with MATLAB® R2015a

`

```
function e=enthalpyh2o(x)
```

BACKGROUND INFORMATION

This function calculates the enthalpy of H2O when given the temperature x in kelvin THE SYNTAX FOR THE FUNCTION IS; e=enthalpyh2o(x); where H is the enthalpy. The unit of the enthalpy is in KJ/KMOL. The data set used for the computation are those given in THERMODYNAMICS AND TRANSPORT PROPERTIES OF FLUID SI UNITS COMPILED BY G.F.C. ROGERS AND Y.R.MAYHEW

DATA SET

```
t=[0;100;200;298.150000000000;300;400;600;800;1000;1200;1400;1600;1800;2000;2200;2400;2600;2800;3
000;3200;3400;3600;3800;4000];
u=[-9904;-6615;-
3280;0;63;3452;10498;17991;25978;34476;43447;52844;62609;72689;83036;93604;4370;115290;126360;137
550;148850;160250;171720;183280];
```

INTERPOLATION CODE

```
a=[t,u];
[r ,c]=size(a);
for i=1:r;
    for j=1:c;
    if a(i,1)==x;
        k=i;
        e=a(k,2);
    else
        if a(i,1)<x;
        k=i;
        lower_x=a(k,1);
        upper_x=a(k+1,1);
        lower_e=a(k,2);
        upper_e=a(k+1,2);
        e=((x-lower_x)/(upper_x-lower_x))*(upper_e-lower_e)+lower_e;
        end

    end
    end
end
```

Published with MATLAB® R2015a

`

```
function e=enthalpyh2(x)
```

BACKGROUND INFORMATION

This function calculates the enthalpy of H2 when given the temperature x in kelvin THE SYNTAX FOR THE FUNCTION IS; H=enthalpyh2(x); where H is the enthalpy. The unit of the enthalpy is in KJ/KMOL. The data set used for the computation are those given in THERMODYNAMICS AND TRANSPORT PROPERTIES OF FLUID SI UNITS COMPILED BY G.F.C. ROGERS AND Y.R.MAYHEW

DATA SET

```
t=[0;100;200;298.150000000000;300;400;600;800;1000;1200;1400;1600;1800;2000;2200;2400;2600;2800;3
000;3200;3400;3600;3800;4000];
u=[-8468;-5293;-
2770;0;54;2958;8812;14703;20686;26794;33062;39522;46150;52932;59860;66915;74090;81370;88743;96199
;103740;111360;119060;126850];
```

```
%INTERPOLATION CODE
```

```
a=[t,u];
[r ,c]=size(a);
for i=1:r;
    for j=1:c;
    if a(i,1)==x;
        k=i;
        e=a(k,2);
    else
        if a(i,1)<x;
        k=i;
        lower_x=a(k,1);
        upper_x=a(k+1,1);
        lower_e=a(k,2);
        upper_e=a(k+1,2);
        e=((x-lower_x)/(upper_x-lower_x))*(upper_e-lower_e)+lower_e;
        end

    end
    end
end
```

Published with MATLAB® R2015a

`

```
function e=enthalpyco2(x)
```

BACKGROUND INFORMATION

This function calculates the enthalpy of CO2 when given the temperature x THE SYNTAX FOR THE FUNCTION IS; H=enthalpyco2(x); where H is the enthalpy. The unit of the temperature is in kelvin while the internal energy is in KJ/KMOL. The data set used for this computation are those given in THERMODYNAMICS AND TRANSPORT PROPERTIES OF FLUID SI UNITS COMPILED BY G.F.C. ROGERS AND Y.R.MAYHEW

DATA SET

```
t=[0;100;200;298.150000000000;300;400;600;800;1000;1200;1400;1600;1800;2000;2200;2400;2600;2800;3
000;3200;3400;3600;3800;4000];
u=[-9364;-6456;-
3414;0;67;4008;12916;22815;33405;44484;55907;67580;79442;91450;103570;115790;128080;140440;152860
;165330;177850;190410;203000;215630];
```

```
% INTERPLOATION CODE
a=[t,u];
[r ,c]=size(a);
for i=1:r;
    for j=1:c;
    if a(i,1)==x;
        k=i;
        e=a(k,2);
    else
        if a(i,1)<x;
        k=i;
        lower_x=a(k,1);
        upper_x=a(k+1,1);
        lower_e=a(k,2);
        upper_e=a(k+1,2);
        e=((x-lower_x)/(upper_x-lower_x))*(upper_e-lower_e)+lower_e;
        end

    end
    end
end
```

Published with MATLAB® R2015a

`

```
function e=enthalpyco(x)
```

```
% This function calculates the enthalpy of CO when given the
% temperature x in kelvin
% THE SYNTAX FOR THE FUNCTION IS;
% H=enthalpyco(x);
% where H is the enthalpy
% The unit of the enthalpy is in KJ/KMOL.
% the data set used for the computation are those given in THERMODYNAMICS
% AND TRANSPORT PROPERTIES OF FLUID SI UNITS COMPILED BY G.F.C. ROGERS AND
% Y.R.MAYHEW
```

```
%DATA SET
t=[0;100;200;298.150000000000;300;400;600;800;1000;1200;1400;1600;1800;2000;2200;2400;2600;2800;3
000;3200;3400;3600;3800;4000];
u=[-8699;-5770;-
2858;0;54;2975;10196;15175;21686;28426;35338;42384;49522;56739;64019;71346;78714;86115;93542;1010
00;108480;115980;123490;131030];
```

```
%INTERPLOATION CODE

a=[t,u];
[r ,c]=size(a);
for i=1:r;
    for j=1:c;
    if a(i,1)==x;
        k=i;
        e=a(k,2);
    else
        if a(i,1)<x;
        k=i;
        lower_x=a(k,1);
        upper_x=a(k+1,1);
        lower_e=a(k,2);
        upper_e=a(k+1,2);
        e=((x-lower_x)/(upper_x-lower_x))*(upper_e-lower_e)+lower_e;
        end

    end
    end
end
```

Published with MATLAB® R2015a

`

Appendix V Enthalpy of Formation computation code

```
function hfr= enthalpy_formation(nc,nh,no)
```

```
%BACKGROUND INFORMATION
```

The function hfr= enthalpy_formation(nc,nh,no) takes the input nc, nh and no and computes hfr the enthalpy of formation of hydrocarbons or reactant. The result compares well with experimental results from literature for alkanes for a generic hydrocarbon CaHbOc the following formulae were applied in the computation DHa(298k)=a*DHf(C,g)+b*DHf(H,g)+c*DHf(O,g)-DHf(CaHbOc,g); DHa=sum([(b-c)*B_HC, (a-1)*B_CC, c*B_CO, c*B_OH])

DEFINITION OF TERMS

DHf(C,g)=change in formation enthalpy of carbon in gaseous state (g) DHf(H,g)=change in formation enthalpy of hydrogen in gaseous state DHf(O,g)=change in formation enthalpy of oxygen in gaseous state DHf(CaHbOc,g)=change in formation enthalpy of the hydrocarbon in gaseous state DHa=change in atomisation energy the hydrocarbon

```
% B_HC=the dissociation energy of H-C bond
% B_CC=the dissociation energy of C-C bond
% B_CO=the dissociation energy of C-O bond
% B_OH=the dissociation energy of O-H bond
% a=nc; the number of carbon atoms in the hydrocarbon
% b=nh; the number of hydrogen atoms in the hydrocarbon
% c=no; the number of oxygen atoms in the hydrocarbon
```

COMPUTATION PROCESS

```
B_HC=(nh-no)*413363;
B_CC=(nc-1)*345202;
B_CO=no*358000;
B_OH=no*463000;

CF=714990*nc;
HF=217998*nh;
OF=249170*no;

DHa=sum([B_HC B_CC B_CO B_OH]);
IEF=sum([CF HF OF]);
hfr=-(DHa-IEF);
```

Published with MATLAB® R2015a

`

Appendix VI Dissociation constant computation code

```
function k=dissk_hydrocarbon(x)
```

BACK GROUND INFORMATION

```
%This function calculates the dissociation constant of HYDROCARBON in log form when given the
% temperature x in kelvin
% THE SYNTAX FOR THE FUNCTION IS;
% K=dissk_hydrocarbon(x);
% where k is the log of dissociation constant to base 10
% the data set used for this computation are those given in THERMODYNAMICS
% AND TRANSPORT PROPERTIES OF FLUID SI UNITS COMPILED BY G.F.C. ROGERS AND
% Y.R.MAYHEW
```

COMPUTATION PROCESS

```
k1=dissk_h2o(x);
k2=dissk_co2(x);
k=k1-k2;
```

Published with MATLAB® R2015a

`

```
function kk=dissk_h2o(x)
```

BACKGROUND INFORMATION

```
%This function calculates the dissociation constant of H2O in log form when given the
% temperature x in kelvin
% THE SYNTAX FOR THE FUNCTION IS;
% K=dissk_h2o(x);
% where k is the log of dissociation constant to base 10
% the data set used for this computation are those given in THERMODYNAMICS
% AND TRANSPORT PROPERTIES OF FLUID SI UNITS COMPILED BY G.F.C. ROGERS AND
% Y.R.MAYHEW
```

DATA SET

```
T=[289.150000000000,300,400,600,800,1000,1200,1400,1600,1800,2000,2200,2400,2600,2800,3000,3200,3
400,3600,3800,4000,4500,5000,5500,6000];
KH2O=[40.0480000000000,39.7860000000000,29.2400000000000,18.6330000000000,13.2890000000000,10.062
0000000000,7.89900000000000,6.34700000000000,5.18000000000000,4.27000000000000,3.54000000000000,2
.94200000000000,2.44320000000000,2.02100000000000,1.65800000000000,1.34300000000000,1.06700000000
000,0.824000000000000,0.607000000000000,0.413000000000000,0.238000000000000,-0.133000000000000,-
0.430000000000000,-0.675000000000000,-0.880000000000000];
```

INTERPOLATION CODE

```
a=[T;KH2O];
a=a';
[r ,c]=size(a);
for i=1:r;
    for j=1:c;
    if a(i,1)==x;
        k=i;
        kk=a(k,2);
    else
        if a(i,1)<x;
        k=i;
        lower_x=a(k,1);
        upper_x=a(k+1,1);
        lower_e=a(k,2);
        upper_e=a(k+1,2);
        kk=((x-lower_x)/(upper_x-lower_x))*(upper_e-lower_e)+lower_e;
        end

    end
    end
end
```

`

Published with MATLAB® R2015a

`

```
function kk=dissk_co2(x)
```

BACKGROUND INFORMATION

```
%This function calculates the dissociation constant of CO2 in log form when given the
% temperature x in kelvin
% THE SYNTAX FOR THE FUNCTION IS;
% K=dissk_co2(x);
% where K is the log of dissociation constant to base 10
% the data set used for this computation are those given in THERMODYNAMICS
% AND TRANSPORT PROPERTIES OF FLUID SI UNITS COMPILED BY G.F.C. ROGERS AND
% Y.R.MAYHEW
```

DATA SET

```
T=[289.150000000000,300,400,600,800,1000,1200,1400,1600,1800,2000,2200,2400,2600,2800,3000,3200,3
400,3600,3800,4000,4500,5000,5500,6000];
KCO2=[45.0600000000000,44.7600000000000,32.4310000000000,20.0870000000000,13.9160000000000,10.221
0000000000,7.76400000000000,6.01400000000000,4.70600000000000,3.69300000000000,2.88400000000000,2
.22600000000000,1.67900000000000,1.21900000000000,0.825000000000000,0.485000000000000,0.189000000
000000,-0.0710000000000000,-0.302000000000000,-0.508000000000000,-0.692000000000000,-
1.07900000000000,-1.38600000000000,-1.63500000000000,-1.84100000000000];
```

INTERPLOATION CODE

```
a=[T;KCO2];
a=a';
[r ,c]=size(a);
for i=1:r;
    for j=1:c;
    if a(i,1)==x;
        k=i;
        kk=a(k,2);
    else
        if a(i,1)<x;
        k=i;
        lower_x=a(k,1);
        upper_x=a(k+1,1);
        lower_e=a(k,2);
        upper_e=a(k+1,2);
        kk=((x-lower_x)/(upper_x-lower_x))*(upper_e-lower_e)+lower_e;
        end

    end
    end
end
```

`

Published with MATLAB® R2015a

`

Appendix VII Combustion Product Computation function

```
function [nco2,nco,nh2o,nh2,no2,nn2]=dissf_hydrocarbon(t,p,nc,nh,nro2)
```

BACKGROUND INFORMATION

This function;[nco2,nco,nh2o,nh2,no2,nn2]=dissf_hydrocarbon(t,p,nc,nh,nro2) computes the number of moles of CO2, CO, H2 H2O, O2 and N2 in the combustion products of hydrocarbons taking into consideration the effect of dissociation; The arguments to the function are; t-the temperature at which the combustion takes place p-the pressure at which the combustion takes place nc-the number of carbon atoms in one mole of the hydrocarbon nh=the number of hydrogen atoms in one mole of the hydrocarbon nro2=the number of moles of air oxygen that is involved in the reaction

COMPUTATION PROCESS

```
syms a b                                  % Define a and b as symbolic variables
nco=a;                                    % Assign a to the number of moles of Co
nh2=b;                                    % Assign b to the number of moles of H2
nco2=(nc-a);                              % Assign (nc-a)to the number of moles of Co2
nh2o=(nh/2-b);                            % Assign (nh/2-b)to the number of moles of H2o
no2=(2*nro2-nco-2*nco2-nh2o)/2;           % Compute the number of moles of O2 in the product
nn2=nro2*79/21;                           % Compute the number of moles of N2 in the product
n=(nco+nco2+nh2o+nh2+nn2+no2);            % Compute the total number of moles of all the species
in the product
pco=(nco/n)*p;                            % Compute the partial pressure of CO in the product
pco2=(nco2/n)*p;                          % Compute the partial pressure of CO2 in the product
po2=(no2/n)*p;                            % Compute the partial pressure of O2 in the product

%k=pco2/(pco*po2^0.5);                    % k is equal to the ratio of pco2/ pco &po2 as shown

logk=dissk_co2(t);                        % Call the function dissk_co2 to compute the log of
dissociation constant k
k=10^logk;                                % Compute the dissociation constant from its log


ph2=(nh2/n)*p;                            % Compute the partial pressure of H2 in the product
ph2o=(nh2o/n)*p;                          % Compute the partial pressure of H2O in the product

%k1=ph2o/(ph2*po2^0.5);                   % k is equal to the ratio of pH2O/pH2 &pO2 as shown

logk1=dissk_h2o(t);                       % Call the function dissk_h2o to compute the log of
dissociation constant k
k1=10^logk1;                              % Compute the dissociation constant from its log

% solve for the variables a and b and return only the real values
[sa,sb]=solve(ph2o/(ph2*po2^0.5)==k1,pco2/(pco*po2^0.5)==k,'real',true);

sa=double(sa);                           % return the solution to a in decimal form
sb=double(sb);                           % return the solution to b in decimal form
```

`

```
nco=sa;                                   % compute the number of moles of CO in the product
nh2=sb;                                   % compute the number of moles of H2 in the product
nco2=(nc-sa);                             % compute the number of moles of CO2 in the product
nh2o=(nh/2-sb);                           % compute the number of moles of H2o in the product
no2=(2*nro2-sa-2*(nc-sa)-(nh/2-sb))/2;    % compute the number of moles of O2 in the product
nn2=nro2*79/21;                           % compute the number of moles of N2 in the product
```

Published with MATLAB® R2015a

`

Appendix VIII Internal energy interpolation function

```
function e=internal_energyoh(x)
% This function calculates the internal energy of OH when given the
% temperature x in kelvin
% THE SYNTAX FOR THE FUNCTION IS;
% U=internal_energyoh(x);
% where U is the internal energy
% The unit of the internal energy is in KJ/KMOL.
% the data set used for this computation are those given in THERMODYNAMICS
% AND TRANSPORT PROPERTIES OF FLUID SI UNITS COMPILED BY G.F.C. ROGERS AND
% Y.R.MAYHEW
```

DATA SET

```
t=[0;100;200;298.150000000000;300;400;600;800;1000;1200;1400;1600;1800;2000;2200;2400;2600;2800;3
000;3200;3400;3600;3800;4000];
u=[-9171;-6969;-4638;-2479;-2440;-
292;3955;8227;12618;17181;21928;26847;31924;37131;42460;47885;53397;58985;64640;70354;76118;81927
;87783;93680];
```

INTERPOLATION CODE

```
a=[t,u];
[r ,c]=size(a);
for i=1:r;
    for j=1:c;
    if a(i,1)==x;
        k=i;
        e=a(k,2);
    else
        if a(i,1)<x;
        k=i;
        lower_x=a(k,1);
        upper_x=a(k+1,1);
        lower_e=a(k,2);
        upper_e=a(k+1,2);
        e=((x-lower_x)/(upper_x-lower_x))*(upper_e-lower_e)+lower_e;
        end

    end
    end
end
```

Published with MATLAB® R2015a

`

`

```
function e=internal_energyo2(x)
% This function calculates the internal energy of O2 when given the
% temperature x in kelvin
% THE SYNTAX FOR THE FUNCTION IS;
% U=internal_energyo2(x);
% where U is the internal energy
% The unit of the internal energy is in KJ/KMOL.
% the data set used for this computation are those given in THERMODYNAMICS
% AND TRANSPORT PROPERTIES OF FLUID SI UNITS COMPILED BY G.F.C. ROGERS AND
% Y.R.MAYHEW
t=[0;100;200;298.150000000000;300;400;600;800;1000;1200;1400;1600;1800;2000;2200;2400;2600;2800;3
000;3200;3400;3600;3800;4000];
u=[-8682;-6610;-4529;-2479;-2440;-
297;4258;9189;14392;19788;25325;30976;36723;42571;48510;54537;60657;66864;73155;79521;85963;92467
;99034;105660];

a=[t,u];
[r ,c]=size(a);
for i=1:r;
    for j=1:c;
    if a(i,1)==x;
        k=i;
        e=a(k,2);
    else
        if a(i,1)<x;
        k=i;
        lower_x=a(k,1);
        upper_x=a(k+1,1);
        lower_e=a(k,2);
        upper_e=a(k+1,2);
        e=((x-lower_x)/(upper_x-lower_x))*(upper_e-lower_e)+lower_e;
        end

    end
    end
end
```

Published with MATLAB® R2015a

`

```
function e=internal_energyn2(x)
% This function calculates the internal energy of N2 when given the
% temperature x in kelvin
% THE SYNTAX FOR THE FUNCTION IS;
% U=internal_energyn2(x);
% where U is the internal energy
% The unit of the internal energy is in KJ/KMOL.
% the data set used for this computation are those given in THERMODYNAMICS
% AND TRANSPORT PROPERTIES OF FLUID SI UNITS COMPILED BY G.F.C. ROGERS AND
% Y.R.MAYHEW
t=[0;100;200;298.150000000000;300;400;600;800;1000;1200;1400;1600;1800;2000;2200;2400;2600;2800;3
000;3200;3400;3600;3800;4000];
u=[-8669;-6601;-4521;-2479;-2440;-
355;3902;8394;13145;18131;23296;28600;34016;39512;45079;50696;56364;62065;67795;73555;79339;85149
;90976;96819];

a=[t,u];
[r ,c]=size(a);
for i=1:r;
    for j=1:c;
    if a(i,1)==x;
        k=i;
        e=a(k,2);
    else
        if a(i,1)<x;
        k=i;
        lower_x=a(k,1);
        upper_x=a(k+1,1);
        lower_e=a(k,2);
        upper_e=a(k+1,2);
        e=((x-lower_x)/(upper_x-lower_x))*(upper_e-lower_e)+lower_e;
        end

    end
    end
end
```

Published with MATLAB® R2015a

`

```
function e=internal_energyh2o(x)
% This function calculates the internal energy of H2O when given the
% temperature x in kelvin
% THE SYNTAX FOR THE FUNCTION IS;
% U=internal_energyh2o(x);
% where U is the internal energy
% The unit of the internal energy is in KJ/KMOL.
% the data set used for this computation are those given in THERMODYNAMICS
% AND TRANSPORT PROPERTIES OF FLUID SI UNITS COMPILED BY G.F.C. ROGERS AND
% Y.R.MAYHEW
t=[0;100;200;298.150000000000;300;400;600;800;1000;1200;1400;1600;1800;2000;2200;2400;2600;2800;3
000;3200;3400;3600;3800;4000];
u=[-9904;-7446;-4943;-2479;-
2432;126;5509;11340;17664;24499;31806;39541;47643;56060;64744;73650;82752;92014;101420;110950;120
590;130320;140130;150020];
a=[t,u];
[r ,c]=size(a);
for i=1:r;
    for j=1:c;
    if a(i,1)==x;
        k=i;
        e=a(k,2);
    else
        if a(i,1)<x;
        k=i;
        lower_x=a(k,1);
        upper_x=a(k+1,1);
        lower_e=a(k,2);
        upper_e=a(k+1,2);
        e=((x-lower_x)/(upper_x-lower_x))*(upper_e-lower_e)+lower_e;
        end

    end
    end
end
```

Published with MATLAB® R2015a

`

```
function e=internal_energyh2(x)
% This function calculates the internal energy of H2 when given the
% temperature x in kelvin
% THE SYNTAX FOR THE FUNCTION IS;
% U=internal_energyh2(x);
% where U is the internal energy
% The unit of the internal energy is in KJ/KMOL.
% the data set used for this computation are those given in THERMODYNAMICS
% AND TRANSPORT PROPERTIES OF FLUID SI UNITS COMPILED BY G.F.C. ROGERS AND
% Y.R.MAYHEW
t=[0;100;200;298.150000000000;300;400;600;800;1000;1200;1400;1600;1800;2000;2200;2400;2600;2800;3
000;3200;3400;3600;3800;4000];
u=[-8468;-6124;-4433;-2479;-2440;-
368;3823;8051;12371;16817;21422;26219;31184;36303;41569;46960;52473;58090;63799;69592;75469;81430
;87469;93589];

a=[t,u];
[r ,c]=size(a);
for i=1:r;
    for j=1:c;
    if a(i,1)==x;
        k=i;
        e=a(k,2);
    else
        if a(i,1)<x;
        k=i;
        lower_x=a(k,1);
        upper_x=a(k+1,1);
        lower_e=a(k,2);
        upper_e=a(k+1,2);
        e=((x-lower_x)/(upper_x-lower_x))*(upper_e-lower_e)+lower_e;
        end

    end
    end
end
```

Published with MATLAB® R2015a

```
function e=internal_energyco2(x)
% This function calculates the internal energy of CO2 when given the
% temperature x
% THE SYNTAX FOR THE FUNCTION IS;
% U=internal_energyco2(x);
% where U is the internal energy
% The unit of the temperature is in kelvin while the internal energy is in
% KJ/KMOL.
% the data set used for this computation are those given in THERMODYNAMICS
% AND TRANSPORT PROPERTIES OF FLUID SI UNITS COMPILED BY G.F.C. ROGERS AND
% Y.R.MAYHEW
load('enthalpy_of_gases_file.mat')
t=[0;100;200;298.150000000000;300;400;600;800;1000;1200;1400;1600;1800;2000;2200;2400;2600;2800;3
000;3200;3400;3600;3800;4000];
u=[-9364;-7287;-5077;-2479;-
2427;683;7927;16164;25091;34507;44266;54277;64476;74821;85283;95833;106470;117160;127920;138720;1
49580;160470;171400;182370];
a=[t,u];
[r ,c]=size(a);
for i=1:r;
    for j=1:c;
    if a(i,1)==x;
        k=i;
        e=a(k,2);
    else
        if a(i,1)<x;
        k=i;
        lower_x=a(k,1);
        upper_x=a(k+1,1);
        lower_e=a(k,2);
        upper_e=a(k+1,2);
        e=((x-lower_x)/(upper_x-lower_x))*(upper_e-lower_e)+lower_e;
        end

    end
    end
end
```

Published with MATLAB® R2015a

`

Appendix IX Thermal Conductivity k Interpolation Function

```
function kk=thermalK_propane(x)
%This function calculates the THERMAL CONDUCTIVITY OF PROPANE IN W/m*K
%when the temperature x in kelvin is known
% THE SYNTAX FOR THE FUNCTION IS;
% k=thermalK_propane(x);
% where K is the THERMAL CONDUCTIVITY OF BUTANE at 1 bar and x temperature
% the data set used for this computation are from https://www.engineeringtoolbox.com


T=[231,248,263,268,273,278,298,303,323,348,373,398,423,448,473,523,573,623,673,773];
K=[0.0116,0.0132,0.0146,0.0151,0.0156,0.0162,0.0183,0.0189,0.0211,0.0242,0.0274,0.0307,0.0343,0.0
38,0.042,0.0503,0.0594,0.0693,0.0798,0.103];
a=[T;K];
a=a';
[r ,c]=size(a);
for i=1:r;
    for j=1:c;
    if a(i,1)==x;
        k=i;
        kk=a(k,2);
    else
        if a(i,1)<x;
        k=i;
        lower_x=a(k,1);
        upper_x=a(k+1,1);
        lower_e=a(k,2);
        upper_e=a(k+1,2);
        kk=((x-lower_x)/(upper_x-lower_x))*(upper_e-lower_e)+lower_e;
        end

    end
    end
end
```

Published with MATLAB® R2015a

`

```
function kk=thermalK_methane(x)
%This function calculates the THERMAL CONDUCTIVITY OF METHANE W/m*K
%when the temperature x in kelvin is given
% THE SYNTAX FOR THE FUNCTION IS;
% k=thermalK_methane(x);
% where K is the THERMAL CONDUCTIVITY of methane at 1 bar and x temperature
% the data set used for this computation are from https://www.engineeringtoolbox.com


T=[283,293,303,323,348,373,398,423,448,473,523,573,623,673,773];
K=[0.032,0.0333,0.0347,0.0376,0.0413,0.0453,0.0494,0.0537,0.0582,0.0629,0.0727,0.083,0.0937,0.1046,0.1267];
a=[T;K];
a=a';
[r ,c]=size(a);
for i=1:r;
    for j=1:c;
    if a(i,1)==x;
        k=i;
        kk=a(k,2);
    else
        if a(i,1)<x;
        k=i;
        lower_x=a(k,1);
        upper_x=a(k+1,1);
        lower_e=a(k,2);
        upper_e=a(k+1,2);
        kk=((x-lower_x)/(upper_x-lower_x))*(upper_e-lower_e)+lower_e;
        end

    end
    end
end
```

Published with MATLAB® R2015a

`

```
function kk=thermalK_butane(x)
%This function calculates the THERMAL CONDUCTIVITY OF BUTANE W/m*K
%when the temperature x in kelvin is known
% THE SYNTAX FOR THE FUNCTION IS;
% k=thermalK_butane(x);
% where K is the THERMAL CONDUCTIVITY of butane at 1 bar and x temperature
% the data set used for this computation are from https://www.engineeringtoolbox.com


T=[283,293,303,323,348,373,398,423,448,473,523,573,623,673,773];
K=[0.01512,0.01607,0.01706,0.01913,0.0219,0.02487,0.02803,0.0314,0.03496,0.03872,0.04684,0.05576,
0.0654,0.076,0.09942];
a=[T;K];
a=a';
[r ,c]=size(a);
for i=1:r;
    for j=1:c;
    if a(i,1)==x;
        k=i;
        kk=a(k,2);
    else
        if a(i,1)<x;
        k=i;
        lower_x=a(k,1);
        upper_x=a(k+1,1);
        lower_e=a(k,2);
        upper_e=a(k+1,2);
        kk=((x-lower_x)/(upper_x-lower_x))*(upper_e-lower_e)+lower_e;
        end

    end
    end
end
```

Published with MATLAB® R2015a

`

Appendix X Specific heat capacity interpolation function

```
function kk=cp_propane(x)
```

BACKGROUND INFORMATION

```
%This function calculates the isobaric specific heat capacity of Propane in
%KJ/KMOL*K
%when the temperature x in kelvin is known
% THE SYNTAX FOR THE FUNCTION IS;
% K=cp_propane(x);
% where K is the isobaric specific heat capacity of cp of propane
% the data set used for this computation are from https://www.engineeringtoolbox.com
```

DATA SET

```
T=[0,293,313,333,353,373,393,413,433,453,473,493,513,533];
cp=[0.07,0.0734,0.0771,0.0809,0.0847,0.0886,0.0925,0.0963,0.1002,0.1039,0.1076,0.1112,0.1146,0.11
8];
```

INTERPOLATION CODE

```
a=[T;cp];
a=a';
[r ,c]=size(a);
for i=1:r;
    for j=1:c;
    if a(i,1)==x;
        k=i;
        kk=a(k,2);
    else
        if a(i,1)<x;
        k=i;
        lower_x=a(k,1);
        upper_x=a(k+1,1);
        lower_e=a(k,2);
        upper_e=a(k+1,2);
        kk=((x-lower_x)/(upper_x-lower_x))*(upper_e-lower_e)+lower_e;
        end

    end
    end
end
```

Published with MATLAB® R2015a

`

`

```
function kk=cp_methane(x)
```

BACKGROUND INFORMATION

```
%This function calculates the isobaric specific heat capacity of METHANE in
%KJ/KMOL*K
%when the temperature x in kelvin is known
% THE SYNTAX FOR THE FUNCTION IS;
% K=cp_methane(x);
% where K is the isobaric specific heat capacity of cp of butane
% the data set used for this computation are from https://www.engineeringtoolbox.com
```

DATA SET

```
T=[200,225,250,275,300,325,350,375,400,450,500,550,600,700,800];
cp=[0.033,0.034,0.034,0.035,0.036,0.037,0.038,0.039,0.040,0.043,0.046,0.049,0.052,0.058,0.063];
```

INTERPOLATION CODE

```
a=[T;cp];
a=a';
[r ,c]=size(a);
for i=1:r;
    for j=1:c;
    if a(i,1)==x;
        k=i;
        kk=a(k,2);
    else
        if a(i,1)<x;
        k=i;
        lower_x=a(k,1);
        upper_x=a(k+1,1);
        lower_e=a(k,2);
        upper_e=a(k+1,2);
        kk=((x-lower_x)/(upper_x-lower_x))*(upper_e-lower_e)+lower_e;
        end

    end
    end
end
```

Published with MATLAB® R2015a

`

```
function kk=cp_butane(x)
```

BACKGROUND INFORMATION

```
%This function calculates the isobaric specific heat capacity of butane in
%KJ/KMOL*K
%when the temperature x in kelvin is known
% THE SYNTAX FOR THE FUNCTION IS;
% K=cp_butane(x);
% where K is the isobaric specific heat capacity of cp of butane
% the data set used for this computation are from
% https://www.engineeringtoolbox.com
```

DATA SET

```
T=[0,283,293,303,313,323,333,343,353,363,373,383,393,413,433,453,473,493,513,533];
cp=[0.0954,0.0974,0.0995,0.1017,0.104,0.1064,0.1088,0.1113,0.1138,0.1163,0.1188,0.1213,0.1238,0.1
287,0.1335,0.1383,0.1429,0.1475,0.1518,0.1561];

%INTERPOLATION CODE

a=[T;cp];
a=a';
[r ,c]=size(a);
for i=1:r;
    for j=1:c;
    if a(i,1)==x;
        k=i;
        kk=a(k,2);
    else
        if a(i,1)<x;
        k=i;
        lower_x=a(k,1);
        upper_x=a(k+1,1);
        lower_e=a(k,2);
        upper_e=a(k+1,2);
        kk=((x-lower_x)/(upper_x-lower_x))*(upper_e-lower_e)+lower_e;
        end

    end
    end
end
```

Published with MATLAB® R2015a

`

Appendix XI Kinematic Viscosity Interpolation Function

```
function kk=Kviscosity_propane(x)
%This function calculates the kinematic viscosity of of propane in m2/s
%when the temperature x in kelvin is given
% THE SYNTAX FOR THE FUNCTION IS;
%k=Kviscosity_propane(x)
% where K is the kinematic viscosity of of propane
% the data set used for this computation are from
% https://www.engineeringtoolbox.com


T=[100,150,200,250,300,350,400,450,500,550,600,650,700,750,800,850,900,950,1000];
kviscosity=[5.26e-06,9.87e-07,4.730e-07,3.130e-06,4.56e-06,6.23e-06,8.11e-06,1.021e-05,1.25e-
05,1.497e-05,1.761e-05,2.04e-05,2.334e-05,2.641e-05,2.959e-05,3.288e-05,3.626e-05,3.972e-
05,4.324e-05];

a=[T;kviscosity];
a=a';
[r ,c]=size(a);
for i=1:r;
    for j=1:c;
    if a(i,1)==x;
        k=i;
        kk=a(k,2);
    else
        if a(i,1)<x;
        k=i;
        lower_x=a(k,1);
        upper_x=a(k+1,1);
        lower_e=a(k,2);
        upper_e=a(k+1,2);
        kk=((x-lower_x)/(upper_x-lower_x))*(upper_e-lower_e)+lower_e;
        end

    end
    end
end
```

Published with MATLAB® R2015a

`

```
function kk=Kviscosity_methane(x)
%This function calculates the kinematic viscosity of of methane in m2/s
%when the temperature x in kelvin is given
% THE SYNTAX FOR THE FUNCTION IS;
%k=Kviscosity_methane(x)
% where K is the kinematic viscosity of of methane
% the data set used for this computation are from
% https://www.engineeringtoolbox.com


T=[100,150,200,250,300,350,400,450,500,550,600,650,700,750,800,850,900,950,1000];
kviscosity=[1.91e-06,4.46e-06,7.93e-06,1.222e-05,1.727e-05,2.301e-05,2.939e-05,3.635e-05,4.385e-
05,5.187e-05,6.036e-05,6.93e-05,7.866e-05,8.842e-05,8.857e-
05,0.00010907,0.00011991,0.00013107,0.00014251];
a=[T;kviscosity];
a=a';
[r ,c]=size(a);
for i=1:r;
    for j=1:c;
    if a(i,1)==x;
        k=i;
        kk=a(k,2);
    else
        if a(i,1)<x;
        k=i;
        lower_x=a(k,1);
        upper_x=a(k+1,1);
        lower_e=a(k,2);
        upper_e=a(k+1,2);
        kk=((x-lower_x)/(upper_x-lower_x))*(upper_e-lower_e)+lower_e;
        end

    end
    end
end
```

Published with MATLAB® R2015a

`

```
function kk=Kviscosity_butane(x)
%This function calculates the kinematic viscosity of of propane in m2/s
%when the temperature x in kelvin is given
% THE SYNTAX FOR THE FUNCTION IS;
%k=Kviscosity_butane(x)
% where K is the kinematic viscosity of of
% the data set used for this computation are from
% https://www.engineeringtoolbox.com


T=[150,200,250,300,350,400,450,500,550];
kviscosity=[1.902e-06,7.37e-07,4.15e-07,3.11e-06,4.28e-06,5.6e-06,7.08e-06,8.72e-06,1.05e-05];
a=[T;kviscosity];
a=a';
[r ,c]=size(a);
for i=1:r;
    for j=1:c;
    if a(i,1)==x;
        k=i;
        kk=a(k,2);
    else
        if a(i,1)<x;
        k=i;
        lower_x=a(k,1);
        upper_x=a(k+1,1);
        lower_e=a(k,2);
        upper_e=a(k+1,2);
        kk=((x-lower_x)/(upper_x-lower_x))*(upper_e-lower_e)+lower_e;
        end

    end
    end
end
```

Published with MATLAB® R2015a